UPPSALA
UNIVERSITET

Digital Comprehensive Summaries of Uppsala Dissertations from the Faculty of Science and Technology 1307

Photocatalytic TiO_2 thin films for air cleaning

Effect of facet orientation, chemical functionalization, and reaction conditions

BOZHIDAR STEFANOV

ACTA
UNIVERSITATIS
UPSALIENSIS
UPPSALA
2015

ISSN 1651-6214
ISBN 978-91-554-9387-5
urn:nbn:se:uu:diva-265056

Dissertation presented at Uppsala University to be publicly examined in Polhemssalen, Lägerhyddsv. 1, Uppsala, Friday, 11 December 2015 at 09:15 for the degree of Doctor of Philosophy. The examination will be conducted in English. Faculty examiner: Prof Peter Christian Kjærgaard Vesborg.

Abstract

Stefanov, B. 2015. Photocatalytic TiO_2 thin films for air cleaning. Effect of facet orientation, chemical functionalization, and reaction conditions. *Digital Comprehensive Summaries of Uppsala Dissertations from the Faculty of Science and Technology* 1307. 148 pp. Uppsala: Acta Universitatis Upsaliensis. ISBN 978-91-554-9387-5.

Poor indoor air quality is a source of adverse health effects. TiO_2 coatings deposited on well-illuminated surfaces, such as window panes, can be used to fully mineralize indoor air pollutants by photocatalysis. In such applications it is important to ensure stable photocatalytic activity for a wide range of operating conditions, such as relative humidity and temperature, and to avoid deactivation of the catalyst.

In this thesis photocatalytic removal of the indoor-pollutant acetaldehyde (CH_3CHO) on nanostructured TiO_2 films is investigated, and in particular it is proposed how such films can be modified and operated for maximum performance. Catalyst deactivation can be reduced by purposefully changing the surface acidity of TiO_2 by covalently attaching SO_4 to the surface. Moreover, the overall photocatalytic activity on anatase TiO_2 films can be improved by increasing the fraction of exposed reactive {001} surfaces, which otherwise are dominated by {101} surfaces.

In the first part of the thesis mode-resolved in-situ FTIR is used to elucidate the reaction kinetics of CH_3CHO adsorption and photo-oxidation on the TiO_2 and SO_4 – modified TiO_2 surfaces. Surface concentrations of main products and corresponding reaction rates were determined. Formate is the major reaction product, whose further oxidation limits the complete oxidation to gaseous species, and is responsible for photocatalyst deactivation by site inhibition. The oxidation reaction is characterized by two reaction pathways, which are associated with two types of surface reaction sites. On the sulfate modified TiO_2 catalyst fewer intermediates are accumulated, and this catalyst resists deactivation much better than pure TiO_2. A hitherto unknown intermediate – surface-bound acetaldehyde dimer with an adsorption band at 1643 cm^{-1} was discovered, using interplay between FTIR spectroscopy and DFT calculations.

The second part of the thesis treats the effect of increasing the relative abundance of exposed {001} facets on the photocatalytic activity of anatase TiO_2 films prepared by DC magnetron sputtering. A positive effect was observed both for liquid-phase photo-oxidation of methylene blue, and for gas-phase photocatalytic removal of CH_3CHO. In both cases it was found that the exposed {001} surfaces were an order of magnitude more reactive, compared to the {101} ones. Furthermore, it was found that the reactive films were more resilient towards deactivation, and exhibited almost unchanged activity under varying reaction conditions. Finally, a synergetic effect of SO_4 – modification and high fraction of exposed {001} surfaces was found, yielding photocatalysts with sustained high activity.

The results presented here for facet controlled and chemically modified TiO_2 films are of interest for applications in the built environment for indoor air purification and as self-cleaning surfaces.

Keywords: titanium dioxide, photocatalysis, thin films, surface functionallization, acetaldehyde, indoor air cleaning, sputter deposition, crystallographic modifications, preferential orientation, self-cleaning surfaces

Bozhidar Stefanov, Department of Engineering Sciences, Solid State Physics, Box 534, Uppsala University, SE-751 21 Uppsala, Sweden.

ISSN 1651-6214
ISBN 978-91-554-9387-5
urn:nbn:se:uu:diva-265056 (http://urn.kb.se/resolve?urn=urn:nbn:se:uu:diva-265056)

“An original idea? That can't be too hard. The library must be full of them ...”

Stephen Fry

List of Papers

This thesis is based on the following papers, which are referred to in the text by their Roman numerals.

I	Stefanov, B.I., Topalian, Z., Granqvist, C.G., Österlund, L. (2013) Acetaldehyde adsorption and condensation on anatase TiO_2: Influence of acetaldehyde dimerization. *Journal of Molecular Catalysis A*, 381:77-88.

II	Topalian, Z., Stefanov, B.I., Granqvist, C.G., Österlund, L. (2013) Adsorption and photo-oxidation of acetaldehyde on TiO_2 and sulfate-modified TiO_2: Studies by in situ FTIR spectroscopy and micro-kinetic modeling. *Journal of Catalysis*, 307:265-274.

III	Stefanov, B.I., Granqvist, C.G., Österlund, L. (2014) Fine control of the amount of preferential <001> orientation in DC magnetron sputtered nanocrystalline TiO_2 films. *Journal of Physics: Conference Series*, 559:012011.

IV	Stefanov, B.I., Österlund, L. (2014) Tuning the Photocatalytic Activity of Anatase TiO_2 Thin Films by Modifying the Preferred <001> Grain Orientation with Reactive DC Magnetron Sputtering. *Coatings,* 4:587-601.

V	Stefanov, B.I., Niklasson G.A., Granqvist, C.G., Österlund, L. (2015) Quantitative relation between photocatalytic activity and degree of <001> orientation for anatase TiO_2 thin films. *Journal of Materials Chemistry A*, 3:17369-17375.

VI	Stefanov, B.I., Niklasson, G.A., Granqvist, C.G., Österlund, L., Gas-phase photocatalytic activity of sputter-deposited anatase TiO_2 films: Effect of <001> preferential orientation, surface temperature and humidity. *in manuscript*.

VII	Stefanov, B.I., Lebrun, D., Mattsson, A., Granqvist, C.G., Österlund, L. (2015) Demonstrating Online Monitoring of Air Pollutant Photodegradation in a 3D Printed Gas-Phase Photocatalysis Reactor. *Journal of Chemical Education*, 92:678-682.

Reprints were made with permission from the respective publishers.

My contributions to the appended papers

I Kinetic modeling, DFT calculations and most of the writing.

II Analysis of the in situ FTIR data, micro-kinetic modeling and fitting, and part of the writing.

III Sample preparation, measurements, data analysis and most of the writing.

IV Construction of the experimental setup, sample preparation, measurements, data analysis and most of the writing.

V Construction of the experimental setup, sample preparation, measurements, data analysis and most of the writing.

VI Construction of the experimental setup, sample preparation, measurements, data analysis and most of the writing.

VII Construction of the experimental setup, and most of the writing.

Contents

1. Introduction

It is estimated that the population of the industrialized world spends more than 90% of their life indoors [1] with approximately 20% of this time spent in the office by working individuals [2]. It was observed that the increased time spent indoors can lead to negative effects on the health status and similar symptoms occur in people who share the same working or living environment [3].

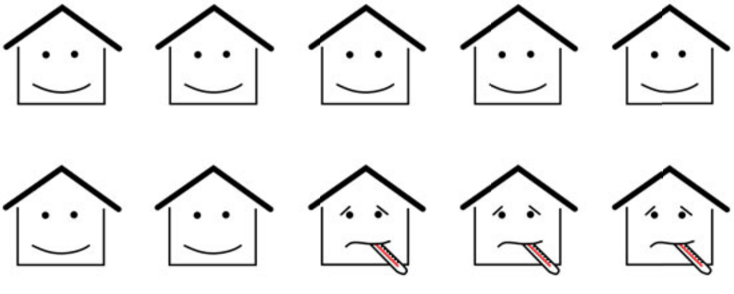

Figure 1.1: According to a report issued by the WHO, SBS was affecting about 10 to 30% of the new or refurbished buildings in 1984. [4]

This has led to the coining of the term Sick Building Syndrome (SBS) by the World Health Organization (WHO) in 1983 [5]. In the 1980s it was estimated that a significant number of newly built or refurbished buildings in the West suffered from poor quality indoor environment and SBS (Figure 1.1). SBS is still a poorly understood multifactorial health condition with a number of non-specific symptoms. These symptoms are often caused by indoor environmental factors such as poor quality of the lighting or the indoor air [6].

Additionally there is an emerging understanding that outdoor emissions contribute to a detrimental indoor air climate. Recently the International Agency for Research on Cancer (IARC) has updated the classification of outdoor air pollution in terms of its carcinogenicity to humans [7]. Previously, IARC has evaluated individual chemicals and specific mixtures that occur in outdoor air pollution, such as diesel engine exhaust, solvents, metals, and dust. They have now broadened their analysis to include outdoor air pollution in general, including particulate matter. In addition to the contribution from outdoor pollution, particulate matter (PM), and microorganisms (and their metabolites), the main group of indoor air pollutants is the volatile organic compounds (VOCs), examples of which are shown in Figure 1.2.

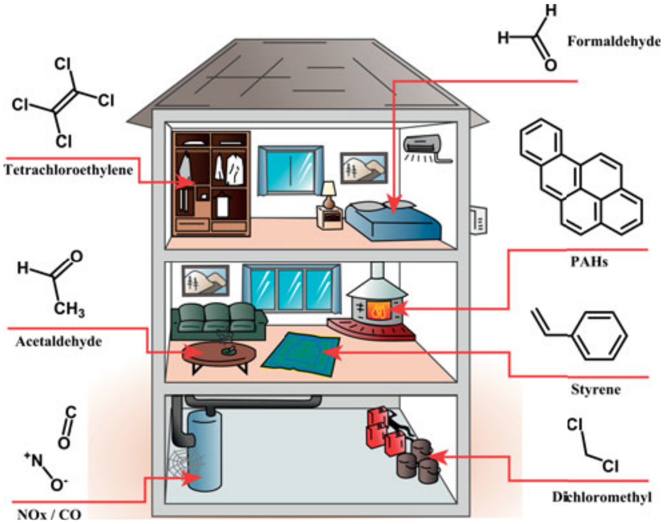

Figure 1.2: Common indoor VOCs and their sources. Tetrachloroethylene (from dry cleaning); acetaldehyde (smoking); NO_x / CO (central heating); dichloromethylene (household chemistry); styrene (synthetic textiles); PAHs (indoor fireplaces); and formaldehyde (furniture).

This group is composed of all organic compounds whose boiling points lie between 50 and 260°C [8]. Among them a significant health risk is posed by aldehydes, such as acetaldehyde and formaldehyde [9]. They are released by many sources, such as synthetic materials (Figures 1.2, 1.3), building insulation, and domestic chemistry [10; 11; 12]. Their accumulation is enhanced through poor ventilation and through the use of air conditioning [13].

Acetaldehyde is a common contributor to air pollution. In the outdoor environment it is released from ethanol-fuelled vehicles [14], while indoors it is associated with the bad indoor air odor [15]. It is also known to be potentially carcinogenic to humans [16], and the maximum occupational exposure limit is 35 ppm (19 mg/m^3; short term exposure limit) in Europe, and 25 ppm (45 mg/m^3; ACGIH ceiling) or 200 ppm (360 mg/m^3, 8 h time weighted OSHA PEL value) in USA [17; 18]. By comparison the odor threshold for acetaldehyde is 50 ppb (0.09 mg/m^3), while the LC_{50} value is approximately 2% (37000 mg/m^3).[1]

---

[1] LC_{50}, or the lethal concentraion$_{50}$, is the calculated concentration of a chemical in air to which exposure for a specific length of time is expected to cause death in 50% of a defined experimental animal population.

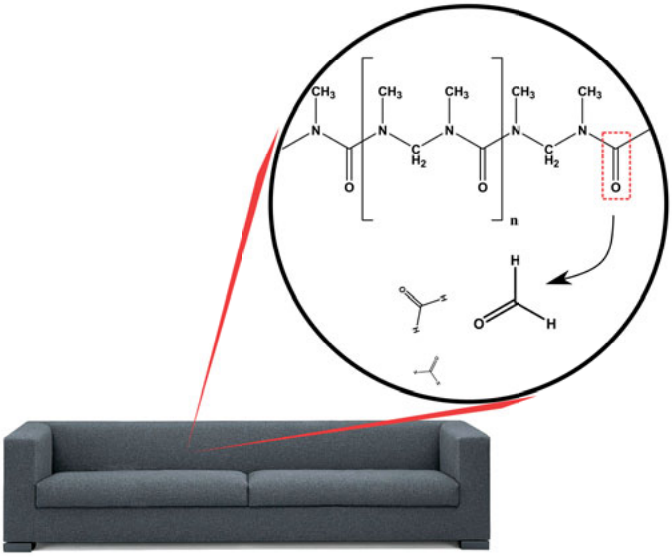

Figure 1.3: The use of synthetic materials, such as the hydrolysis sensitive urea-formaldehyde resins, used to bind MDF panels in furniture can lead to release of aldehydes and other VOCs in the indoor environment [19].

Promising methods to reduce the VOC concentration in the indoor air include advanced oxidation processes (AOPs) and in particular the photocatalytic oxidation of VOCs. Photocatalysts, e.g. TiO_2, can be activated by low-intensity UVA light (λ = 300 – 400 nm), of the order 0.1 – 1 W m^{-2}, and utilized to completely mineralize acetaldehyde, yielding only CO_2 and H_2O [20].

It is possible to integrate photocatalysts into the built environment in the form of coatings. In order to achieve maximum efficiency against indoor pollutants these can be deposited onto building elements with sufficiently large and well–illuminated surface. For example the surface of windowpanes provides a suitable substrate for photocatalysis, as they are in contact with indoor air, offer a large area for adsorption of volatile compounds, and are constantly illuminated by natural solar light. However, the concept of “photocatalytic” windows for indoor air cleaning is yet to be developed, and is explored further in this thesis.

2. Photocatalysis

In general, the definitions employed in thermal heterogeneous catalysis can be carried over to photocatalysis. As shown in Figure 2.1a, the acceleration of the reaction is realized through an intermediate excited state.
According to IUPAC, photocatalysis is the initiation or change in the rate of a chemical reaction, under the action of UV, visible or IR light in the presence of a substance; the photocatalyst [21]. This can have an active or a passive role. In the latter case, the catalyst enhances a photochemical reaction by offering an enhanced surface for improved light absorption and formation of excited states by the reagents (Figure 2.1b). An active photocatalyst, such as TiO_2, generates electron-hole pairs upon illumination. They, in turn, can take part directly in photochemical processes, by an interfacial charge transfer. Alternatively they react with adsorbed water, hydroxyls (electron donors), and oxygen (electron acceptors), which produces reactive radical species (Figure 2.1c).

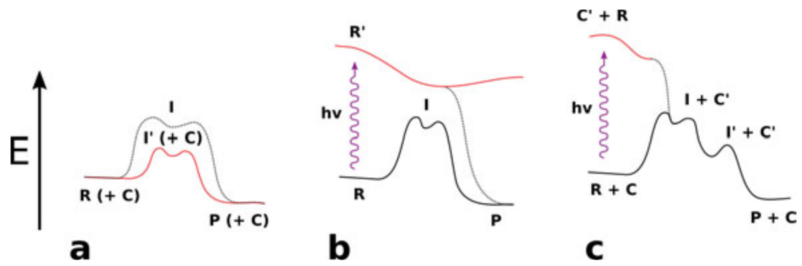

Figure 2.1: Potential energy plots in the case of: (a) thermal reaction, where reagent R is converted into a product P exclusively on the PES surface; (b) a photochemical reaction, where the energy barrier is overcome by a highly-energetic excited state of the reagent R' which is reached through absorption of light energy; and (c) a photocatalytic reaction, where absorption of light leads to an excited state of the catalyst C' in order to overcome the reaction barrier. I and I' indicate intermediate states.

2.1. Basic principles of semiconductor photocatalysis

In heterogeneous photocatalysis, the catalyst can be in the form of nanoparticles (suspended or immobilized), or a polycrystalline thin film deposited on a substrate. The nanostructure is a determining factor for the photocatalytic activity, as it provides the surface area needed for the photogenerated charge pairs to interact with adsorbed reactants.

The photocatalyst is in contact with the liquid or gas-phase reaction environment. When the photocatalyst is illuminated by light of the appropriate wavelength (with energy higher than the band gap energy of the semiconductor photocatalyst, E_g), excited states are formed in the form of photogenerated holes and electrons. These migrate to the phase boundary and initiate the chemical transformations through interfacial charge transfer reactions.

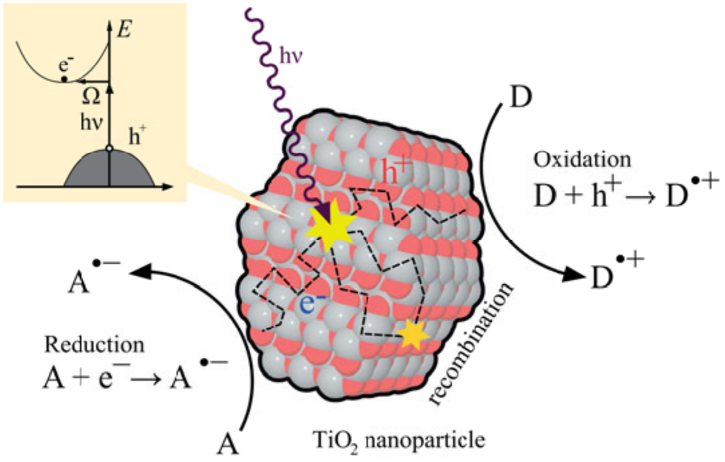

Figure 2.2: Schematic representation of the elementary photo-induced reaction steps, initiated in a semiconductor photocatalyst. The inset depicts the electronic interband transition initiated by absorbed photons, with energies higher than the bandgap energy of the photocatalyst. In TiO_2 the lowest interband transition is an indirect transition with energy of 3.2 eV.

A simplified scheme of the photocatalytic oxidation (PCO) mechanism is presented in Figure 2.2. It schematically represents a semiconductor nanoparticle, whose electronic structure is characterized by a valence band populated with electrons, and the higher energy vacant levels forming the conduction band. They are separated by the bandgap, whose energy is unique for the given semiconductor and determines the energy of the photon required to initiate the photochemical reaction. For bulk TiO_2 $E_g = 3.2\,eV$, which implies that this photocatalyst is activated by UV light ($\lambda \leq 388$ nm). We note that local bandgap and surface states may contribute to the photocatalytic activity, and thus not only the positions of the bulk band edges are important for the efficiency of a photocatalyst [22].

When the photocatalyst absorbs a photon with energy larger than E_g an electron (e^-) is excited from the valence band into the conduction band and an empty state, a.k.a. a hole (h^+), is left into the valence band. The fate of this charge pair (exciton) is determined by the possibility of recombination. This is the process by which the electron returns to its original energy level through a non-radiative transition. In this way the energy of the adsorbed photon is lost in the form of heat. This is the most probable event in a photocatalyst, such as TiO_2, and is responsible for its generally low quantum yield if the order of 1% or lower. In the more favourable scenario, for the purpose of utilizing the excitation energy in chemical reactions, the electron and the hole diffuse through the bulk of the particle and reach the surface, where they may react with adsorbed species through interfacial charge transfer reactions. Those species can play the role of electron donors D) or acceptors (A), depending on whether they react with the electrons or holes. The positively "charged" holes react with electron-donating molecules and oxidize them (eqn. 2.1), while the conduction band electrons take part in reduction reactions with electron-accepting molecules (eqn. 2.2).

$$D + h^+ \rightarrow D^{\bullet +} \qquad (2.1)$$
$$A + e^- \rightarrow A^{\bullet -} \qquad (2.2)$$

Typically the photogenerated holes are of higher importance for photocatalytic activity. They are highly reactive and can take part in the direct oxidation of adsorbed species. In the presence of surface water, or in the case where the photo-oxidation takes place in aqueous solution, they can also react with the water molecules, and highly reactive hydroxyl radicals ($^{\bullet}OH$) are generated (eqn. 2.3).

$$H_2O + h^+ \rightarrow {}^{\bullet}OH + H^+ \qquad (2.3)$$

The oxidation potential for $^{\bullet}OH$ is is 2.8V. This is superseded only by fluorine, and it is a more potent oxidation agent than either H_2O_2 or O_3. This gives it the ability to easily attack adsorbed organic molecules and fully mineralize them to CO_2, H_2O and mineral acids. The only requirement for the generation of hydroxyl radicals is that the process should take place in an environment of sufficient humidity to replenish surface hydroxyls.

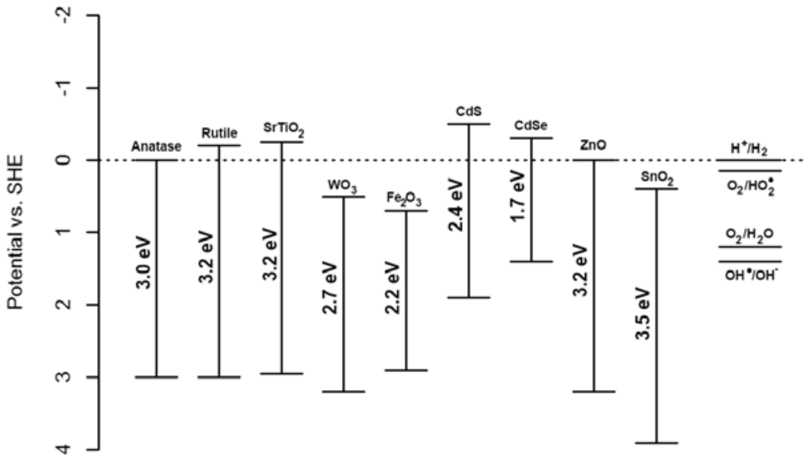

Figure 2.3: HOMO and LUMO levels positions (vs. SHE) for a number of photocatalysts, compared with the redox potential of a couple of important redox couples (at pH = 0) [23].

In order to close the catalytic cycle, the photo – generated electrons must react as well. In the presence of oxygen, another important reactive species is produced on the surface of the photocatalyst –the superoxide ion $O_2{}^{\bullet -}$ (eqn. 2.4). These species can also take part in the PCO, either directly as a reducing agent, or indirectly through the generation of additional hydroxyl radicals (eqns. 2.5 – 2.7).

$$O_2 + e^- \rightarrow O_2{}^{\bullet -} \tag{2.4}$$

$$H^+ + O_2{}^{\bullet -} \rightarrow HO_2{}^{\bullet} \tag{2.5}$$

$$2HO_2{}^{\bullet} \rightarrow H_2O_2 + O_2 \tag{2.6}$$

$$H_2O_2 \rightarrow {}^{\bullet}OH + OH^- \tag{2.7}$$

The ability of a photocatalyst to take part in these reactions is determined by the energies of the HOMO and LUMO levels of the reactant molecules, and their relative positions to the redox potential of the respective reaction (Figure 2.3). The energy of the LUMO level determines the reduction potential of the photogenerated electrons, while the HOMO level determines the oxidizing power of the photogenerated holes.

The ideal photocatalyst for environmental applications should fulfill several conditions. Firstly, it should efficiently utilize a large fraction of the solar radiation spectrum. For indoor applications other sources can be used, such as LEDs, but the quantum efficiency of the catalyst is still crucial. Secondly, it should be photo-chemically stable, and not degrade as a function of usage time. Thirdly, it should be easy to produce and apply, and for air cleaning applications, it should expose a high surface area. Finally, it should be chemically and biologically inert, and safe for the environment, and human health.

2.2. TiO_2 as a photocatalyst

There are a number of semiconductors with photocatalytic properties. These include simple metal oxides with ionic character (e.g. TiO_2, ZnO, WO_3, $SrTiO_3$, SnO_2, Fe_2O_3), and metal sulphides and selenides (e.g. CdS and CdSe). These belong to a class of semiconductors called wide bandgap semiconductors, due to their large bandgaps ($E_g \geq 2\ eV$), which distinguishes them from semiconductors used in electronic applications, which can be activated by thermal excitation. Of these titanium dioxide (TiO_2) stands out as a particularly attractive photocatalyst for several reasons. It has high photocatalytic activity, is an abundant and inexpensive material, is readily prepared as films and particles, and it is non-toxic at most relevant exposure conditions [24].

Photocatalytic TiO_2 has been exploited for practical applications for more than a decade, particularly in Asia [25]. Especially in environmental applications the above beneficial properties of TiO_2 makes it an ideal photocatalyst. Furthermore, TiO_2 has a high chemical and photochemical stability. Its photogenerated holes readily react with H_2O molecules to generate highly energetic hydroxyl radicals, while its photogenerated electrons have sufficient energy to reduce molecular oxygen to superoxide ions (eqns. 2.3 – 2.7) [26].

Commercial TiO_2 is manufactured from three minerals: rutile (93 – 96% TiO_2 content); ilmenite (44 - 70% TiO_2 content); and leucoxene (90% TiO_2 content). There are two extraction methods; the sulfate and the chloride method.

The sulfate method uses ilmenite ($FeTiO_3$) ore; however rutile, which is richer in TiO_2, has been recently also employed. In the sulfate method feedstock is treated with concentrated H_2SO_4 and converted to sulfates. Iron sulfate ($FeSO_4$) is a by-product, which is easily crystallized and extracted. Then the titanyl sulfate ($TiOSO_4$) is separated by evaporation. The last step is the calcination of the $TiOSO_4$ yielding TiO_2.

The chloride method uses only rutile stock and its aim is to refine and purify TiO_2. The first step is high temperature treatment with carbon and chlorine gas. In this way TiO_2 is converted into $TiCl_4$, which is a liquid under normal conditions, and hence can be fractionally distilled. The distilled $TiCl_4$ is then oxidized at temperatures of 1200 – 1700°C by flame pyrolysis, and it is turned almost exclusively into anatase. The chloride method is widely used for preparation of TiO_2 pigment. In 2010 these two methods produced about 1.4 million tons of TiO_2 in the United States alone. The worldwide consumption of TiO_2 equals to about 4 million tons yearly [27].

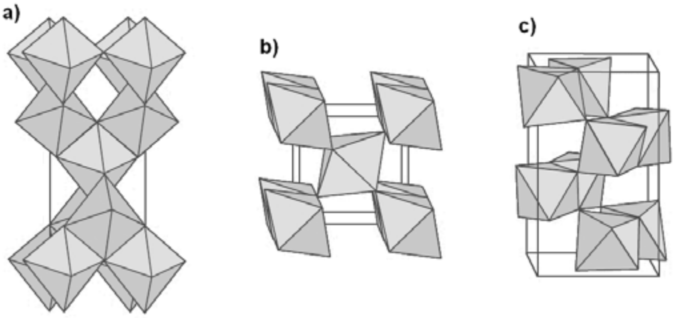

Figure 2.4: Crystal structures of the three naturally occurring TiO_2 modifications: anatase (a), rutile (b), and brookite (c). Every octahedron represents a six-fold oxygen coordinated Ti center. Figure from reference [28].

TiO_2 naturally exists in three crystalline modifications, namely anatase, rutile, and brookite (Figure 2.4). Among them, anatase and rutile are widely used as photocatalysts. The photocatalytic activity of brookite is still relatively unexplored, due to the difficulties in obtaining sufficient quantities of the pure phase. According to some studies it is expected to have high photocatalytic activity [29], which is reasonable considering the structural and electronic similarity to anatase.

Even though rutile has a narrower bandgap than anatase, it is generally considered to exhibit lower photocatalytic activity compared to anatase. In an electrochemical impedance study by Kavan *et al* [30], it was reported that the flatband potential of anatase is approximately 0.2 eV more negative than that of rutile. This implies that the conduction band of anatase lies 0.2 eV above that of rutile, and it has been assumed that the higher photoreactivity of anatase is due to its lower lying Fermi level. This better matches the LUMO level of molecular oxygen. Anatase also has a higher coverage of surface hydroxyl groups [31]. Recently, the data published by Kavan *et al* has been challenged. Scanlon et al. obtained contradictory data showing that the conduction band edge actually lies 0.4 eV lower on anatase, compared to rutile, resulting in a higher work function of the anatase phase [32].

It is also known that mixtures of anatase and rutile express higher activity than either of the two alone. An example of such a mixed catalyst was presented in the study by Kawahara *et al* [33], which demonstrated that a composite of rutile and anatase in a 1:1 ratio showed a threefold increase in activity compared to pure anatase, and a tenfold increase compared to the pure rutile. An explanation of the synergetic properties of the rutile : anatase mixture is provided by the more efficient charge separation when the two phases are in contact with each other. The anatase phase possesses higher electron affinity, thus facilitating e – h pair separation [32].

The synergetic anatase – rutile effect is exploited by one of the most popular commercial photocatalysts in use today, the Degussa P25, a.k.a. Aeroxide TiO_2 P25, after Degussa merged with Evonik. It is inexpensive and has relatively high photoreactivity, which made it the standard for comparison of photocatalytic activity in the literature. It is manufactured through the patented AEROSIL® process, based on the oxidation of $TiCl_4$ in the flame of a H_2/O_2 fueled torch. The resulting TiO_2 has a purity of 99.5%, and a composition varying between 70:30 and 80:20 w/w % (anatase : rutile) [34]. Its crystallites have a cubic to spherical shape, with a mean size of between 21 – 50 nm. The specific surface area of P25 is 50±15 m^2/g. It has been assumed that the high photocatalytic activity of Degussa P25 results from the higher reduction potential of rutile, compared to the anatase [30]. Due to this the photogenerated electrons can migrate between the two phases, leading to better charge separation due to the anatase – rutile junction, and effectively lowering the possibility for recombination of the electron-hole pairs [35].

2.3. Photocatalysis in the indoor environment

Photocatalysis can be used to improve the quality of the indoor environment in a number of ways, e.g. the utilization of photocatalytic materials for indoor air purification and deodoration. As of 2010 there are over 120 patents for indoor air purification devices based on photocatalysis [36].

Photocatalysis on TiO_2 was found to be effective against a number of indoor air pollutants including inorganic gases as NO [37] and CO, VOCs such as benzene, toluene, and xylenes [38], and chlorinated VOCs as tetrachloroethylene (PCE) [39].

It is clear that the only way to use TiO_2 for indoor applications is in the form of an immobilized photocatalyst. For example, it could readily be applied to high-efficiency particulate air (HEPA) filters, which are already used in Heating, Ventilation and Air Conditioning (HVAC) systems. With minimal modifications, such as the provision of UV illumination inside the HVAC system, these modified filters can be used to strip VOCs from the indoor air. TiO_2 impregnated HEPA filters have been already demonstrated to be effective against bioaerosols and bacteria [40] and formaldehyde [41].

There is also a lot of interest in the use of TiO_2 coatings as self-cleaning surfaces. Such surfaces also exhibit antibacterial properties and can effectively attack and kill bacteria at distances up to 50 μm from the surface via free radical generation [42].

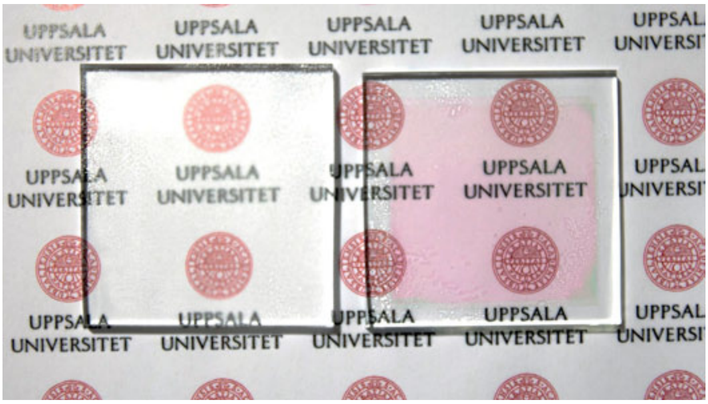

Figure 2.5: Ordinary glass (on the left-hand side) and glass coated with a thin film of TiO_2. After UV illumination and introduction of water vapor the ordinary glass is fogged, while the TiO_2-coated is fully wetted, due to the light-induced superhydrophilic effect, which completely spreads the water on the film, thus avoiding light scattering.

TiO_2 exhibits another property which makes it suitable for indoor applications: light induced superhydrophilicity. This was investigated for the first time in 1995 by researchers of the Japanese company Toto, Inc. They observed that coatings of TiO_2 exhibited an increased hydrophilicity during UV illumination. The contact angle of water on the TiO_2 surface is usually in the order of 30 – 80° (depending on the surface microstructure). After UV illumination it decreases to 0° and the surface is fully wetted (Figure 2.5).

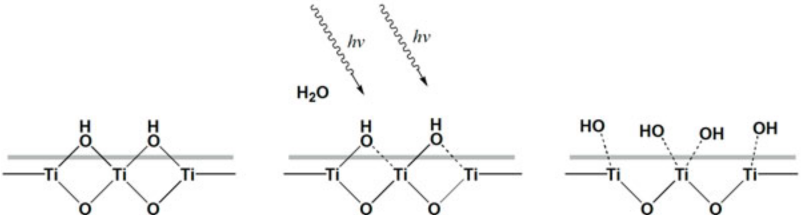

Figure 2.6: Simplified scheme of the hydrophilic – superhydrophilic states transition of the TiO_2 surface

This effect can be reversed, albeit slowly, by storing the TiO_2 coating in darkness for extended periods. However, it was found that through partial modification of the surface with SiO_2 the superhydrophilicity can be preserved even in darkness, for periods of up to several days [43]. The chemical mechanism of the transition from hydrophilicity to superhydrophilicity is described in Figure 2.6. During UV illumination a reaction occurs between surface-bound H_2O molecules and the bridged hydroxyl groups, leading to the creation of more surface hydroxyls, and increased hydrophilicity.

There are already several commercial products based on TiO_2 films, utilizing superhydrophilicity as a method to create self-cleaning glasses for exterior window applications. Examples of such products include Active CLEAR^{TM}, SSG BIOCLEAN^{TM}, and SunClean^{TM} produced by Pilkington Group Ltd, Saint-Gobain Glass UK Ltd, and PPG Residential Glass, respectively [44]. They are manufactured by the deposition of anatase films onto structural glass, through DC-sputtering and Chemical Vapor Deposition (CVD) [45].

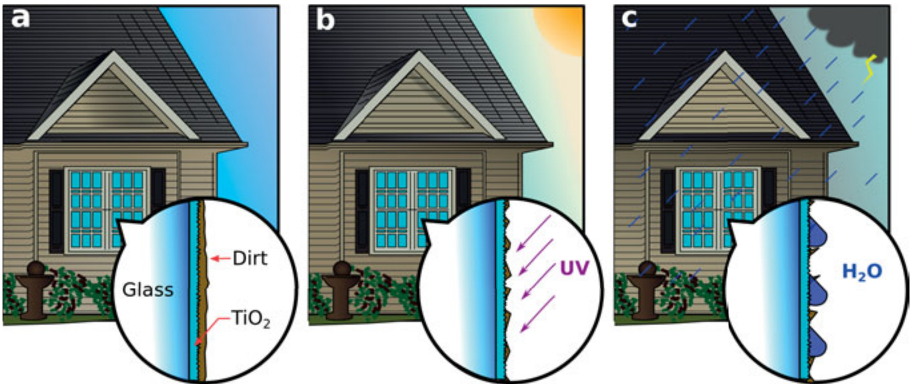

Figure 2.7: Mechanism of action of a self-cleaning window based on TiO_2 coating (a). The combined effects of photocatalysis, initiated by sunlight (b), and light-induced superhydrophilicity (c) help maintain the coated surface clean of contamination.

The combined photocatalytic – superhydrophilic effect, along with its superb optical properties, makes TiO_2 an ideal self-cleaning window coating material (Figure 2.7).

3. Enhancing the activity of TiO_2 for indoor air cleaning

As mentioned in the previous chapter, indoor air quality may benefit substantially from TiO_2 coatings deposited onto large, well – illuminated surfaces, such as windowpanes. A central topic in this thesis is the concept of the "photocatalytic window", a possible construction of which is presented in Figure 3.1.

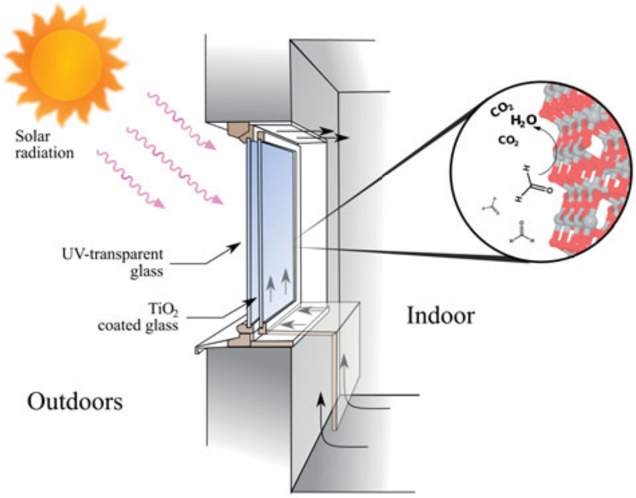

Figure 3.1: Conceptual drawing of the operating principle of a photocatalytic indoor air cleaning window based on a TiO_2 thin film.

These windows can be constructed of a TiO_2 – coated structural glass, facing a sheet of UV – transparent glass (such as the Pilkington OptiWhite^{TM} iron-free glass). The indoor air flows in the gap, between the two sheets, either driven by convection, or a dedicated circulation system. The basic idea behind such setup is simple, but there are two important aspects that have to be considered regarding the TiO_2 photocatalyst used: Its photocatalytic activity has to be high and stable across a wide range of operational conditions related to the dynamics of the indoor environment, such as relative humidity, temperature, etc. It also has to be resistant against long-term deactivation, caused by to the accumulation of reaction intermediates on the catalytic surface.

Being a heterogeneous photocatalyst, TiO_2 reacts with the surrounding media through its surface. Hence, surface modification may be an elegant way to improve some properties of TiO_2. One example is surface roughening through laser ablation, leading to a higher specific surface area [46]. It has also been shown that simple mechanochemical treatment can alter the surface hydrophilicity, and even allow both hydrophobic and hydrophilic areas to co-exist on the same surface [47]. Moreover, since transition metal oxides are in general of hygroscopic nature, the interaction with water vapor is of paramount importance to understanding surface reactions on TiO_2 photocatalysts. We begin this chapter by discussing this latter aspect of TiO_2 heterogeneous photocatalysis.

3.1. Effects of relative humidity on TiO_2 photocatalysis

In laboratory conditions gas-phase photocatalytic activity of TiO_2 is often determined using controlled experiments with “dry” gas mixtures (i.e. dry synthetic air or nitrogen). Studying this simple system allows for easy interpretations of reaction mechanisms and intrinsic activity in order to compare photocatalysts. Unfortunately, it can be difficult to relate results from such “dry” experiments to operando conditions. For example, while most indoor contaminants are in ppb and ppm concentration, even at low relative humidity, the concentration of water is in the order of $10^3 \sim 10^4$ ppm.

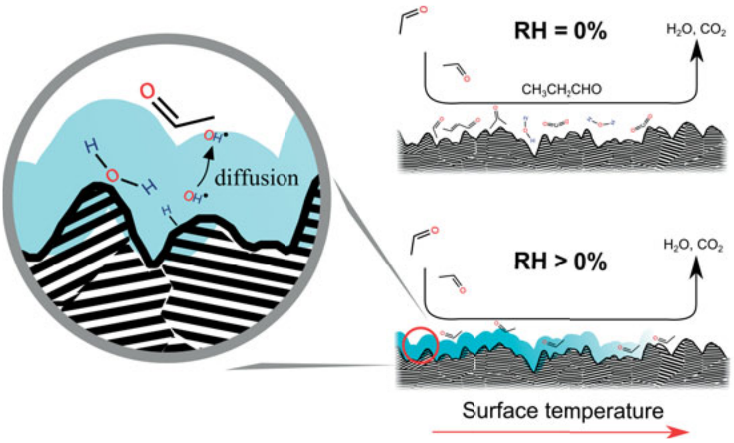

Figure 3.2: Whilst on the dry surface the adsorbed contaminants are directly oxidized by the photogenerated charge pairs, in the presence of water a water layer is formed. It might be beneficial due to the generation of highly-reactive radical species, but it could also mask the intrinsic activity of the catalyst. Heating the surface could be a way to control the effect.

As discussed above TiO_2 has high affinity to water and it is known that under humid conditions water layers form on its surface [48]. They can turn into a major determining factor of the apparent activity in the gas-phase photo-oxidation reactions, as illustrated in Figure 3.2.

In some cases surface water can play an enhancing effect. As described in Section 2.1 photogenerated charge pairs can react with water and oxygen and yield highly reactive radicals, such as $^{\bullet}OH$ and $O_2^{\bullet -}$, which can in turn participate in further oxidation reactions. Thus water acts as a charge scavenger, improving quantum yields. The photogenerated electron-hole pairs can oxidize the adsorbed contaminants directly. However, their lifetime, which is in the order of hundreds of picoseconds [49], poses a narrow window for this to happen. In comparison, $^{\bullet}OH$ and $O_2^{\bullet -}$ both have orders of magnitude longer lifetimes, extending into the nanosecond range [50]. Furthermore, theoretical predictions demonstrate that when the surface of TiO_2 is covered by water, $^{\bullet}OH$ can embed itself in the water layer, diffuse through it, and react with other molecules at some distance from the surface [51; 52]. This is shown in the inset of Figure 3.2.

The diffusion of substrate molecules involved in the photocatalytic reactions will also be a determining factor for photocatalytic activity. Water soluble species, such as acetaldehyde, could also become embedded in the water layer and be oxidized inside it. Non-polar molecules, like the PAHs, will be limited to adsorption on the water layer surface, leading to a suppressing effect. An example of this is the adsorption of acetone and chlorobenzene on TiO_2, where a negligible and suppressing effect was observed in the presence of surface water, respectively [53; 54].

In summary, the effect of RH should be taken into account in gas-phase photocatalytic reactions, as it might alter the apparent activity of the catalyst. This is especially important when photocatalytic coatings are used in the indoor environment, where the relative humidity cannot always be controlled. However, in that case heating the surface might be used in order to mitigate the negative effects of elevated humidity. This could be accomplished actively, by the means of passing an electrical current through a conducting layer behind the TiO_2 coating. Alternatively, passive heating could be achieved by the means of an electro-, photo- or thermochromic coating behind the catalyst. The latter case has advantages, as it brings energy saving benefits, such as controlling IR light transmittance through the window, and further enhances the “smart window” concept.

3.2. Preventing deactivation of TiO_2 through surface functionalization

By using chemical modification techniques much more useful and controllable surface properties are obtainable. For example, the hydrophilicity can be adjusted. We have already mentioned in the previous chapter that SiO_2 modified TiO_2 surfaces can remain superhydrophilic for prolonged periods of time [43]. It has also been demonstrated that TiO_2 nanoparticles can be made hydrophobic through functionalization of the surface with isocyanate groups [55]. These functionalized nanoparticles can be easily dispersed in non-polar solvents and used as building blocks in organic / inorganic composites. Another property that can be adjusted is the surface acidity of TiO_2, achieved by surface functionalization with suitable groups which can participate in proton – transfer reactions.

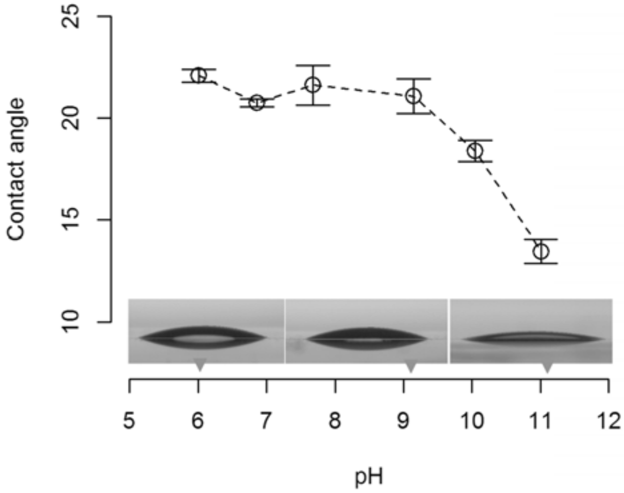

Figure 3.3: SO_4 – modified TiO_2 films, prepared by DC sputtering, express pH – dependent water contact angle, repelling more-strongly water droplets with low pH (unpublished result).

For example surface hydroxyl groups can be replaced with fluorine, through simple ligand exchange with HF acid, leading to the formation of ≡Ti-F centers with enhanced Lewis acidity [56]. In practice, during this fluorine treatment a large fraction of the terminal -OH groups are eliminated. They usually occupy Ti(VI) centers (≡Ti-OH), preventing them to act as adsorption centers or catalytic sites in the surface reactions. It was demonstrated that modified TiO_2 with limited amounts of terminal OH groups, express higher activity against gaseous CH_3CHO than unmodified TiO_2 [57]. Consequently, many surface modification techniques directly target the OH groups. Another example is the H_2O_2 treatment of TiO_2, which replaces part of the OH groups with OOH ones, leading to an extended photocatalytic activity [58].

When enhanced acidic properties of the surface are required, sulfated titania ($SO_4 - TiO_2$) is a good candidate (Figure 3.3). This material is easy to prepare, either through adding a source of sulfate to a TiO_2 sol ($Ti(OH)_4$), followed by calcination [59], or in post-treatment by photofixation of SO_2 on the TiO_2 surface [60]. Sulfated TiO_2 is a very acidic catalyst and is classified as a solid superacid [61]. It expresses high activity even in non-photochemical reactions, such as alkylation in organic synthesis [62].

Enhanced surface acidity may complement the photocatalytic activity. In the PCO of basic species or weaker acids, such as phenol, the elevated surface acidity can enhance adsorption [63]. Enhanced surface acidity can also be used to limit the accumulation of acidic intermediates on the surface. In a recent study of the acetaldehyde photo-oxidation on pristine and sulfated TiO_2 it was found that that the latter surface is deactivated more slowly, due to the weaker bonding of acidic intermediates on the sulfated surface [64].

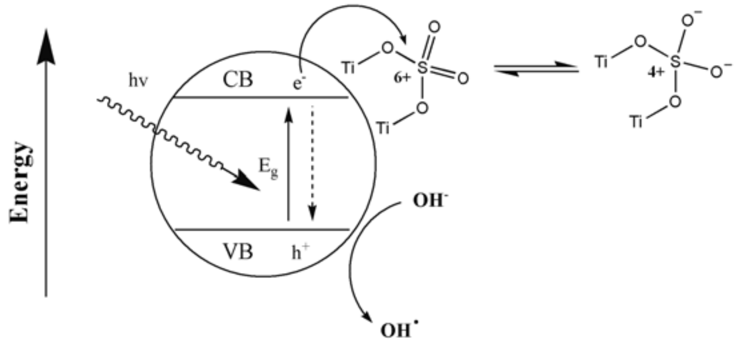

Figure 3.4: The surface SO_4 groups can act as charge separation centers, accepting photogenerated electrons.

The surface SO_4 groups can also improve charge separation, by effectively trapping the photogenerated electrons and preventing recombination (Figure 3.4) [65]. Furthermore, doping bulk TiO_2 with sulfur, can lead to even greater enhancements of the photocatalytic activity. In the crystal lattice, S takes the form of S^{4+} and introduces localized levels in the bandgap of TiO_2. This leads to visible light absorption and photocatalytic activity. Using the synergistic effects of bulk and surface doping highly active catalysts can be developed. These were demonstrated to be highly effective against phenol in liquid-phase [65]. In another study, TiO_2 co-doped with F and S exhibited high activity against NO_2 in gas-phase [66].

3.3. Enhancing the photocatalytic activity of TiO_2 through crystallographic modification

Apart from chemically modifying the surface of anatase TiO_2, or increasing its specific surface area, the modification of its basic crystallographic structure is also a promising and much less investigated method of improving its photocatalytic activity.

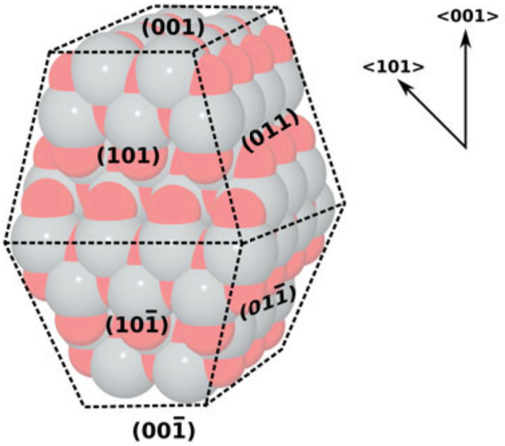

Figure 3.5: Wulff – construction of an anatase TiO_2 nanoparticle with the <101> and <001> crystallographic directions noted on the right side, and the exposed surfaces labeled. Due to symmetry $\big((001),(00\bar{1})\big) \in \{001\}$ and $\big((101),(10\bar{1}),(011),(01\bar{1})\big) \in \{101\}$.

According to the Wulff construction of anatase TiO_2 its nanoparticles are normally dominated by {101} facets, with only a small amount of the highly energetic {001} facets exposed. This leads to the typical truncated bipyramidal shape of the anatase nanocrystals [67; 68], as shown in Figure 3.5. The {001} facets, which typically comprise about 10% of the exposed surface area in anatase [69], are expected to exhibit higher activity in photocatalytic reactions. This is due to their higher surface energy of 0.9 J m^{-2} vs. 0.44 J m^{-2} for {101} [70]. Another hint to the higher activity of {001} is given by the fact that 100% of the Ti atoms on {001} are five-fold coordinated (Ti_{5c}), while this number is only 50% for {101} [71], as shown in Figure 3.6.

A number of theoretical works have revealed that small molecules, such as water, methanol and formic acid decompose on the (001) surface, while molecular adsorption is observed on (101) [72; 73; 74].

Until recently the catalytic properties of the {001} surface have not been investigated, due to the difficulty in obtaining anatase crystals large enough for single-facet mechanistic investigations. This changed with the pioneering work of Yang *et al* [75] who reported a novel method of preparation of TiO_2 particles with controlled facet distribution. It was found that the addition of F^- ions in hydrothermal synthesis lowers the energy of the {001} facets. This allows for crystals with almost 50% exposed active {001} to be prepared. Since this study, the technique was enhanced via the use of other capping agents, which allows for the preparation of TiO_2 with complicated shapes, such as sheets, spheres and belts with up to 100% {001} surface coverage [76; 77; 78; 79].

It has been demonstrated that increasing the surface coverage of {001} in TiO_2 nanoparticles improves their activity in photo-oxidation reactions, such as the removal of MB dye in solution [80]. In other reactions, however, such as H_2 production by water splitting, the activity of {101} was found to be higher [81]. The reason for this discrepancy is related to the selective reactivity that {001} and {101} exhibit towards oxidation and reduction reactions, respectively.

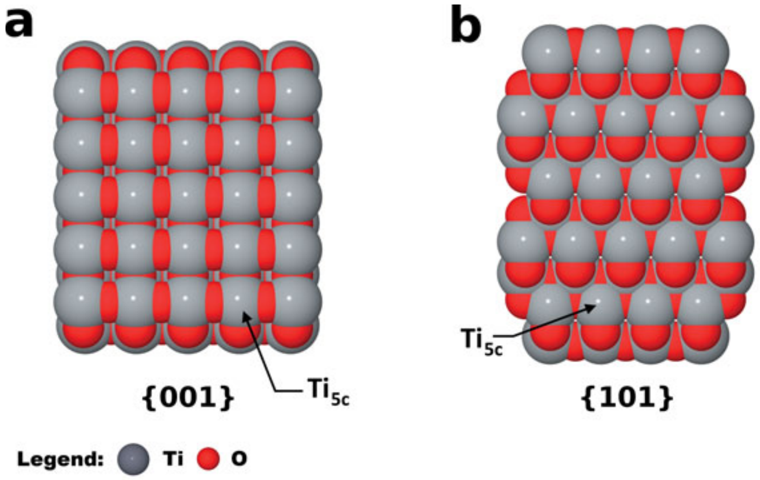

Figure 3.6: One of the reasons for the higher reactivity of {001} surfaces (a) in anatase TiO_2 is the higher density of five-fold coordinated Ti – atoms (Ti_{5c}) on them, compared to {101} surfaces (b).

The first report of this selective reactivity was observed in surface photo-fixation of metal ions. Experimental results show that noble metals (e.g. Au, Ag and Pt) are preferentially deposited onto the {101} facets, while metal oxides (like PbO_2 and MnO_x) deposit onto {001} [82; 83]. The former are deposited via photo-reduction, while photo-oxidation leads to the deposition of the latter. This selective reactivity has been confirmed through the use of fluorescent molecules sensitive towards specific reactions [84], as well as through DFT calculations [85]. Thus it can be concluded that during the photo-activation process electrons are drawn preferentially towards the

{101} surfaces, while the holes accumulate on {001}. Hence, the presence of both surfaces is necessary for a good charge separation. In fact, for TiO_2 spheres with 100% coverage of {001} facets very poor photocatalytic activity is observed, unless Pt nanoparticles serving as electron-acceptor centres are deposited [86].

While there is plenty of information on the effects of {001} and {101} on the photocatalytic activity of TiO_2 nanoparticles, much less is known about how such crystallographic modifications affect the reactivity of polycrystalline TiO_2 films. An important part of this PhD thesis has been dedicated to this subject, and TiO_2 films, prepared reactive DC magnetron sputtering, are good model systems for such studies.

It has been reported in several studies that sputter-deposited anatase films exhibit preferential <001> orientation [87; 88; 89; 90]. Furthermore, the orientation can be fine-tuned by adjusting the preparation conditions. For example, during deposition at high temperatures, which directly yields crystalline anatase, the substrate bias can be used to alter the crystallographic orientation of the TiO_2 crystallites [90]. If the deposition is carried at room temperature, initially yielding an amorphous TiO_2 film, various sputtering parameters, such as the total pressure in the sputtering chamber, or the partial pressure of the reactive gas (O_2) can be used to induce growth in the <001> direction during a post-deposition heat treatment [87; 89]. This textured growth is an intrinsic property for sputter-deposited TiO_2 films and does not depend on the type of substrate used. It has been shown that even freestanding amorphous TiO_2 films deposited in this manner crystallize with preferential orientation upon heating [87].

If there is little information available on preparation techniques of <001> oriented TiO_2 films, even less can be found on its effect on their photocatalytic activity. However, at least in one report an improved photocatalytic degradation rate of acetaldehyde was observed in preferentially oriented sputter-deposited films [90].

4. Preparation and characterization of TiO_2 films

This chapter summarizes the main methods used for preparation and structural characterization of TiO_2 films. Some general results on the structural properties of the films used in the photocatalytic experiments, are also reported here.

4.1. Sample preparation techniques

4.1.1. Doctor – blading of anatase TiO_2 films

Some of the photocatalytic experiments were performed on 6.5 µm thick porous TiO_2 films. They were prepared by the Doctor - blading method, using a commercial nanoparticulate TiO_2 paste (DSL 18NR-T, Dyesol, Queanbeyan, Australia).

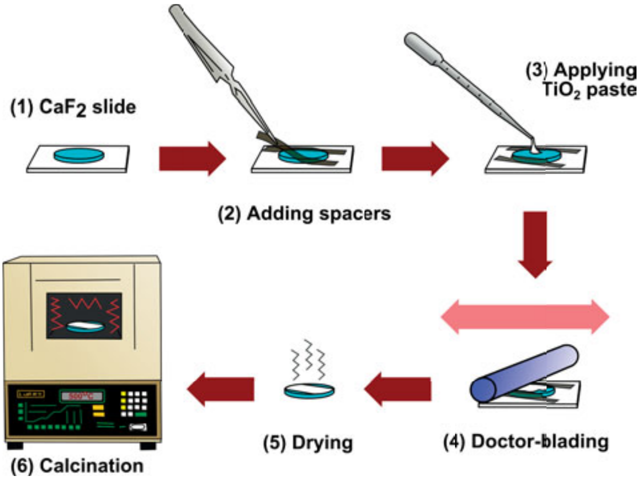

Figure 4.1: Doctor – blading of thick porous TiO_2 films from commercial nanoparticulate paste.

The Doctor-blading technique is a simple method to prepare films of viscous liquids. The name for this technique is derived from the term that describes a blade used in conjunction with ductor rolls in printing presses. Eventually "ductor blade" evolved into the term “doctor blade”. In rotogravure printing it controls the quantity of ink deposited onto the printing drum, by scraping off the excess and leaving a thin film on it.

The Doctor-blading procedure is shown in Figure 4.1. UV and IR transparent CaF_2 discs were used as a substrate. Prior to application of the TiO_2 paste a polymer tape with thickness of ~ 10 μm was adhered to the sides of the substrate. The tape acts as a frame and spacer, which determines the thickness of the final film. A small amount of paste is then deposited on top of the substrate, and a steel roller (or glass rod) is used to apply the paste homogenously over the surface, carrying away the excess. The films were then dried for 24h and heat treated in an oven according to the following protocol: 10 minutes at 180, 320 and 390°C and finally, at 450°C for 1h. This sequence is required to carefully evaporate the solvents and then burn off the polymer binders contained in the original paste.

4.1.2. Reactive DC magnetron sputtering

Direct current (DC) magnetron sputtering is a versatile physical vapor deposition (PVD) technique used to prepare coatings and thin films of many materials.

A conductive target, made of the material to be deposited (usually a metal or alloy), is placed in a chamber containing Ar gas (a.k.a. working gas) at a low pressure. The target serves as a cathode, while a metallic ring placed around it acts as the anode (Figure 4.2). When direct current is applied, the Ar atoms near the target are ionized and accelerate towards it. The energetic collisions result in the ejection of atoms from the target surface, and the generation of secondary electrons. The latter are trapped in the vicinity of the target in the magnetic field of a magnet positioned behind it (forming a magnetron, hence the name). This leads to subsequent re-ionization of Ar atoms, maintaining the plasma discharge and further enhancing the number of collisions between the ionized Ar atoms and the target. In this process more atoms are knocked (sputtered) away and deposited inside the vacuum chamber; and on the substrate, which is facing the target.

When an insulating material, such as TiO_2, is the desired product another gas, called a reactive gas, is also introduced into the chamber. In the case of TiO_2 this is O_2 gas. Since Ti has high affinity towards oxygen, the sputtered Ti atoms become oxidized during their trajectory from the target to the substrate, and TiO_2 is ultimately deposited onto the substrate.

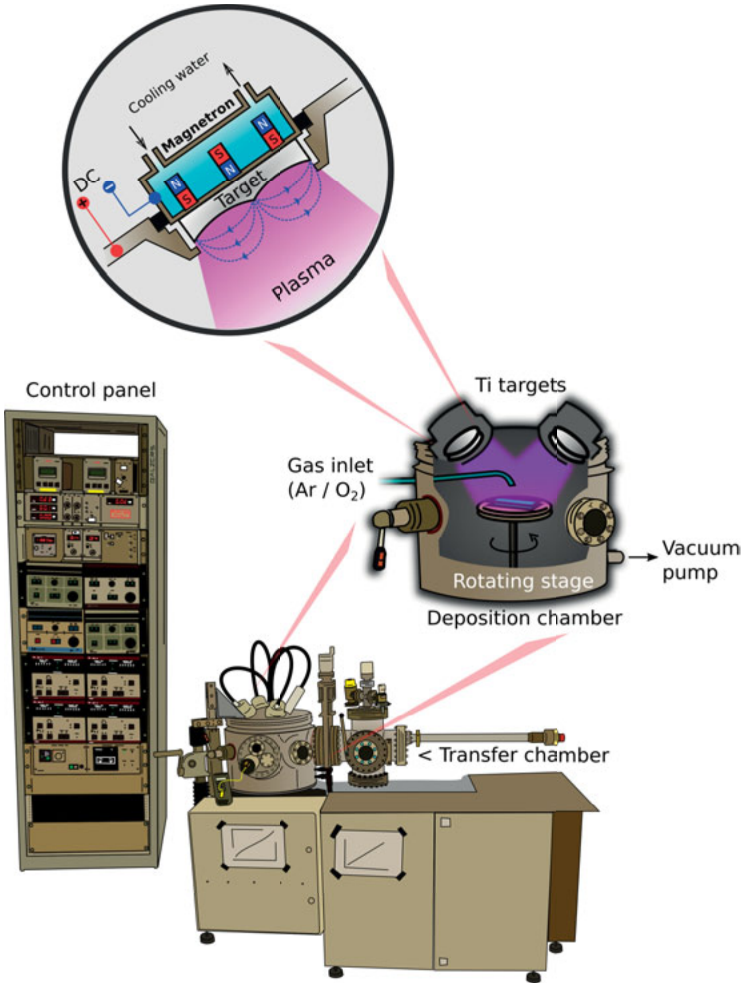

Figure 4.2: Overview of the Balzers UTT 400 sputtering unit.

The sputtered anatase TiO_2 films were deposited in a homemade sputtering setup based on the Balzers UTT400 vacuum unit [91]. Two Ti targets (5-cm in diameter, 99.995% Ti from Plasmaterials, CA, USA) were used as a pair. All depositions took place in an Ar / O_2 atmosphere, at a fixed sputtering current of 0.75A onto an unheated substrate, which was rotated during deposition in order to achieve a uniform coating.

The only deposition parameter that was varied in the present work was the partial O_2 pressure, P_{O_2}, which was adjusted by changing the O_2 flow entering the deposition chamber (eqn. 4.1).

$$P_{O_2} = \frac{[O_2]}{[Ar]+[O_2]} P_{tot}, \tag{4.1}$$

where $[O_2]$ and $[Ar]$ are the flow rates for the two gases, and P_{tot} is the total pressure in the chamber.

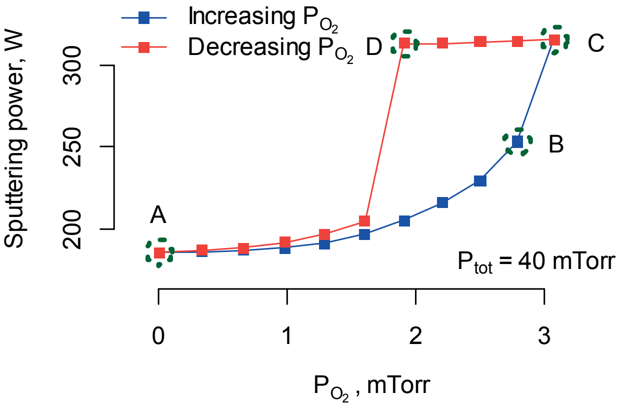

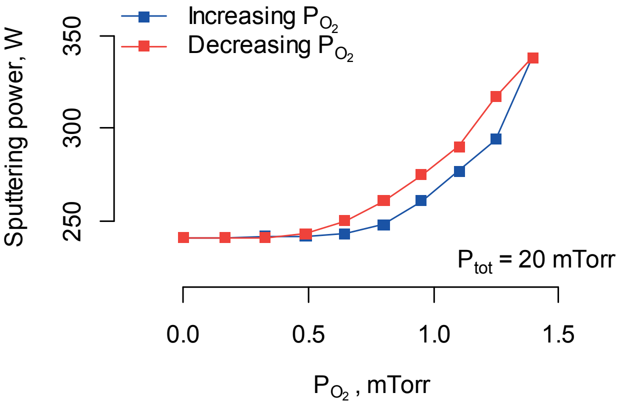

Figure 4.3: Process curves for $P_{tot} = 40\ mTorr$ (top), and $P_{tot} = 20\ mTorr$. At $P_{tot} = 40\ mTorr$ the sputtering regimes are (A) "metallic", where Ti and sub – stoichiometric TiO_x is deposited; (A → B) "reactive" – where TiO_x is deposited; (B → C) "reactive" with target poisoning, where low yields are expected, and the deposition becomes unstable; extending to (C → D) due to hysteresis. At $P_{tot} = 20\ mTorr$ the hysteresis is minimized, and deposition can be carried throughout the entire P_{O_2} range; hence $P_{tot} = 20\ mTorr$ was chosen for all sputtered TiO_2 films in this thesis. Note that the mass – flow range of O_2 is the same in both plots, and the difference in P_{O_2} is due to the higher P_{tot} - see eqn. 4.1.

The $[Ar]$ flow was fixed at 60 mL min^{-1}, while $[O_2]$ was in the range 1.75 – 6 mL min^{-1}. Thus, according to eqn. 4.1, P_{O_2} was in the range 0.56 to 1.82 mTorr, for $P_{tot} = 20\ mTorr$, which was kept fixed. The value of 20 mTorr was chosen in order to assure stable deposition condition in a wider P_{O_2} range.

If P_{O_2} vs. sputtering power (or the sputtering rate) is plotted, hysteresis loops are obtained, such as the ones shown in Figure 4.3. The shape of the hysteresis is determined by the adsorption – desorption equilibrium of O_2 on the Ti target, which in turn is determined by P_{O_2} and P_{tot}. This forms three sputtering regimes. At $P_{O_2} \approx 0$ (point A in Figure 4.3), the target is in "metallic mode" and the deposited films are either metallic Ti, or very sub – stoichiometric TiO_2. As P_{O_2} increases (points A → B in Figure 4.3) the sputtering condition enters the "reactive mode", where the desired compound, with stoichiometry determined by P_{O_2}, is deposited. In this region the O_2 coverage at the Ti target increases, and is determined by the ratio of the sputtering rate, and the O_2 adsorption rate. As P_{O_2} is further increased (points B → C), the O_2 adsorption rate exceeds the sputtering rate and an insulating layer of TiO_x is formed on the target surface; in extreme cases to the point where the glow discharge cannot be sustained. Then the target becomes poisoned (point D). As visible in Figure 4.3, at $P_{tot} = 40\ mTorr$ the target is easily poisoned, as reflected by the large hysteresis. At $P_{tot} = 20\ mTorr$ the hysteresis is small, and with a smaller slope; hence this is the more favorable condition to ensure a wide range of accessible P_{O_2} and to avoid poisoning of the Ti – targets and at the same time ensure reproducible deposition conditions.

As the deposition of TiO_2 films take place at fixed current, all of these processes lead to an increase of the sputtering power (which also resulted in a slight increase of the deposition rates, as shown by the data summarized in Table 4.1).

Table 4.1: Trends in deposition parameters, as a function of P_{O_2}. From left to right: partial oxygen pressure P_{O_2}, sputtering power P, film thickness d, sputtering rate r^{dep}. All parameters were obtained during 35 min of deposition at $P_{tot} = 20$ mTorr and fixed target current of 0.75A.

P_{O_2}, mTorr	P^{dep}, W	d, nm	r^{dep}, nm min^{-1}
0.64	211	574	16.4
0.95	223	579	16.5
1.25	244	664	18.9
1.53	291	697	19.9

The most obvious effect of P_{O_2} on the as-deposited films is that at lower oxygen content sub – stoichiometric films are formed. Figure 4.4 shows an example of four films deposited at increasing P_{O_2}. Sub – stoichiometric TiO_2 films are blue in color due to the presence of Ti^{3+} ions. Other of P_{O_2} on the structural and optical properties of the TiO_2 films will be discussed in detail in the following sections of this chapter.

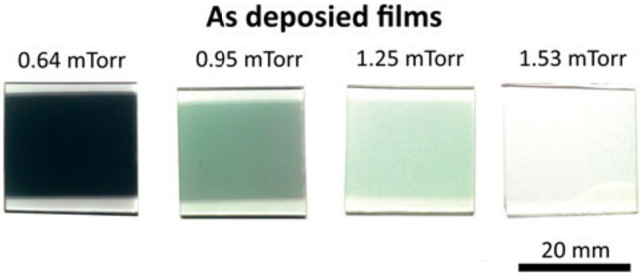

Figure 4.4. Photographic images of as-deposited anatase TiO_2 films prior to heat-treatment. Films deposited at low P_{O_2} were darker in color, due to the presence of Ti^{3+} and gradually turning transparent at equilibrium P_{O_2}, attaining stoichiometric composition. All films turned transparent, following the post-deposition heat-treatment for 1h at 500°C.

4.1.3. Preparation of SO_4 – TiO_2 films by SO_2 photofixation

The anatase TiO_2 films were sulfated by exposing them to SO_2 gas during UV illumination at elevated temperatures up to about 200°C. The experimental setup is presented at Figure 4.5. It consists of a stainless-steel vessel containing the sample holder. It is equipped with a heater and a thermocouple connected to a temperature controller. A quartz window is located directly above the sample where the UV source is mounted. The light source employed is a UV-LED matrix consisting of 24 UV LEDs (NS370L-5CLA, Roithner LaserTechnik GmbH, Vienna, Austria) with $\lambda = 370 \pm 12$ nm. The LED array is positioned at distance of 100 mm from the sample so that even light distribution is ensured.

The photofixation is carried in 50 ppm SO_2 atmosphere, 200°C sample temperature and continuous UV illumination. The reaction of SO_2 on TiO_2 under these conditions has previously been thoroughly investigated in our group [60] and normally results in about 2 at. % sulfur content in commercial, randomly oriented TiO_2 films. The following reaction scheme is suggested:

$$SO_2^{ad} + O_2 \underset{h\nu}{\overset{TiO_2}{\longrightarrow}} \begin{cases} SO_2 + O^{\bullet} + O_{vac} & \rightarrow Ti - SO_3 \\ SO_2 + O_2^{\bullet} + O_{vac} & \rightarrow Ti - SO_4 \end{cases} \tag{4.2}$$

UV irradiation creates oxygen vacancies on the surface by means of a hydroxyl condensation mechanism, where a protonated lattice O atom reacts with an adsorbed OH to yield water.

To a smaller extent heating, which is possible to apply up to the desorption temperature of adsorbed sulfate / sulfite species (around 300°C), also contributes to create O vacancies. Importantly this also helps to desorb excess water from the surface to allow for SO_2 adsorption and reaction with O vacancy sites [60]. SO_2 adsorbs on the surface where some of it reacts with O vacancies to form strongly bonded bridging bi-dentate SO_4 species [92]. Therefore, the TiO_2 films modified via SO_2 – photofixation will be referred to as SO_4 – TiO_2 in the rest of the thesis.

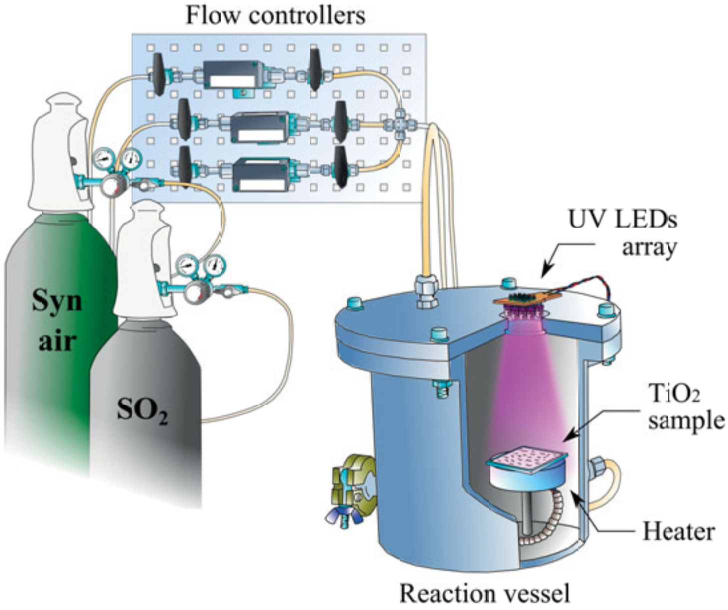

Figure 4.5: Laboratory set-up for SO_2 treatment of TiO_2 films

4.2. Grazing Incidence X-Ray Diffraction (GIXRD)

The phase composition and structure of the TiO_2 films were determined by means of GIXRD. X-ray diffraction is an important and widely used material analysis method in materials science. It is mainly used for characterization of the structure of crystalline and amorphous materials in their solid state.

XRD is based on the interaction of the material with a parallel beam of x-rays. The wavelength of the x-rays is usually in the order of the interatomic distances; hence they are diffracted by the crystalline structure. If the angle between the normal of a given crystalline plane and the falling x-ray beam fulfills the Bragg condition (Figure 4.6 and eqn. 4.3), constructive interference of the reflected waves occurs, and a spot is observed in the diffraction pattern.

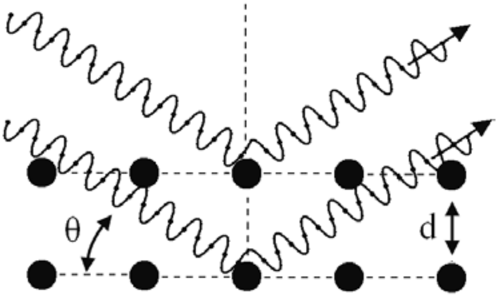

Figure 4.6: Bragg condition for x-ray diffraction

$$2d\sin\theta = n\lambda \tag{4.3}$$

The diffraction pattern as a function of angle of incidence is unique for each material and crystal structure. Thus diffraction patterns can be used to obtain interplanar distances, phase identification and other crystallographic information. The diffraction patterns are obtained using a device, called an x-ray diffractometer, which consists of an x-ray source, sample holder and a detector, mounted on a goniometer (Figure 4.7). It allows for the measurement of the angular dependence of the diffracted beam intensity, a.k.a. a diffractogram.

In GIXRD the scan is done at grazing incidence angle, meaning that the x-ray beam is falling at a very steep angle towards the surface and the scan is performed using the detector only. In that way GIXRD has high sensitivity for very thin samples. It is also possible for the depth to be probed systematically down to ten nanometers. The relation between the GI angle and the penetrated depth is given by eqn. 4.4.

$$\tau_{1/e} = \frac{\sin\alpha}{\mu} \tag{4.4}$$

Eqn. 4.4 expresses the depth at which the intensity of the x-ray beam will decrease to 1/e ($\tau_{1/e}$), and is determined by the grazing angle α and the linear x-ray attenuation coefficient for the given material, μ. Values for μ are tabulated for many materials and for TiO_2 (rutile) it is 0.0528 μm^{-1} (as determined with $CuK_{\alpha 1}$ = 1.541 Å radiation in the range of 22 – 60°). Thus if we would want to probe a very thin (100 nm) TiO_2 film the grazing angle should be about 0.3 – 0.5°.

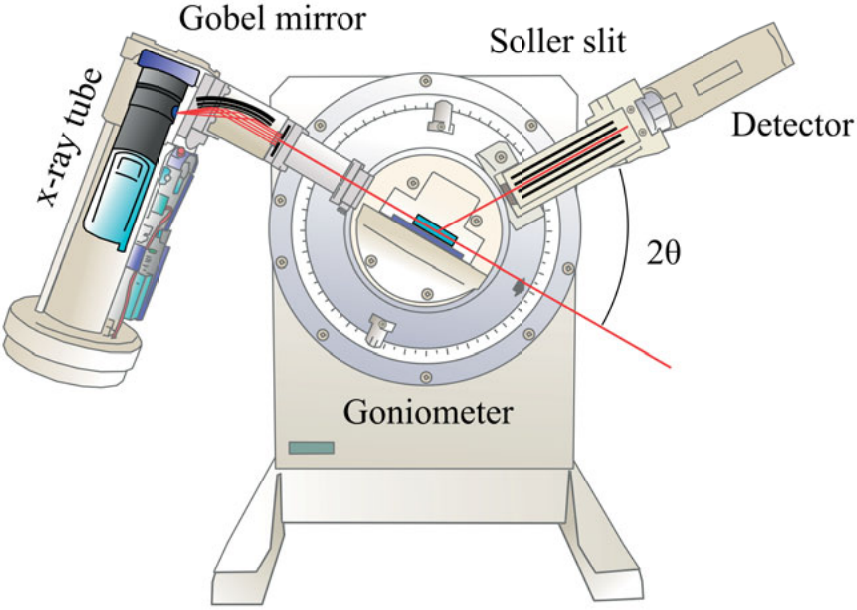

Figure 4.7: Operating principle of the x-ray diffractometer in the GI-XRD configuration.

The Doctor-bladed porous films were determined to be 6.5 μm thick (according to the profilometry measurements) so a grazing angle of 1° was used, while 0.5° was chosen for the sputtered samples, whose thicknesses were in the range 0.4 – 1 μm. In all cases the diffractograms were obtained in the 20 – 80° range (2θ). A typical diffractogram for polycrystalline anatase is presented in Figure 4.8. It is dominated by the reflection corresponding to the most abundant {101} plane.

To quantitatively analyze the diffractogram the Rietveld – refinement method can be employed [93]. Its principle is to calculate a diffractogram based on the crystallographic information for the expected phases, and to approximate it to the experimental data, using a number of fitting variables, such as crystallite size, strain, and other crystallographic parameters. The

PowderCell 2.4 software was used for Rietveld refinement in this thesis [94], along with a crystallographic data file for anatase [95].

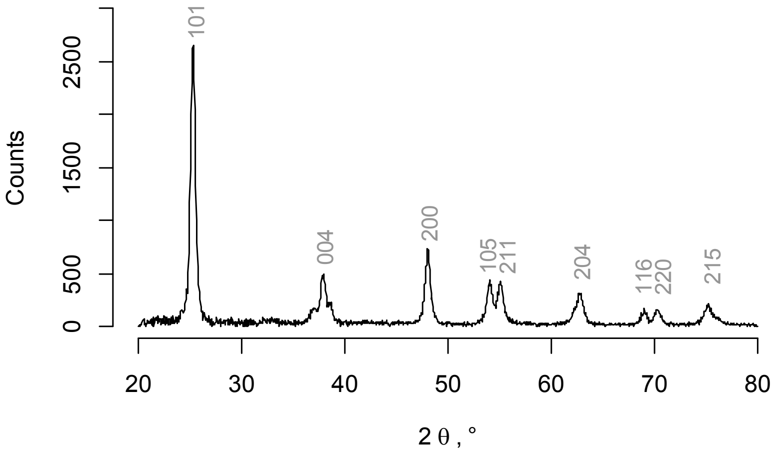

Figure 4.8: X-ray diffractogram of the Doctor-bladed DyeSol anatase films.

4.2.1. Determination of preferential <001> orientation using the March-Dollase model

The presence of preferential crystallographic orientation is usually clearly visible in XRD diffractograms. In powder samples and randomly oriented polycrystalline films the particles are facing the XRD beam in all possible orientations; hence the intensity of the characteristic peaks will be determined by the relative abundance of each diffracting plane. If a given crystallographic direction is preferred this will lead to an increase in the intensity of the corresponding reflection. Determining preferential orientation from XRD data in Rietveld refinement involves modifying the calculated XRD diffractogram with a distribution function, from which a set of intensity corrections for each reflection are calculated.

There are a number of distribution functions available, and in this thesis the March-Dollase (MD) model is used [96] (as integrated in PowderCell). It is suitable for the sputter-deposited samples, where the substrate is rotated during the deposition, as it is assumed that the sample has a cylindrical symmetry and the intensity of the peaks is the same across the rotational axis (i.e. if a 2D pole figure is made, rings would be observed).

The MD model uses the following distribution function:

$$W(\alpha) = (MD_{<hkl>}{}^2 cos^2\alpha + \frac{1}{MD_{<hkl>}} sin^2\alpha)^{-3/2}, \qquad (4.5)$$

where $MD_{<hkl>}$ is the MD parameter for the given <*hkl*> direction, and α is the angle, between this direction and the growth direction of the film. The solution of the MD function gives us the probability of finding a crystallite with the <*hkl*> direction at angle α, and several such plots are presented in Figure 4.9.

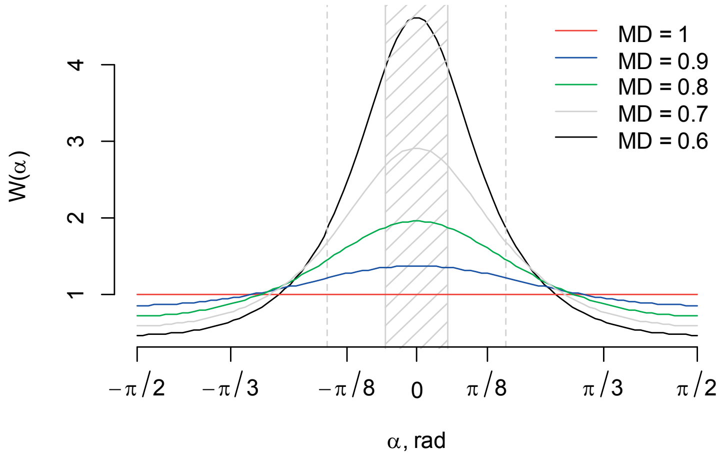

Figure 4.9: $W(\alpha)$ (eqn. 4.5) plotted for five different MD parameters. The increasing peak around 0 rad shows an excess of crystallites, whose <hkl> direction is parallel to the growth direction of the film. Dashed lines wrap the integration range, from which $\eta_{<hkl>}$ is calculated, and the filled area – the more narrow range, from which A_{001} is calculated within this thesis. The red line corresponds to a film composed of randomly oriented crystallites.

In randomly oriented films $MD_{<hkl>} = 1$ and the probability of finding <hkl> at any angle is the same (as shown in Figure 4.9). In preferentially oriented films, $MD_{<hkl>} < 1$, resulting in an increased probability to find crystallites with the corresponding direction parallel to the film plane. If the preferential orientation is in another crystallographic direction $MD_{<hkl>} > 1$. A schematic representation of the crystalline structure of a film with and without preferential orientation is shown in Figure 4.10.

$MD_{<hkl>}$ has a little physical meaning, but numerically integrating $W(\alpha)$ for a given $MD_{<hkl>}$ and range of α provides a number of useful parameters. One example is the degree of preferential orientation, $\eta_{<hkl>}$, defined as the excess of crystallites whose <hkl> direction points within an angle ±30° of the growth direction. As $W(\alpha) = 1$ when $MD_{<hkl>}$ = 1 the excess is defined against the randomly orientated samples, viz

$$\eta_{<hkl>} = \frac{\int_{-\pi/6}^{\pi/6} (W(a) - 1) da}{\int_{-\pi/2}^{\pi/2} W(a) da} \times 100\% \,, \tag{4.6}$$

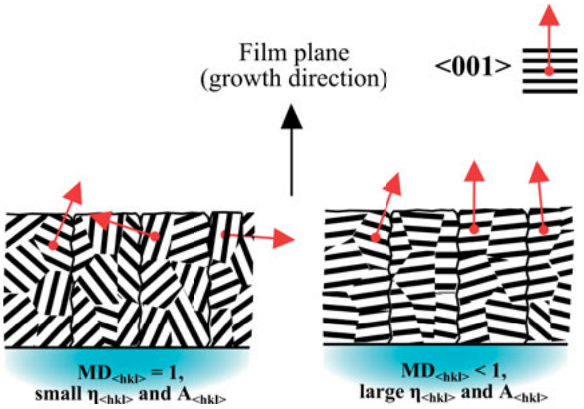

Figure 4.10: The increased preferential orientation leads to higher probability of finding a crystallite with the <001> direction parallel to the film plane. The $MD_{<001>}$ parameter, which is obtained during Rietveld refinement, is a figure of merit that can be converted into other useful parameters with physical meaning.

This integral has an analytical solution, called the Zolotoyabko equation (eqn. 4.7) [97], which is a simple way to convert $MD_{<hkl>}$ into $\eta_{<hkl>}$.

$$\eta_{<hkl>} = \sqrt{\frac{(1-MD_{<hkl>})^3}{(1-MD_{<hkl>}{}^3)}} \times 100\% \,, \tag{4.7}$$

As this thesis focuses mostly on sputtered films, which are thick and solid, it was necessary to convert $\mathrm{MD}_{<hkl>}$ into a descriptor for the surface abundance of some facets under interest. In order to do that two assumptions were introduced. Firstly, even though the XRD data is obtained from the volume of the film, we assume that the surface is simply a cross-section of the film, parallel to the growth direction. Secondly, particles with <hkl> direction, oriented at angles close to the growth direction will expose the corresponding {hkl} facet on the film surface.

The facet of interest in the thesis was the highly reactive {001} facet and we assumed that any particle whose <001> direction is within $\pm 10^{\circ}$ of the film plane would result in a {001} facet exposed on the surface. This integration range is derived from the Wulff construction of TiO_2, discussed in Section 3.3.

The following equation is then used to convert the MD distribution into a relative abundance of {001} facets at the film surface.

$$A_{001} = \frac{\int_{-\pi/18}^{\pi/18} W(a)da}{\int_{-\pi/2}^{\pi/2} W(a)da} . 100\% \,, \tag{4.8}$$

When eqn. 4.8 is solved for $MD_{<001>} = 1$ we determine that the abundance of {001} facets for a randomly oriented anatase film is about 10%, which is in agreement with the expectations in the literature [69].

4.2.2. GIXRD and Rietveld analysis of sputtered TiO_2 films

Sputtered anatase TiO_2 films were prepared using the sputtering parameters listed in Section 4.1.2. The as-deposited films were amorphous, as visible on the lowermost diffractogram in Figure 4.11. Upon heat treatment at 500°C the amorphous TiO_2 phase was converted into a single-phase polycrystalline anatase. As visible from the changing ratio of the (001) and (101) reflections in the GI-XRD diffractograms an increasing preferential <001> orientation is obtained, which is directly proportional to P_{O_2}.

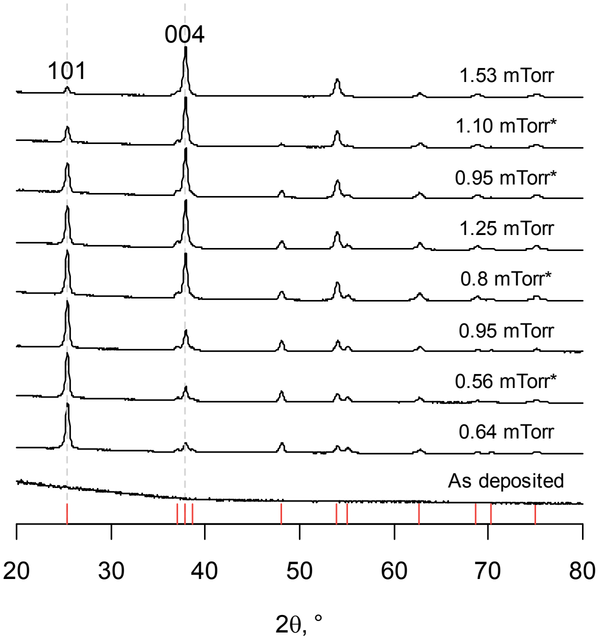

Figure 4.11: X-Ray diffractograms for anatase TiO_2 films, deposited at increasing P_{O_2}. Red bars indicate the positions of all intensive XRD reflections for anatase TiO_2, as obtained from literature data. [95]

Rietveld refinement of the diffraction data revealed that for increasing P_{O_2} the MD parameter decreased from 0.97 to 0.49. This corresponds to an increase of the relative fraction of crystallites with preferential <001> orientation from 2 to 38% and this relates to an increase of the relative area of exposed {001} facets at the film surface from 11 to 41%.

In order to confirm that this behavior is an intrinsic property of the sputter – deposited TiO_2 films, samples were deposited using two different sets of targets. The first was a set of unused Ti – targets, while the latter was extensively used (for about 20h) and exhibited the characteristic "race-track" features, due to surface erosion [98]. The eroded targets exhibit less active surface available for sputtering and are easily poisoned at higher O_2 content in the sputtering atmosphere, hence the P_{O_2} range in which they could be used was limited. As visible in Figure 4.12 the same linear dependence is observed for both sets of targets, for the relationship between P_{O_2} and the resulting A_{001} and η_{001} of the films.

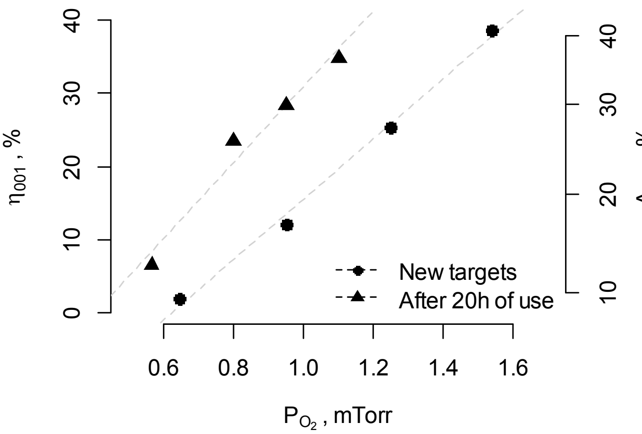

Figure 4.12: O_2 partial pressure, P_{O_2}, vs. amount of <001> preferential film orientation, η_{001}, and the ensuing relative abundance of {001} facets, A_{001}, for sputter deposition from two differently aged Ti targets. Lines are added to guide the eye.

In all cases the maximum achievable η_{001}, before further increase of P_{O_2} led to target poisoning, was about 40%. A possible explanation for this observation may be found in the nucleation and growth of anatase crystallites inside the amorphous matrix of the sputtered films. This growth is limited in each direction by the mean distance between nucleation sites. If a high number of nucleation sites are aligned in a certain crystallographic direction (such as <001>, which is the case in the preferentially oriented films), this may lead to contact between surfaces with high surface energies, or incommensurate atomic structure surfaces, and lead to lattice strain. This is visible in the lattice strain measured by GI-XRD. In films deposited at P_{O_2} = 0.65; 0.95; and 1.81 mTorr the strain was found to increase proportionally with P_{O_2} as 0.16, 0.17, and 0.21%, respectively.

It is reported in the literature that when anatase crystals are twinned along high-energy facets nucleation and growth of new phases may occur, as a mean to minimize stress in the structure. An example of this is the formation of rutile and brookite in anatase crystals twinned along {112} facets [99; 100].

We devised an experiment to see if rutile and brookite would be formed in sputter – deposited TiO_2 films, when achieving $\eta_{001} > 40\%$ was attempted. A single Ti target was used at $P_{O_2} = 1.6\, mTorr$ and $P_{tot} = 40\, mTorr$ (the equivalent of $P_{O_2} = 3.2\, mTorr$ for a deposition via pair of Ti targets).

Sputtering at such high oxygen content led to rapid poisoning of the Ti target, to the point where no plasma could be sustained. Nevertheless, an amorphous film with 200 nm thickness was obtained. A GI-XRD diffraction pattern of the film, after heat treatment for 1h at 500°C, is shown in Figure 4.13.

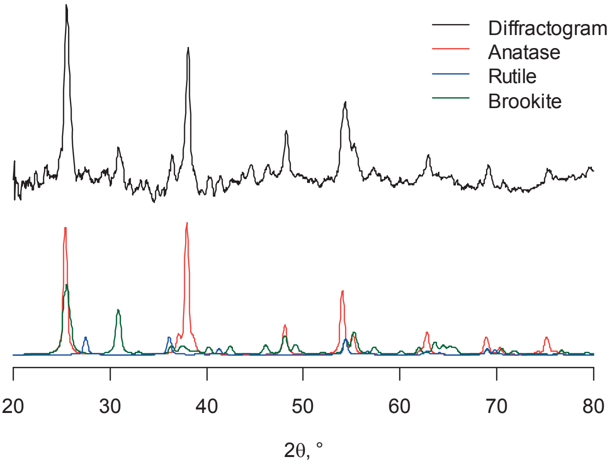

Figure 4.13: Diffractogram of a mixed – phase anatase – rutile – brookite TiO_2 film, prepared at $P_{tot} = 40\, mTorr$ and $P_{O_2} = 1.6\, mTorr$ (above), and the corresponding contributions of the respective phases, resulting from Rietveld refinement (below).

Rietveld refinement of the diffraction pattern reveals the film composition as: 52% anatase, 36% brookite and 12% rutile phase. The corresponding contribution of each phase in the diffractogram is shown in the bottom diagram in Figure 4.13.

Furthermore, all phases exhibited preferential orientation: 21% of the anatase crystallites oriented in <001> direction, 25% of the brookite oriented in the <111> direction, and 25% of rutile in the <101> direction.

Based on the alignment between the anatase <001>, brookite <111>, and rutile <101> directions a crystallographic model of the three-phase system can be devised. In order to achieve this, Rietveld refinement results were combined with theoretical and experimental predictions in the literature. Namely that in anatase – rutile mixed phases the most stable interface junction is anatase {101} || rutile {110} [101], while in anatase – brookite mixed phase systems it is anatase {101} ‖ brookite {210} [102; 103]. The ensuing model is shown in Figure 4.14.

The preparation of such mixed – phase TiO_2 films with high brookite content via sputter-deposition is interesting, since it is expected that brookite TiO_2 is a good photocatalyst with reactive surfaces. Furthermore, as discussed in Section 2.2, anatase – rutile mixtures are reported to exhibit higher photocatalytic activity than either of the two phases, due to charge separation effects at their junctions. It has been reported that anatase – brookite binary systems exhibit an enhanced photocatalytic activity due to the same effect [103].

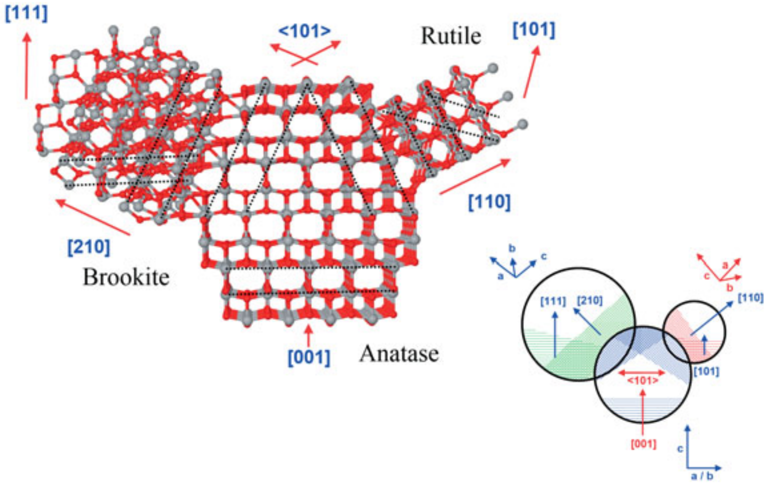

Figure 4.14: Growth model for the anatase – rutile – brookite film, prepared by reactive DC sputtering. The model was based on results for the preferential orientation of each phase, as obtained from Rietveld refinement and available data on the most stable interfaces for anatase - brookite and anatase – rutile phases.

Unfortunately, the mixed phase sputtered TiO_2 films turn out to be very challenging to produce in a consistent and predictable manner, due to the extreme sputtering conditions needed. As mentioned above, the high oxygen content in the sputtering atmosphere leads to severe poisoning of the Ti target and causes excessive heating, which may also damage the sputtering setup. Attempts to reproduce the result at milder $P_{tot} = 20\, mTorr$ were unsuccessful and only films with $\eta_{001} \approx 40\%$ were obtained, even at P_{O_2} which led to poisoning of the targets.

4.3. Transmission Electron Microscopy (TEM)

Transmission electron microscopy (TEM) is a technique routinely employed for characterization of materials at the sub-micrometer and nanometer level. The operating principle of a typical TEM is shown in Figure 4.15.

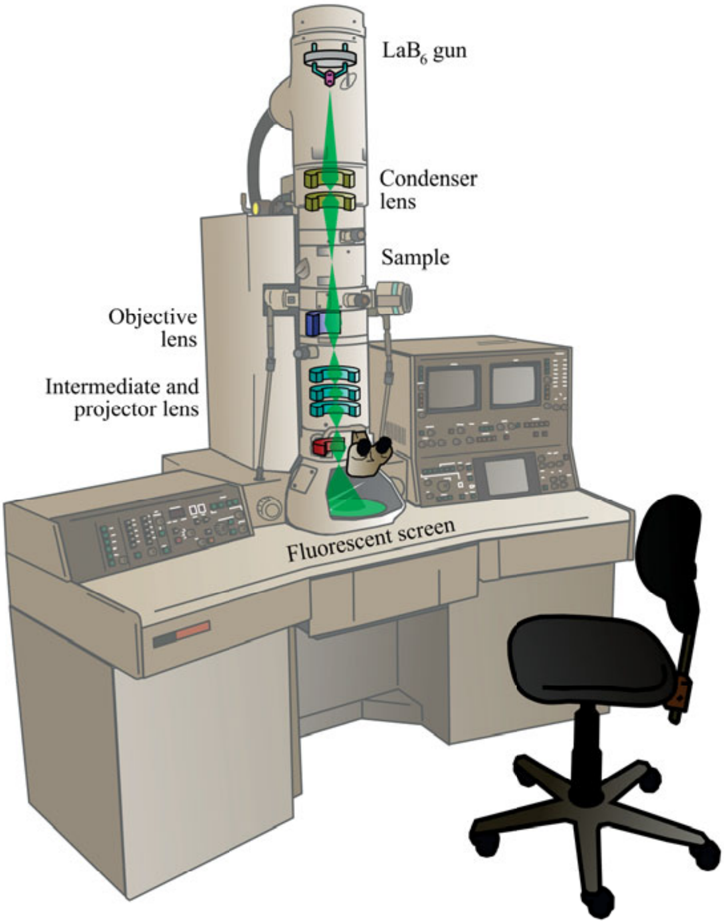

Figure 4.15: Operating principle of the transmission electron microscope

An electron beam is formed at the top of the column, usually by thermionic emission of a W or LaB_6 source. The emitted electrons pass through one or more cross-overs until a focused beam is formed. The optical system of the TEM bears resemblance to the one of an optical microscope. Electromagnetic lenses are used to focus and direct the beam through the sample. There are three groups of lenses: the condenser group, responsible for focusing the beam over the sample; the objective group, responsible for producing the image; and intermediate (and projector) lenses, responsible for the magnification.

The image is formed on a fluorescent screen, but a CCD camera is usually also present for digitalization. There are two basic modes in which any TEM can work – direct imaging, where a magnified image of the sample is formed and a diffraction mode, where the reciprocal space information, formed in the objective lenses back focal plane, is projected on the screen.

There are also three apertures (not shown in Figure 4.15). The condenser aperture determines how much of the electron beam will be directed towards the sample. The Selective Area Electron Diffraction (SAED) aperture is positioned in the objective lens image plane and allows selection of small areas of the sample, from which reciprocal space information can be extracted. The objective aperture, which is positioned in the back focal plane of the objective lens system, allows single spots of the diffraction pattern to be selected, allowing diffraction contrast imaging.

The transmission electron microscopy (TEM) measurements in this thesis were performed on a JEOL 2000FX II microscope, operating at an accelerating voltage of 200 kV.

4.3.1. TEM of commercial anatase TiO_2 nanoparticles

TEM samples were prepared by suspending ~1 μg of the DyeSol TiO_2 nanoparticulate paste, used for Doctor-bladed films preparation (Section 4.1.1), in 5 ml of acetone. The suspension was then sonicated for 15 min, in order to achieve uniform dispersion. A 400-mesh TEM grid, coated with a holey carbon film, (Agar Scientific, Stansted, UK) was then dipped into the suspension and dried in air. A selection of TEM images and the ensuing electron diffraction patterns is shown at Figure 4.16(a – d).

The particles were found to have a truncated tetragonal pyramidal shape, in good agreement with the Wulff polyhedron for anatase (Figure 4.16a). Distinct fringes separated by 3.5 Å were observed in the TEM images, which corresponds to the interplanar spacing of anatase in the <101> direction (Figure 4.16d), and shows that the particles have predominantly {101} facets exposed on their surfaces.

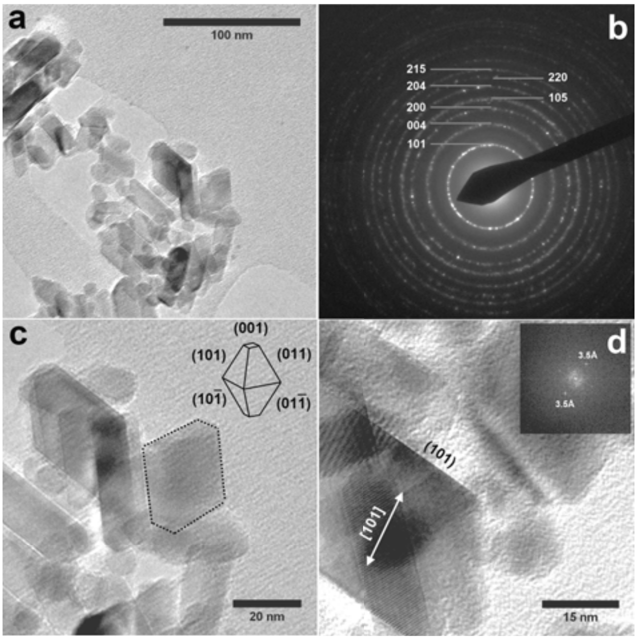

Figure 4.16: (a) Representative TEM images of anatase TiO_2 nanoparticles; (b) SAED pattern obtained from the image shown in panel (a) with the corresponding TiO_2 electron diffraction rings labeled; (c) high-magnification image of the particles in panel (a) with the truncated tetragonal bi-pyramidal shape of the nanoparticles and the corresponding Wulff reconstruction of the anatase particles (inset); and (d) atom-resolved lattice fringes showing the inter-planar spacing along the <101> direction.

4.3.2. TEM of sputtered anatase TiO_2 films with preferential <001> orientation

Samples for TEM microscopy of sputter-deposited anatase TiO_2 films were prepared by scraping the films of the substrate, and dispersing the scrapings in chloroform (>99%, Sigma Aldrich, MO, USA). The suspension was then sonicated, and left for few hours in order to allow any larger fragments to sediment. A holey carbon coated TEM grid (Agar Scientific, Stansted, UK) was then dipped in the suspension, dried, and imaged directly.

The sputtered TiO_2 films normally exhibit a columnar growth structure, when deposited at low temperature on a smooth substrate [104]. Hence, during the scraping the films crack easily along the growth direction and fragments with cross-sectional structure can be observed on the TEM grid. An example is given in Figure 4.17a, where the columnar structure is clearly visible.

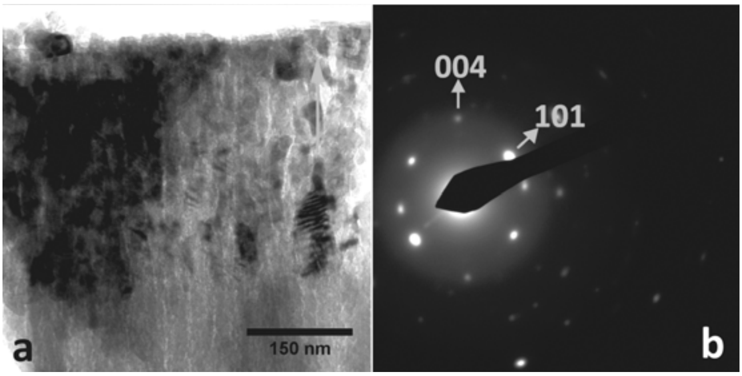

Figure 4.17: Cross-section TEM image of a highly oriented sputtered TiO_2 film (a), and the associated micro-diffraction pattern showing <001> orientation along the growth direction (b).

The high degree of preferential <001> orientation is also visible on the SAED diffraction patterns, which showed alignment between the (004) reflection, which is parallel to <001>, and the film growth direction (Figure 4.17b).

4.4. Scanning Electron Microscopy (SEM) and Energy-Dispersive X-ray spectroscopy (EDX)

An illustration of the operating principle of a typical SEM instrument is presented in Figure 4.18. Similarly to TEM, an electron beam is focused onto the sample by an optical system constructed of electromagnetic lenses. The main difference is that, here the electron beam spot can be spatially shifted in the *x* and *y* directions by a set of deflection coils, and scan the sample surface.

A number of phenomena occur during the interaction between the electron beam and the sample. Firstly, secondary electrons (SE) are generated through inelastic scattering of electrons. The SE are attracted towards a metallic mesh, kept at a positive potential, and the spatially-dependent current, measured between the cathode and the mesh is used to form an image of the sample. This is possible, because the number of SE emitted by the sample depends on the angle of incidence of the electron beam, which in turn is determined by the surface morphology of the sample.

Another outcome of the beam – sample interaction is the excitation of core electrons in the latter, leading to emission of x-rays. This is shown in Figure 4.18. These x-rays have energy, characteristic for each of the elements in the sample. Thus, information about the sample composition can be obtained by analyzing the spectra of emitted x-rays. A dedicated energy-discriminating detector is employed for this purpose. It is usually a Si diode, kept at low temperature by LN_2 cooling, as shown in Figure 4.18.

This outlines the basis of EDX spectroscopy, where the abbreviation EDX stands for energy dispersive x-ray spectroscopy (a.k.a. EDS and XEDS). Treating EDX data can be difficult due to the complicated processes of electron scattering and x-ray absorption the sample. However, elemental compositions and stoichiometry are routinely analyzed using this method.

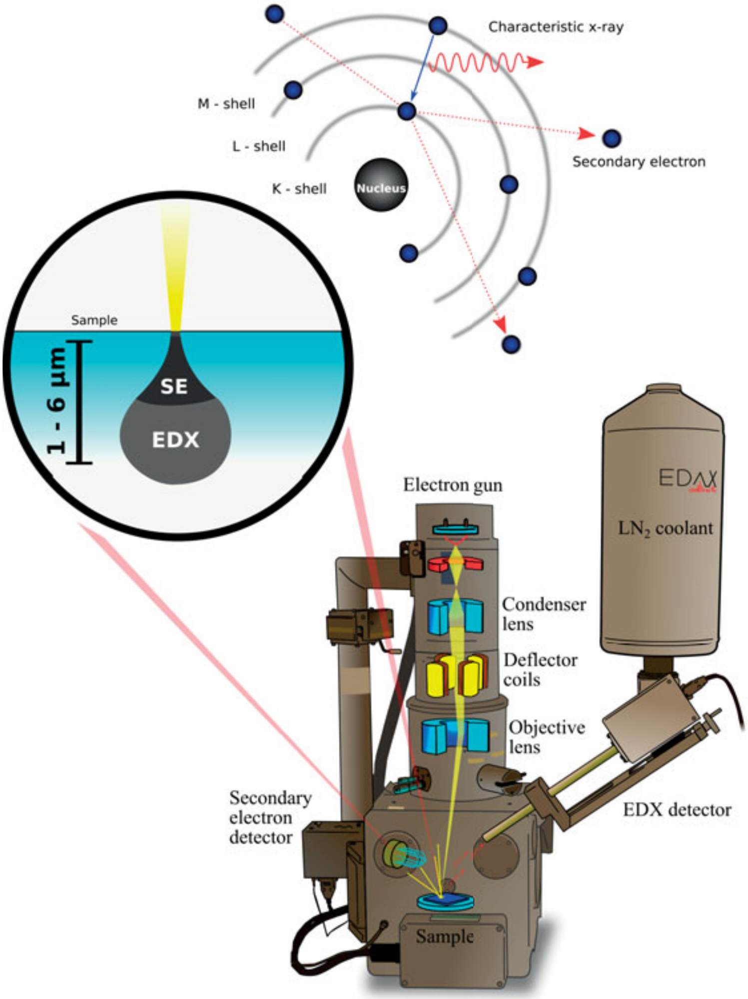

Figure 4.18: Operating principle of a scanning electron microscope equipped with an EDX detector. The inset shows the interaction between the focused electron beam and the sample in SEM. Among the products in the interaction volume secondary electrons (SE), and characteristic x-rays are used to form the image, and to obtain information about the elemental composition of the sample by EDX.

Figure 4.19(a, b) shows a comparison of the morphology of sputtered TiO_2 films, deposited at $P_{O_2} = 0.65\,mTorr$ and $P_{O_2} = 1.82\,mTorr$, respectively. The films consist of densely packed spherical protrusions with dimensions of the order of 100 nm. Cross-sectional images (Figure 4.19b) reveal that these features result from the columnar growth, which was observed in TEM as well. A representative TEM image is shown in Figure 4.19d for comparison. No obvious differences in morphology as a function of P_{O_2} were observed. Hence it can be concluded, that at $P_{tot} = 20\,mTorr$, the oxygen content in the deposition chamber has no decisive effects on the surface morphology of the ensuing TiO_2 films.

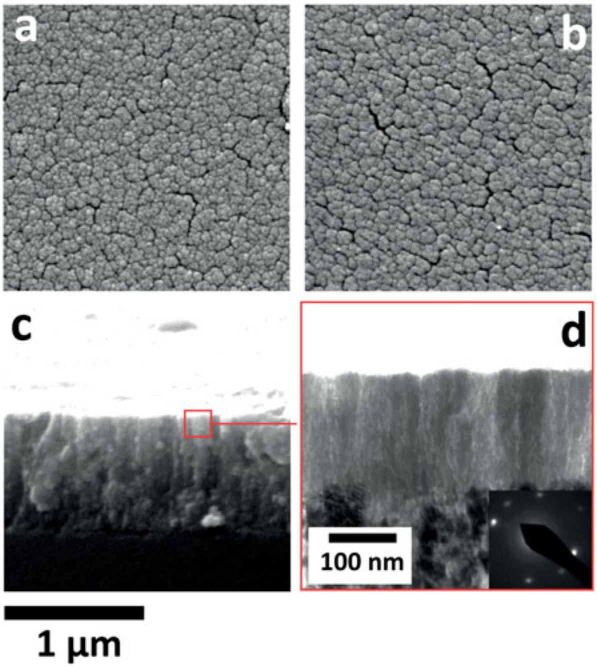

Figure 4.19: SEM micrographs showing surface morphologies of TiO_2 films deposited at P_{O2} of (a) 0.65 mTorr and (b) 1.82 mTorr. Representative cross-sectional images from (c) SEM and (d) TEM for a film with highly preferential orientation, prepared at P_{O2} = 1.82 mTorr. The inset in (d) shows a selected-area electron diffraction pattern and demonstrates the <001> preferred orientation.

Attempts to determine the stoichiometry of the as-deposited TiO_2 films by SEM – EDX proved to be challenging. The tinted films (Figure 4.4) were prone to rapid bleaching in air within few hours after deposition. This is due to the oxidation of Ti^{3+} by oxygen in the air. In few successful measurements, stoichiometry of $TiO_{0.9}$ and $TiO_{1.5}$ was obtained for two films, deposited at $P_{O_2} = 0.5\,mTorr$ and $P_{O_2} = 1.8\,mTorr$, respectively.

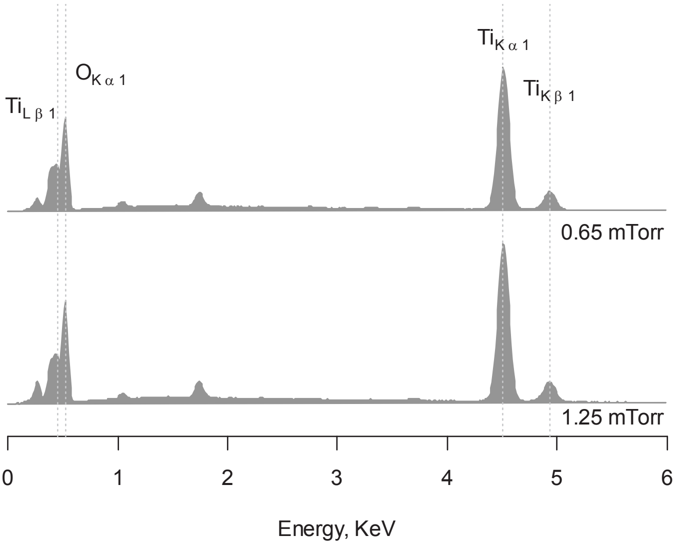

Figure 4.20: EDX spectra of anatase TiO_2 films deposited at two different P_{O2} settings. The post annealed films exhibited the same stoichiometry.

After post-deposition heat treatment in air at 500°C all films exhibited the same stoichiometry, corresponding to TiO_2. Figure 4.20 shows EDX spectra, obtained after the heat treatment of films deposited at $P_{O_2} = 0.65\, mTorr$ and $P_{O_2} = 1.25\, mTorr$, respectively.

4.5. Atomic Force Microscopy (AFM)

Information about the surface morphology of sputtered TiO_2 films was obtained by atomic force microscopy (AFM). In AFM three-dimensional images of the surface are obtained. The image is formed by measuring the interaction of a cantilever with atomically sharp tip with the sample surface.

The typical AFM setup consists of three major components, shown in Figure 4.21. These are: an X – Y sample positioning stage; an optical microscope employed for targeting the areas of interest; and a scanning head, which is comprised of the cantilever and an optical system used to monitor its deflection. This deflection is measured by the displacement of a laser beam, which is bounced off the shiny surface of the cantilever. The scanning head is equipped with a piezo-actuator, which allows its positioning in X – Y – Z with a sub – nanometer precision.

Normally the AFM imaging is done in a non-contact mode. The cantilever is forced to oscillate at its resonant frequency, which is then optically monitored via the reflected laser beam. When its tip is in proximity with the sample van der Waals interactions occur, causing a shift in the resonant frequency. As this frequency shift depends on the tip – to – sample distance, it is used as a feedback in repositioning the cantilever in the Z direction in order to ensure a constant distance to the surface. The X – Y spatial dependence of the Z deflection needed to keep the resonant frequency constant is then used to create the 3D image describing the surface topology of the sample.

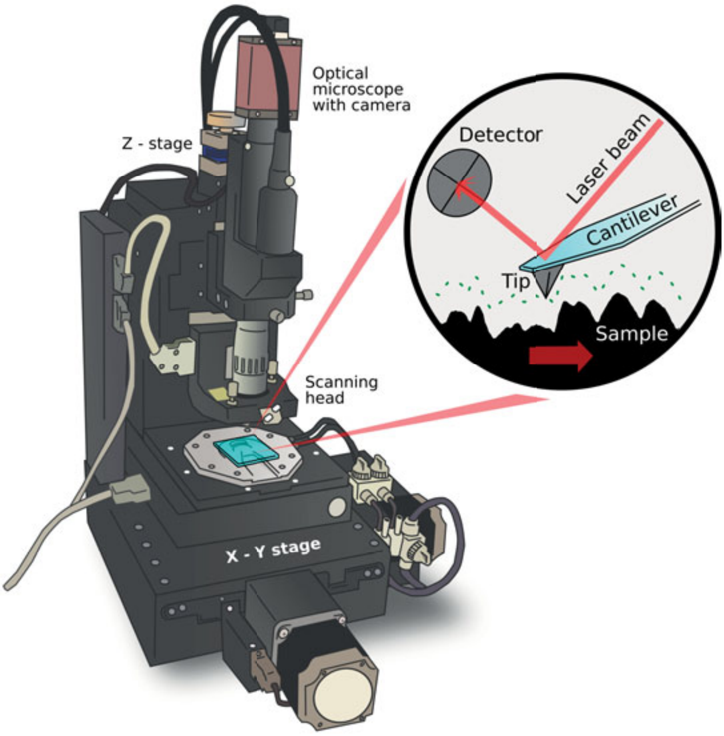

Figure 4.21: Operating principle of an atomic force microscope.

AFM images were obtained in a non-contact mode on a PSIA XE150 SPM/AFM (Park Systems Corp, South Korea) instrument, equipped with a Si ACTA cantilever (6 – 10 nm tip radius from AppNano, USA). An area of 1000 x 1000 nm was imaged at a resolution of 256 × 256 pixels.

In order to obtain statistically significant results, the data from at least six images obtained at random positions was averaged, and two parameters that quantitatively describe films surface roughness and morphology were calculated. The first parameter was the root mean square (r. m. s.) surface roughness ($R_{r.m.s.}$), which is a typical figure-of-merit of AFM surface roughness. It is defined as the average r. m. s deviation from the average surface height (eqn. 4.9)

$$R_{r.m.s.} = \sqrt{\frac{1}{n}\sum_{i=1}^{n} y_i^2} \tag{4.9}$$

$R_{r.m.s.}$ reflects on the average height or depth of the surface features, but it does not completely take into account the spacing between them. Thus, sometimes different morphologies may result in an identical value of $R_{r.m.s.}$ value. This requires the introduction of the average surface wavelength, λ_q (eqn. 4.10), which is defined as $R_{r.m.s.}$ roughness divided by the average surface slope Δ_q (eqn. 4.11).

$$\lambda_q = 2\pi\frac{R_q}{\Delta_q} \tag{4.10}$$

$$\Delta_q = \sqrt{\frac{1}{N-1}\sum_{N-1}\left(\frac{\Delta Z}{\Delta x}\right)^2} \tag{4.11}$$

λ_q is inversely proportional to the frequency at which the features giving raise to $R_{r.m.s.}$ are found at the surface. For example, the densely packed spherical protrusions which are observed in sputtered TiO_2 films. A graphical representation of the physical meaning of both $R_{r.m.s.}$ and λ_q is shown in Figure 4.22.

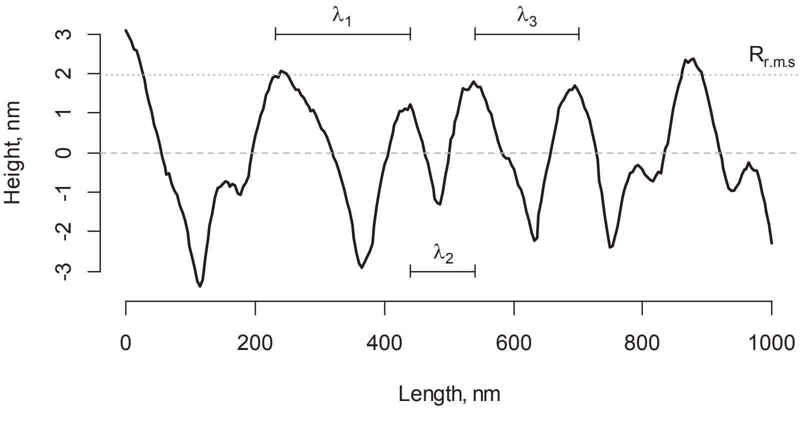

Figure 4.22: A single scan from an AFM image. The $R_{r.m.s.}$ (dotted line) is calculated as the mean deviation from the baseline. The average surface wavelength represents the average distance between two subsequent peaks (i.e. on this image it is the average of λ_1, λ_2, λ_3, and any other unlabeled peak – to – peak distances for any two subsequent peaks) and is inversely proportional to the frequency, at which the surface features associated with $R_{r.m.s.}$ are found at the surface.

A selection of AFM images of four TiO_2 films sputtered at increasing P_{O_2} (0.64 – 1.53 mTorr) is presented in Figure 4.23. They are in line with TEM and SEM observations.

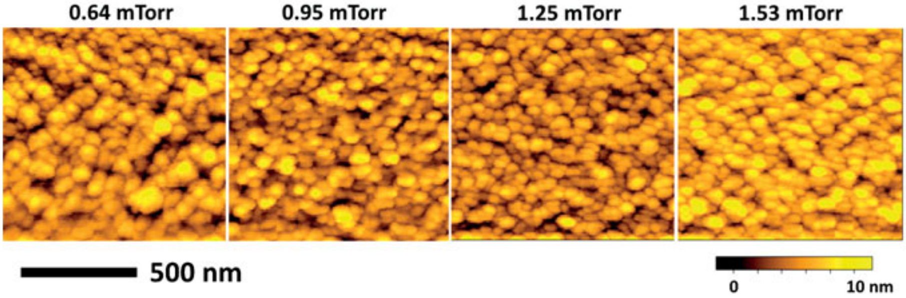

Figure 4.23: AFM images of four TiO_2 films, deposited at increasing P_{O_2}.

The corresponding values of $R_{r.m.s.}$ and λ_q, as a function of P_{O_2}, are listed in Table 4.2. The small decrease in λ_q, proportional to P_{O_2} implies that films deposited at lower P_{O_2} are coarser. This, however, is negligible; hence it can be concluded that P_{O_2} does not influence the surface morphology significantly, which is in line with the observations from SEM.

Table 4.2: Summary of $R_{r.m.s.}$ and λ_q values, obtained via AFM for TiO_2 films sputter deposited at increasing P_{O_2}.

P_{O_2}, mtorr	$R_{r.m.s.}$, nm	λ_q
0.64	1.3	77.9
0.95	1.1	75.6
1.25	1.4	73.9
1.53	1.6	71.3

4.6. Surface profilometry

The surface profilometry, a.k.a. stylus profilometry, is similar in principle to AFM. Here a probe, sometimes called a stylus, is once again brought into contact with the surface of the sample. The probe is attached to an X – Y – Z positioning stage, and moved across the surface at a steady rate. Its vertical displacement is converted electrically or optically into a signal, and changes in the signal correspond to variations of surface height. Surface profilometry has lower resolution than AFM and usually height data is obtained only in one dimension. However, the method is suitable for rapid screening of film thicknesses.

A Dektak XT Advance (Bruker, Tucson, AZ, USA) profilometer was used to measure thicknesses of the sputtered TiO_2 films immediately after their deposition, in order to calculate sputtering rates. In order to determine the average film thickness over the whole coated area UV/Vis spectroscopy was employed, as described in the following section.

4.7. Optical measurements

Information about the optical properties of sputtered TiO_2 films was obtained via UV/Vis spectrometry. The instrument was a Perkin Elmer Lamba 900 double-beam double-monochromator spectrometer, equipped with a 150-mm in diameter $BaSO_4$ coated integrating sphere, allowing for diffuse reflectance measurements.

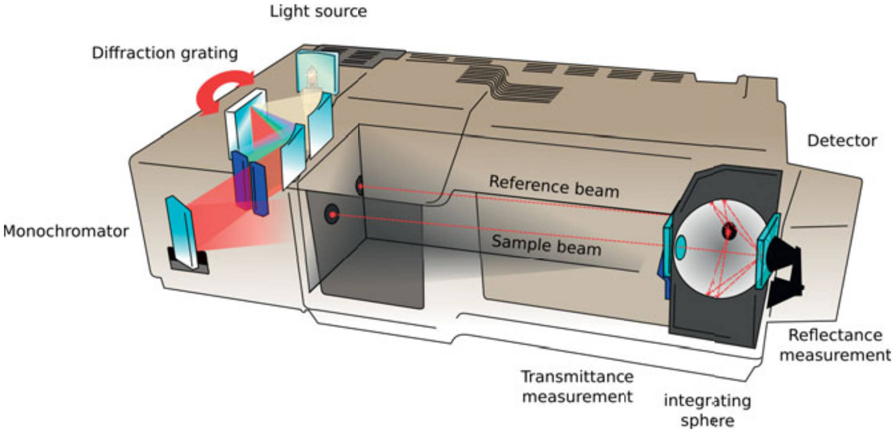

Figure 4.24: Operating principle of a UV/Vis spectrometer.

An overview of a typical spectrometer is presented in Figure 4.24. It consists of a light source covering the desired range, which is 300 nm < λ < 800 nm in UV/Vis spectrometry. The light from the source is passed through a monochromator, which allows allowing for a single wavelength to be selected and passed through the sample for transmittance measurements. An integrating sphere is employed in order to obtain diffuse reflectance measurements. The intensity of the monochromatic light after the interaction is measured by a dedicated detector.

In a typical run, the intensity of the light source is measured one wavelength at a time, prior (I_0) and after (I) interaction with the sample. The transmittance (T) and reflectance (R) are then defined as:

$$\mathrm{T}, \mathrm{R} = \frac{I}{I_0}\, 100\% \,. \tag{4.12}$$

In order to calculate the refractive indices and porosities of the sputtered TiO_2 films, transmittance and reflectance spectra were obtained in the range 300 to 800 nm. As the films were of thickness comparable with the wavelengths of the visible range both spectra exhibited interference fringes, as shown in Figure 4.25.

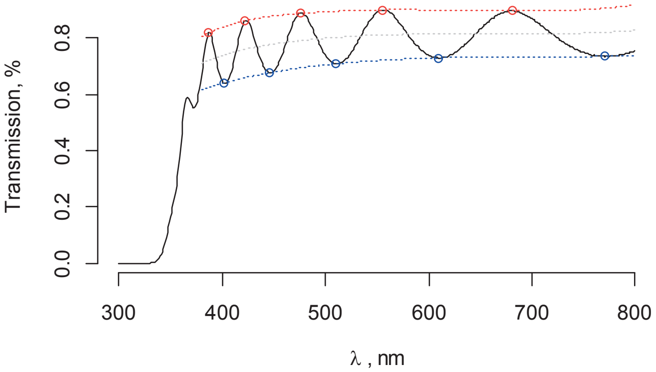

Figure 4.25: Typical result for a transmittance spectrum of a sputtered TiO_2 film. Red and blue dotted line show the envelope functions, fitted through the minima and maxima of the interference fringes.

Information about the positions of these fringes allows for the refractive indices of the films to be obtained, via the envelope method suggested by Swanepoel [105]. The first step is fitting the positions of the maxima and minima of each interference fringe with a set of interpolating spline functions, enveloping the spectra (as shown in Figure 4.25). The refractive index is then be obtained by using eqn. 4.13.

$$n = [N + (N^2 - s^2)^{1/2}]^{1/2} \tag{4.13}$$

Here s is the refractive index of the substrate and N is obtained from the envelope functions via eqn. 4.14.

$$N = 2s\,\frac{T_{max} - T_{min}}{T_{max}T_{min}} + \frac{s^2+1}{2} \tag{4.14}$$

Here T_{max} and T_{min} are the numerical values of the enveloping spline functions that represent the maximum and minimum at a given wavelength in the transmittance spectrum.

The refractive index of the substrate, s, is calculated from a transmittance spectra of the uncoated glass substrate, according to eqn. 4.15.

$$s = \frac{1}{T} + \left(\frac{1}{T^2} - 1\right)^{1/2} \tag{4.15}$$

Here T is the transmittance of the uncoated substrate at a given wavelength.

All refractive indices were averaged in the range 500 < λ < 700 nm. As mentioned in Section 4.1.2, films were deposited at two types of substrates. The first were 1-mm thick microscope slides, with $n = 1.53$, and the second – 4-mm thick OptiWhite$^{\text{TM}}$ glass substrates, with $n = 1.56$.

The average film thickness can also be calculated from transmittance data, according eqn. 4.16.

$$d = \frac{\lambda_m \lambda_{m+1}}{2(\lambda_m n_{m+1} - \lambda_{m+1} n_m)} \tag{4.16}$$

Here λ_m and λ_{m+1} are the wavelengths of any two consecutive minima and maxima, and n_m and n_{m+1} are the refractive indices at these wavelengths (as obtained from eqn. 4.13).

In thin films, their porosity has a determining role on the refractive index, hence we can use the value of the refractive index and calculate the film packing density (ρ), through Pulker's equation [106] (eqn. 4.17).

$$\rho = \frac{\rho_f}{\rho_b} = \frac{n_f^2 - 1}{n_f^2 + 2} \cdot \frac{n_b^2 + 2}{n_b^2 - 1}, \tag{4.17}$$

where ρ_f and ρ_b are the densities of the film and the bulk anatase, and n_f and n_b are the refractive indices of the film and the bulk anatase, respectively (for anatase $n_b = 2.56$, according to literature data [107]).

The optical bandgap, E_g, can also be calculated from the energy dependence of the absorption coefficient of the films (eqn. 4.18), according to Hong *et al* [108].

$$\alpha = \frac{1}{d} \ln(\frac{1-R}{T}) \tag{4.18}$$

Here R and T are the reflectance and transmittance for a given wavelength, and d is the thickness of the film. Since anatase is an indirect bandgap semiconductor, the plot of $\sqrt{\alpha E}$ vs. the photon energy ($E = 1240\,\lambda^{-1}[eV]$) should yield a linear dependence, assuming a parabolic band dispersion, which is a good approximation near the band-gap edge ($E > E_g$).

Figure 4.26 shows Tauc plots for films deposited at $P_{O_2} = 0.65\ mTorr$ and $P_{O_2} = 1.3\ mTorr$.

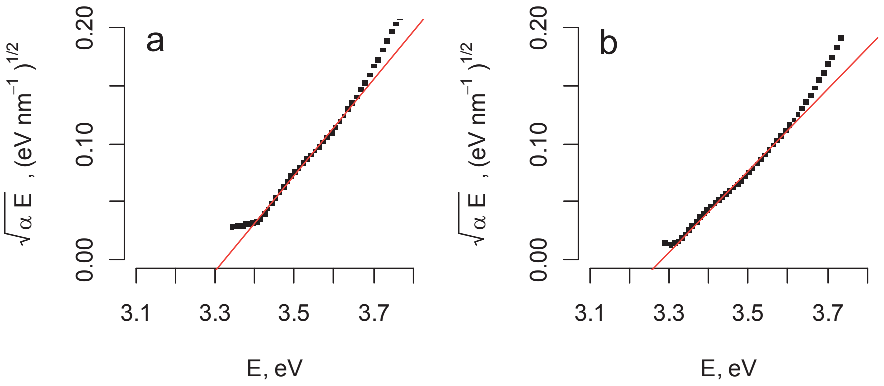

Figure 4.26: Tauc plots of $\sqrt{\alpha E}$ vs. photon energy, E, and linear fits of the data for TiO_2 films, deposited at (a) $P_{O_2} = 0.65\ mTorr$ and (b) $P_{O_2} = 1.3\ mTorr$.

Fitting a linear regression in the region $E = 3.4 - 3.6$ eV, and extrapolating to $\sqrt{\alpha E} = 0$ yields $E_g \approx 3.3\ eV$, which is in good agreement with the expected value for bulk anatase TiO_2 ($E_g = 3.2\ eV$).

4.8. Fourier – Transform Infrared Spectroscopy (FTIR)

Infrared (IR) spectroscopy is widely used in chemical and physicochemical analysis. Most laboratory IR spectrometers work in the range of 400 – 4000 cm^{-1} (2.5 – 25 µm), corresponding to the fundamental vibrational modes of the molecular bonds. While in UV/Vis spectroscopy the bands corresponding for the electronic transitions are noticeably broadened due to their overlap with translational and rotational degrees of freedom, the IR vibrations produce a clear spectrum with sharp, well-defined peaks, easy to interpret and associate with the molecular structure. This makes the IR spectroscopy a powerful tool for a whole array of investigations on molecules and their interaction.

In Fourier-transform IR (FTIR) spectroscopy a multitude of frequencies are recorded simultaneously. In dispersive IR spectroscopy the sample is exposed to monochromatic light at one wavelength at a time. In FTIR spectroscopy polychromatic light is passed through the sample and then, through a device, called a Michelson interferometer (Figure 4.27). It is constructed of a beam splitter and two mirrors – one stationary and one movable. The beam is split into two beams with 50% of the original intensity and then reflected back of each mirror through the beam splitter and the detector. If both mirrors are at the same distance of the beam splitter the beam will not interfere with itself. If the movable mirror is retracted, this result in a difference between the two beam paths (retardation), and this leads to interference. By accurately recording and adjusting the retardation of the mirror by a reference laser beam with known wavelength (usually a HeNe laser), an interferogram is formed. The resolution of the retardation, Δx, and hence the IR interferogram, is determined by the wavelength of the reference HeNe laser, and its co-sinusoidal interferogram, by digitizing the interferogram *exactly* at the zero-point crossings of the laser interferogram. The interferogram contains the recorded path difference of all possible wavelengths and can be transformed back into frequency space by Fourier transform (hence the name FTIR), and an absorption spectrum can be restored.

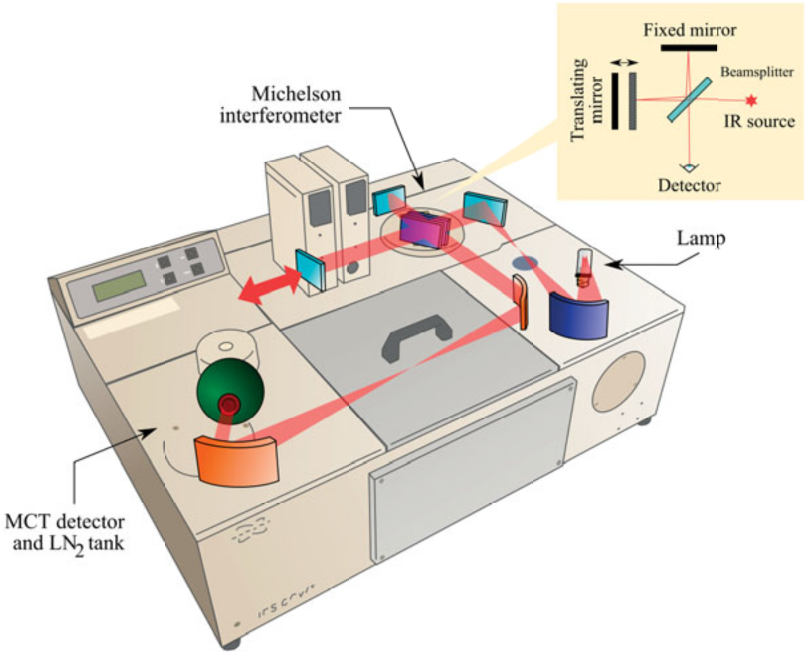

Figure 4.27: Operating principle of a laboratory FTIR spectrometer.

In comparison with dispersive IR spectrophotometers FTIR spectrophotometers give several advantages, which have more or less made dispersive IR spectrophotometers obsolete. Three main advantages may be distinguished:

1. FTIR spectrophotometers have an intrinsically precise wavelength scale, since the sampling interval, Δx, is determined by the zero-crossings of the reference HeNe laser interferogram, and is thus precisely determined by the laser wavelength which is intrinsically highly accurate. The point spacing, $\Delta \bar{\upsilon}$, in the resulting spectrum in frequency space is inversely proportion-

al to Δx, and hence the wavenumber scale is very precise, or the order $1/100 \cdot \bar{\upsilon}$. This advantage is called Connes' advantage.

2. The larger, circular IR beam apertures employed in FTIR spectrophotometers compared with the slits used in dispersive spectrophotometers, implies a significantly higher throughput. This advantage is called Jaquinot's advantage.

3. When measuring a signal whose noise is dominated by detector noise (and not limited by shot noise, determined by discrete electronic transitions, as in detectors for UV-Vis spectrophotometers), an improved signal-to-noise ratio (S/N) is realized in a FTIR spectrophotometer compared to dispersive instrument. This improvement of S/N is due to two effects. First, by taking multiplexed measurements (mixed wavelength measurements, as in FTIR), rather than discrete measurements at each wavelength (as in dispersive), the S/N is increased proportionally to the square root of the number of sampling points. Second, in a monochromator measurement the signal will be noisy at the peak of the emission line, since the noise is proportional to the square root of the signal (and, for the same reason, less noisy at the baseline of the spectrum). In a multiplexed measurement the noise is spread more or less evenly across the spectrum regardless of the local signal intensity. Thus, multiplexed measurements can achieve higher S/N at the emission line peaks. The S/N advantage is called Fellgett's advantage, or the multiplex advantage.

5. Determination of photocatalytic activity

Photocatalytic efficiency can be reported in many ways. A useful quantity is the quantum yield, which is simply the ratio of the number of reacted molecules and the number of absorbed photons. For practical purposes these are quantified by the corresponding rates (i.e. rate of molecular transformation) and photon flux, respectively. The problem in photocatalysis is that the number of active catalytic sites is unknown, and maybe changing under illumination. Hence, usually it is approximated by the number of adsorption sites in BET measurements, surface hydroxyl groups, or by the catalyst mass, which is, by no means an exact measure, and usually results in a lower limit of the quantum yield, by e.g. assuming that all adsorption sites in isothermal adsorption-desorption measurements are photoactive. For the purpose of comparing the effectiveness of different photocatalysts the photonic efficiency, and in particular relative photonic efficiency, have been introduced as an alternative to quantum yield [109]. In this case it is, however, important to report the experimental conditions of the photocatalytic experiments.

Three *in situ* approaches were used to determine the photocatalytic performance of TiO_2 films in the thesis:

- Transmittance FTIR measurements – used to investigate the adsorption and photo degradation mechanism(s) of acetaldehyde (CH_3CHO) on TiO_2, and the effect of the SO_4 surface modification. This method was only used with Doctor – bladed films of the commercial DyeSol photocatalyst.
- Liquid-phase tests with methylene blue (MB) dye for screening the effect of preferential <001> orientation on the intrinsic activity of sputtered TiO_2 films.
- Gas-phase photocatalytic tests with CH_3CHO gas in flow mode with a semiconductor VOC gas sensor for detection. This approach was used to investigate the “photocatalytic” window concept, and the combined effects of both film structure and operando conditions (surface temperature; RH; preferential <001> orientation; and SO_4 modification). For some experiments it was used in combination with FTIR to detect any possible gas-phase intermediates.

Both the operational principles of these three setups, and the methods used to treat the raw data obtained by each of them are described in this chapter. We report rate constants of photocatalytic reactions for the purpose of comparing changes of efficiencies under identical reaction conditions and for similar samples. We do not consider the number of active catalyst sites per unit area. As mentioned above, the photonic efficiency is easily obtained by dividing reaction rates by the reported incident photon flux, but this adds nothing to the inter-sample comparison. In the cases where rates are presented per unit area the geometric surface area is implied, and it does not reflect the number of catalytic active centers (as estimated by the methods mentioned above). In other cases the kinetic rate constants are reported.

5.1 Transmission in situ FTIR photocatalytic measurements

In situ measurements in transmittance mode were performed using a Bruker IFS66v/S FTIR spectrometer (Bruker, Ettlingen, Germany), equipped with LN_2 cooled narrow-band MCT detector. A gas cell, modified to allow UV illumination and simultaneous FTIR spectroscopy, was employed (Figure 5.1).

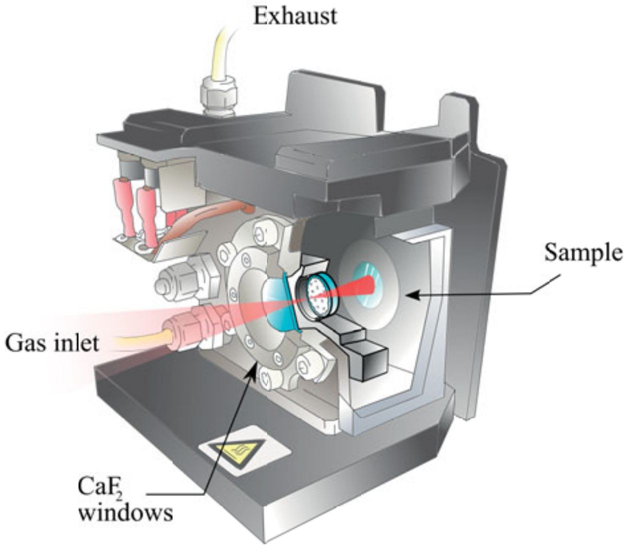

Figure 5.1: Transmission FTIR gas cell used in the measurements. The TiO_2 film is coated onto an IR and UV transparent CaF_2 substrate.

The UV illumination source was a single UV LED (NS370L-5CLA with λ = 370 ± 6 nm, Roithner Lasertechnik GmbH, Vienna, Austria). The UV illumination intensity was 1.1 mW cm^{-2} at the sample surface and was measured with a thermopile detector (Ophir, North Andover, MA, USA).

The IR reaction cell was connected to a homemade gas flow system with a set of computer-controlled mass flow regulators (Figure 5.2). The gas flow was set at 100 ml min^{-1}. It was a mixture of synthetic air, with 20% O_2 and 80% N_2 with purities 99.999 % and 99.994 %, respectively, and acetaldehyde (90 ppm CH_3CHO in N_2) with 99.999 % purity. The acetaldehyde gas-phase concentration was set to 50 ppm in all experiments.

Prior to the measurements the samples were thermal treated inside the reaction cell at 200°C for 15 min, during purging with synthetic air. The adsorption and a photoreaction of CH_3CHO were studied as a function of time and reaction cycles.

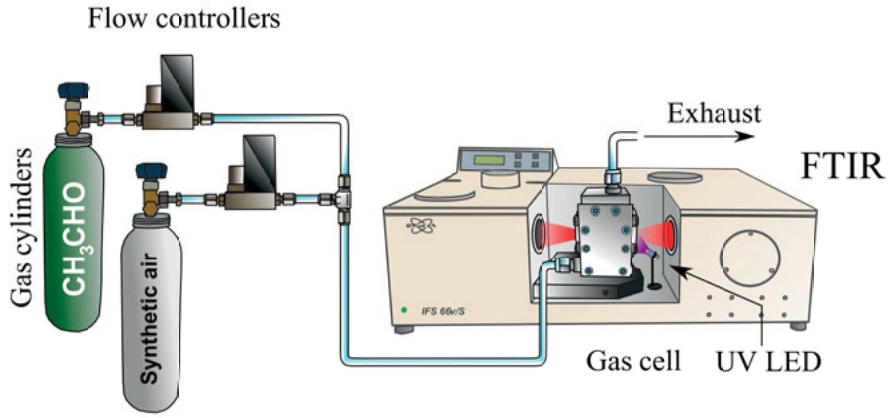

Figure 5.2: Experimental setup for the *in situ* FTIR CH_3CHO adsorption and photocatalysis measurements

Each reaction cycle consisted of dosing, purging and photocatalytic part as shown in Figure 5.3, followed by purging with synthetic air in-between cycles.

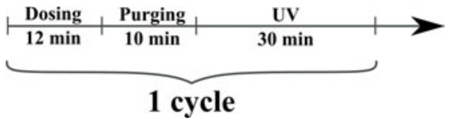

Figure 5.3: Experimental sequence for one photocatalytic cycle in the transmission FTIR experiments.

Four such experimental cycles were conducted on both the pristine and the $SO_4 - TiO_2$ films. FTIR spectra were obtained every 60 s. The wavelength interval was 1000 – 4000 cm^{-1} and each spectrum was calculated from an average of 138 scans. The spectral data were baseline corrected and smoothed with the Savitzky-Golay algorithm, using a nine-point window.

5.1.1. Preparation of FTIR data for micro – kinetic modelling

The background-corrected and smoothed FTIR spectra were binned in datasets, and imported into the R software environment for analysis. An example of the treatment procedure is briefly outlined in this section, using data for CH_3CHO adsorption and photo-oxidation on the pristine TiO_2 surface. The full data set is shown in Figure 5.4.

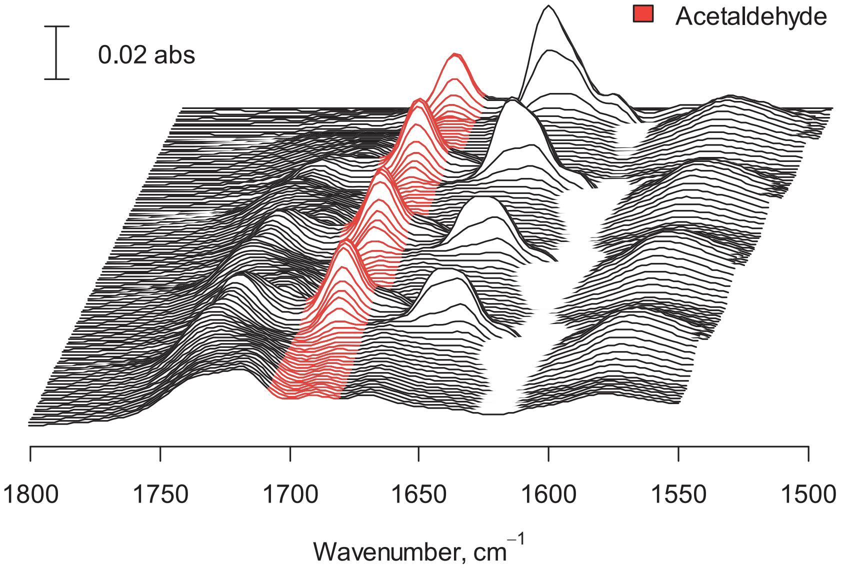

Figure 5.4: *In situ* FTIR data for CH_3CHO on the pristine TiO_2 surface. The data consists of 4 cycles of dosing, purging and UV illumination as outlined in section 5.1.

In order to extract intrinsic kinetic data, absorbance peaks corresponding to the coverage of major surface species were integrated. For example, the CH_3CHO peak, centered at 1693 cm^{-1}, was integrated in the 1680 – 1708 cm^{-1} range. Numerical integration was carried using Simpsons' rule. The resulting integrated FTIR absorbance versus time, for the CH_3CHO peak, is presented in Figure 5.5. It cannot be used for kinetic fitting directly, due to a number of reasons. First, it is not normalized according the IR absorption cross-sections of the corresponding surface species. The values of these cross-sections are available in databases, but only for gas-phase species, thus another treatment is needed in order to use the data quantitatively.

As the surface adsorption is limited by the numbers of adsorption sites, which in turn is determined by the saturation coverage, θ^{sat}, the data can be normalized by it. θ^{sat} is determined by fitting a Langmuir adsorption isotherm (eqn. 5.1) to the increase in the integrated CH_3CHO absorption peak, which occurs during dosing the surface with acetaldehyde. The resulting Langmuir fit is shown as a red line in Figure 5.5.

$$\theta_A = \theta_A^{sat}(1 - e^{-kt}) \qquad (5.1)$$

The obtained θ^{sat} is then used to normalize the spectroscopic data. This approach was followed only for CH_3CHO. The other surface species, treated by the micro-kinetic fitting, were normalized according to their maximum absorbance and the stoichiometry of their surface reactions in respect to CH_3CHO.

In the study of CH_3CHO adsorption and condensation no additional treatment is required. For the full kinetic modelling, however, another problem occurs during the UV illumination phase. It is shown in Figure 5.5 that after the first adsorption cycle there is a significant increase in the background, coinciding with the UV illumination of the sample.

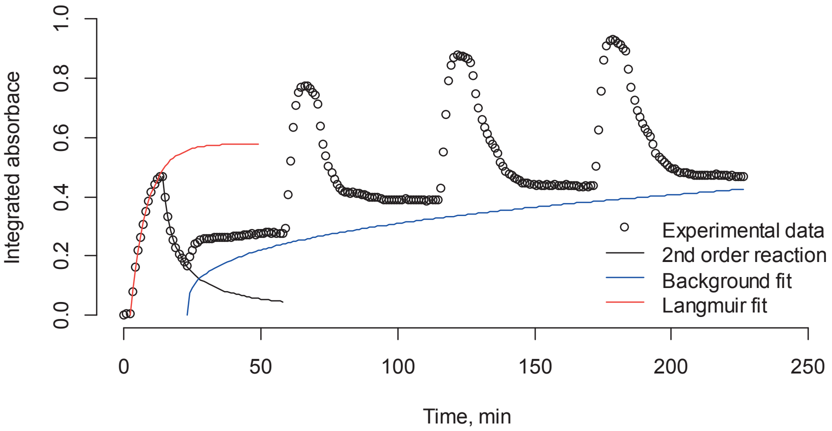

Figure 5.5: The integrated absorbance data for the CH_3CHO band illustrated with the treatment in order to prepare it for the kinetic fitting.

The reason for the background shift is that upon UV illumination of TiO_2 long-lived IR-absorbing states are excited below the conduction band of the semiconductor. They become populated during the UV illumination and contribute to the background shift throughout IR measurements. In order to correct for this shift the following procedure was developed: First, the background shift was estimated from the CH_3CHO data for the first purging period was used. During this period a decrease of the acetaldehyde coverage is observed, due to its condensation to crotonaldehyde. This condensation follows a simple second-order reaction scheme (eqn. 5.2).

$$2\,CH_3CHO \rightarrow CH_3(CH)_2CHO + H_2O \tag{5.2}$$

The analytical solution for the decrease in CH_3CHO coverage (eqn. 5.3) was then fitted to the experimental data.

$$\frac{1}{\theta_A} = \frac{1}{\theta_{A0}} + kt, \tag{5.3}$$

,where θ_A and θ_{A0} are the CH_3CHO coverage at time t, and the initial surface coverage, and k is the second-order rate constant. The resulting kinetic fit is then extrapolated throughout the entire purging and UV illumination part of the first experimental cycle (black line in Figure 5.5), and subtracted from the experimental data. The difference corresponds to the increase in background during the first cycle, and can be approximated with a simple power law equation (eqn. 5.4) in order to obtain a quantitative description.

$$I = at^b \tag{5.4}$$

I is the observed intensity change and a and b are constants. The fit is extrapolated throughout the entire experiment (blue line in Figure 5.5), and subtracted. The same background correction function was re-used for treating the integrated IR absorbance data on all species, with the a constant scaled accordingly to compensate for different integration ranges.

5.2. Liquid-phase photo-oxidation of Methylene blue dye

Liquid-phase photocatalytic measurements with Methylene Blue (MB) were carried in a batch reactor, which is shown schematically in Figure 5.6. It was developed as a part of the author's MSc thesis, and described in greater detail in the original publication [110].

The photo-oxidation reaction takes place in a glass reaction cell where a TiO_2 film, deposited onto a standard microscopy glass slide, is placed along with 100 mL of MB solution with a starting concentration of 1 ppm. The solution is magnetically stirred in order to minimize mass-transfer limitations. A 4W black-light UV tube (λ = 365 nm) served as a light source in all experiments.

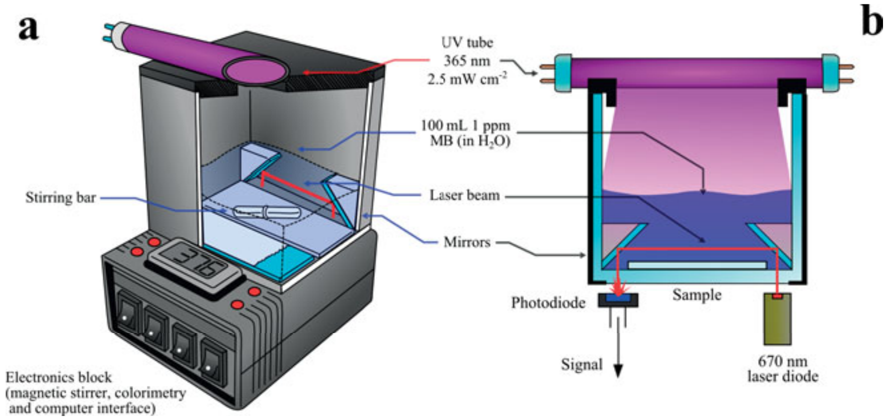

Figure 5.6: The photocatalytic reactor used to determined photo – oxidation rates of methylene blue in liquid-phase. Cut – out view (a) and schematic overview of the colorimetric system (b).

The MB concentration is followed *in situ* by measuring the absorbance of a laser beam (λ = 670 nm), which matches MB absorption peak. As a part of the PhD project an automated computer control unit and software were developed, and allowed for the execution of programmable experimental sequences.

5.2.1. Determination of photocatalytic rate constants in liquid-phase

In a typical experiment a TiO_2 film is placed in the reaction cell, initially containing 100 mL of deionized water. The baseline intensity of the laser beam (I_0) is measured and the MB concentration is adjusted to 1 ppm (using 100 ppm stock solution).

The first 40 min of the experiment were conducted in darkness, in order to achieve adsorption-desorption equilibrium between the MB dye and the TiO_2 film. The intensity of the laser beam (I) is measured every 2 min, until a stable value is obtained, indicating that saturation coverage (C_{sat}^{MB}) is reached. At this point the UV irradiation begins and the experiment continues for 80 min, during which I is measured every 10 min. The data of the laser intensity is converted into absorbance via eqn. 5.5.

$$A_{MB}(t) = -\log(\frac{I}{I_0}) \tag{5.5}$$

Since the initial MB concentration is known the absorbance data is converted easily into a concentration profile, as the one shown in Figure 5.7.

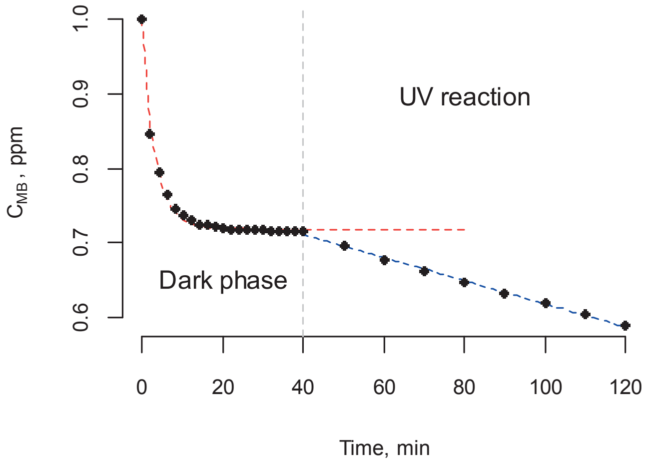

Figure 5.7: Overview of a photocatalytic experiment in liquid-phase. During the first 40 min an adsorption – desorption equilibrium is reached between the dye in the solution and the dye on the film surface. At t = 40 min the UV lamp is switched on and the concentration of MB decreases due to the photo-oxidation process.

C_{sat}^{MB} is obtained by fitting a Langmuir adsorption isotherm (eqn. 5.6) to the decrease in C_{MB} during the dark phase.

$$(1-\ C_{MB}) = C_{sat}^{MB}(1-e^{-k_{ad}t}), \tag{5.6}$$

where k_{ad} is the adsorption rate constant, and *t* is the time. As some of the MB is adsorbed on the reaction cell walls, this approach gives us a rough estimate of C_{sat}^{MB}. Nevertheless, any large differences in the films surface area, accessible for MB adsorption, would be reflected in the saturation coverage. For example, in a control experiment, without a TiO_2 film, a decrease of 0.1 ppm MB was observed, while a typical value for the sputtered samples was 0.3 ppm.

The photocatalytic rate constant, k_{MB}, is obtained from the decrease in C_{MB} up UV illumination. As the rate-determining step is the adsorption of MB on the TiO_2 surface, the process is often described via the Langmuir – Hinshelwood (LH) equation (eqn. 5.7).

$$-\frac{dC_{MB}}{dt} = \frac{k_{MB}KC_{MB}}{1+KC_{MB}}, \tag{5.7}$$

where dC_{MB}/dt is the rate of MB disappearance, k_{MB} – the apparent rate constant, and K – a factor determining the adsorption-desorption equilibrium. If C_{MB} is very small compared to the amount of photocatalyst, which is the typical case in photocatalytic experiments, the LH kinetics can be approximated to a pseudo-first order expression, viz.

$$-\frac{dC_{MB}}{dt} = k_{MB}C_{MB}\,. \tag{5.8}$$

The analytical solution of eqn. 5.8 is given by eqn. 5.9.

$$-ln\frac{C_{MB}}{C_{MB}^{0}} = k_{MB}t. \tag{5.9}$$

Thus, the plot of $-ln(C_{MB}/C_{MB}^{0})$ vs. time is a straight line, whose slope is determined by k_{MB}. C_{MB}^{0} is the initial concentration of MB dye in the beginning of UV irradiation (t = 40 min for the example in Figure 5.7).

5.3. Gas-phase photo-oxidation of acetaldehyde

The setup discussed in this section was constructed as a part of the PhD thesis work, and is a scaled-down version of the photocatalytic air cleaning window described in Chapter 3. An overview of the experimental setup is presented in Figure 5.8. It consists of three sections: (*i*) gas supply system (Figure 5.8a); (*ii*) photocatalytic reaction cell, and (*iii*) exhaust flow gas analyzing section (Figure 8.7b).

In the gas supply system, which is identical with the one described in Section 5.1, CH_3CHO (90 ppm in N_2) is mixed with synthetic air from an in-house supply, resulting in a 150 mL min^{-1} flow, containing 10 ppm CH_3CHO. The temperature of the resulting gas flow was kept close to 25°C and any fluctuations, caused by instabilities of the indoor synthetic gas supply, were minimized by a 300 mL ballast tank placed between the supply system and the experiment.

The relative humidity (RH) in the CH_3CHO flow was adjusted by feeding it through a gastight glass container with deionized water, which was kept at constant temperature in a water bath. Adjusting the temperature of the water bath in the range 10 – 25°C allowed for the RH to be controlled in the range 0 – 40%. Feedback was obtained by an in-stream capacitance humidity sensor (HIH-4000, Honeywell Inc., USA) positioned in the gas analyzing section.

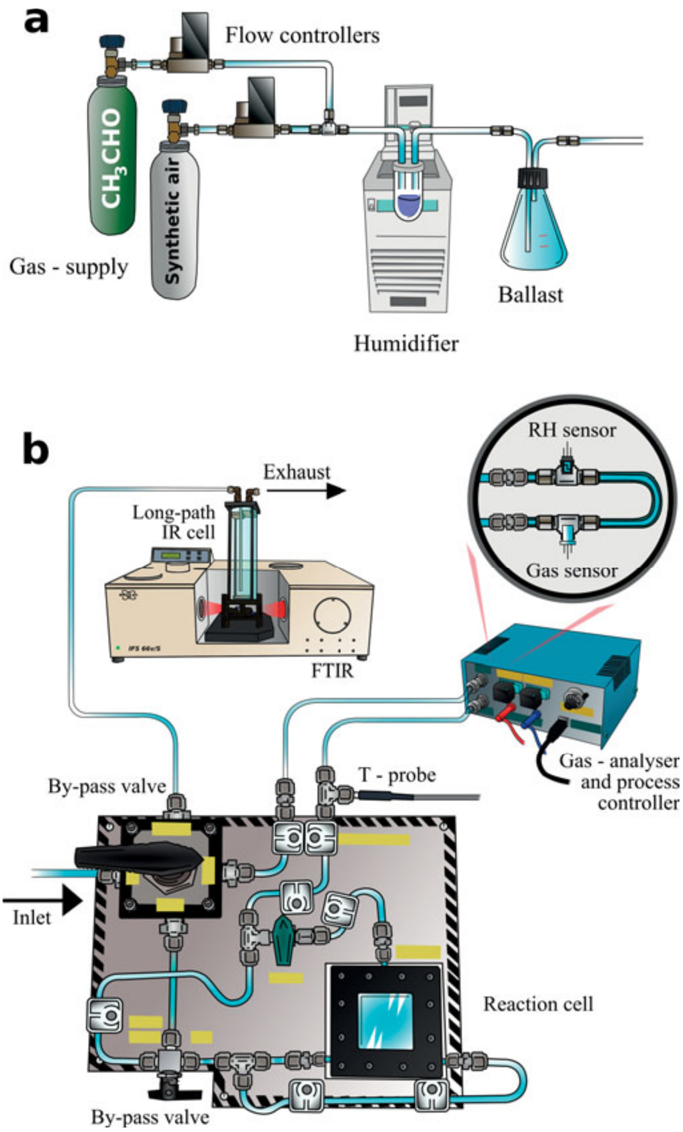

Figure 5.8: Overview of the gas-phase photocatalytic window setup used in gas-phase CH_3CHO experiments. The gas-supply system (a) and the reaction cell / gas analyser part (b).

The photocatalytic reaction cell, shown in Figure 5.9, consisted of a stainless steel frame equipped with two OptiWhite^{TM} glass windows (70 x 70 mm in size), which were spaced 5 mm apart and hermetically sealed with silicone O-rings. One of the OptiWhite^{TM} windows was coated with the sputter-deposited TiO_2 film, and facing the inside of the reaction cell with its coated side. The exposed coated area inside the cell was 50 × 50 mm, leading to a volume of 12.5 cm^3. Gas entered the cell via two inlets and left the through a single outlet.

As shown in Figure 5.9 the cell was sandwiched between the UV source (facing the film surface) and a heater (behind the coated window). The latter was used to adjust the surface temperature of the catalyst. Temperature feedback was given by a 1-wire digital thermometer IC (Dallas Semiconductor 18b20) positioned inside the heater.

The light source was an array of three high-intensity UV LEDs (P8D136, Seoul Semiconductors, Korea) with $\lambda = 365 \pm 5$ nm and 70 mW luminous flux. They were positioned in a triangular arrangement.

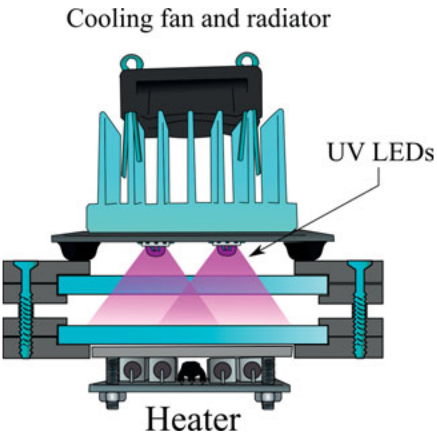

Figure 5.9: Cross-section view of the window reaction cell used in the setup, described in Figure 5.8 with the heater and UV illumination source

The concentration of CH_3CHO in the exhaust flow of the reaction cell was measured *in situ* by a dedicated homemade gas analyzing unit which was constructed by the author as a part of the PhD project. The gas analyzer has two sensors, both positioned in a U-shaped stainless steel tube through which the CH_3CHO flow passes, as shown in the inset of Figure 5.8b. The first sensor measures the humidity in the flow, as described above. The second sensor is a semiconductor gas sensor (HS-130AS, Sencera Co., Taiwan) and is employed to monitor the in-flow CH_3CHO concentration.

The gas analyzer also contains electronics responsible for process control, and a power supply for the gas sensor. An ADAM-4012 high precision digital-to-analogue conversion module (Advantech, Taiwan) converts the sensor signal and passes it to an Arduino microcontroller board, which is responsible for communication with a host PC for data logging. The latter is also responsible for setting the experimental sequence via control over the UV source and heater.

One example of an experimental sequence, which is used to study the effect of surface temperature (T^{surf}) on the CH_3CHO photo-oxidation rate is presented in Figure 5.10.

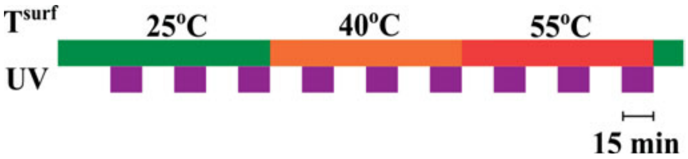

Figure 5.10: Experimental sequence used to obtain CH_3CHO photo-oxidation rates at different catalyst surface temperatures (T^{surf}). Each measurements comprised of three UV irradiation cycles of 15 min, separated by 15 min of darkness (to allow self-calibration of the baseline CH_3CHO signal)

The experiment, which is 4 h and 45 min in duration, consists of nine 15 min UV illumination cycles, binned into three groups, which are performed at increasing T^{surf} (25°C, 40°C and 55°C). All cycles are separated by 15 min dark periods, needed to allow for self-calibration of the baseline signal measured at 10 ppm CH_3CHO concentration in the flow. This procedure is repeated three times for each sample, at RH = 0%, 20% and 40%.

The presence of gas-phase intermediates was monitored by FTIR measurements in the exhaust flow. These were carried only when the experimental conditions allowed for it (at RH = 0%), employing a long-path FTIR gas cell (Model 8-PA, Infrared Analysis Inc., Anaheim, CA, USA).

5.3.1. Data treatment of the sensor signal

As described in the previous section, the concentration of CH_3CHO (C_{CH_3CHO}) was measured *in situ* by a semiconductor gas sensor. These operate on the basis of a relative change in the electrical resistivity of a polycrystalline sensing element, which is made of a metal oxide (e.g. SnO_2 or In_2O_3). When such metal oxides are subjected to atmosphere containing VOCs molecules from the gas-phase adsorb onto their surface. This leads to injection of electrons and the electrical properties of the sensing material are altered, proportionally to the concentration of the monitored gas [111; 112].

In our setup the gas sensor was connected in series with a shunt resistor. Changes in the resistivity of the sensing layer were reflected by changes in the voltage across the shunt resistor, V_{CH_3CHO}, which is directly proportional to C_{CH_3CHO}. In a series of calibration experiments the functional dependence $V_{CH_3CHO} = \sqrt{C_{CH_3CHO}}$ was obtained in the range $C_{CH_3CHO} = 0 - 60$ ppm. Raising the RH led to an increase of V_{CH_3CHO}, however, the above-mentioned functional dependence was preserved. The baseline signal of $V_{CH_3CHO}^{0\,ppm} = 70$ mV was found to be negligible, compared to $V_{CH_3CHO}^{10\,ppm} \cong 3$V and was omitted in calculations.

A typical plot of V_{CH_3CHO}, resulting from the experimental sequence shown in Figure 5.10, is presented in Figure 5.11a.

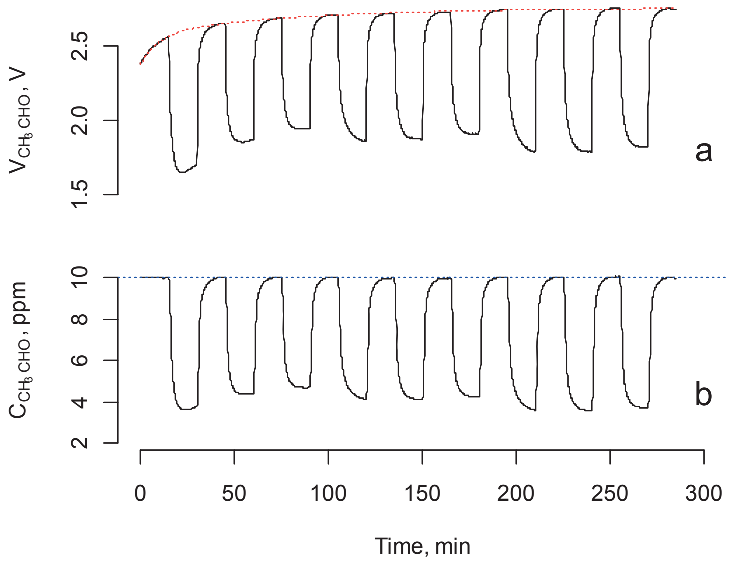

Figure 5.11: Example of experimental data on V_{CH_3CHO}, measured through the sequence, presented in Figure 5.10 (a) along with the sensor drift correction (red line) and the C_{CH_3CHO} obtained from the corrected data using eqn. 5.10 (b).

As visible, a slow, but noticeable drift in $V_{CH_3CHO}^{10\,ppm}$ of up to 15% was observed during the experiment. This is caused by processes taking place on the surface of the sensing layer, which alter the number of adsorption sites for CH_3CHO, and is noted in the manufacturer datasheet. Strategies to correct for this drift include conditioning the sensing element at higher temperatures, or aging it for 24 – 36 h in operando conditions. This was not possible in our experiments, so a correction for the drift was performed during the raw data treatment.

Since the experimental sequence was a series of 15 min long UV illumination cycles, separated by dark phases where $C_{CH_3CHO} = 10\,ppm$, a correction for the drift can be obtained by fitting a function throughout the dark periods. A Langmuir adsorption isotherm was successfully employed for this purpose, confirming that the drift is related to the changing number of surface adsorption sites. An example of such drift-correcting function is shown in Figure 5.11a, as a red line across the raw data. The drift-corrected V_{CH_3CHO} was converted into C_{CH_3CHO} using eqn. 5.10.

$$C_{CH_3CHO}[ppm] = \left(\frac{V_{CH_3CHO}{}^2}{V_{CH_3CHO}^{10\,ppm}{}^2}\right) 10[ppm] \qquad (5.10)$$

The rate of photocatalytic removal of CH_3CHO, r_{CH_3CHO}, was calculated from as-prepared C_{CH_3CHO} data. As shown in Figure 5.11b, during UV illumination cycles C_{CH_3CHO} drops significantly, as CH_3CHO is consumed in the photocatalytic reaction cell.

It is important to note, that since the experiments were conducted in flow mode, each UV illumination cycle starts with a very high CH_3CHO coverage on the catalyst surface. This is due to the fact that prior each cycle the film was constantly exposed to CH_3CHO. As a consequence of that it takes some time for the equilibrium CH_3CHO coverage to be reached, since it is determined by the ratio of the rates of CH_3CHO adsorption and removal. The response time of the sensor, which is of the order of few minutes, contributes to uncertainty in C_{CH_3CHO} during the first minutes as well.

Hence, the steady-state r_{CH_3CHO} was calculated from C_{CH_3CHO} measured in the end of the respective illumination cycle. It was normalized to the catalyst surface area, according to eqn. 5.11.

$$r_{\mathrm{CH_3CHO}}[\mu\,\mathrm{mol\,min^{-1}cm^{-2}}] = \frac{(10\,[\mathrm{ppm}] - C_{\mathrm{CH_3CHO}}\,[\mathrm{ppm}])}{10\,[\mathrm{ppm}]S[cm^2]}\,F\,[\mu\,\mathrm{mol\,min^{-1}}], \qquad (5.11)$$

where S is the exposed area coated with photocatalytic TiO_2 film (25 cm^2), and F is the CH_3CHO mass-flow rate through the reaction cell. The latter was 0.061 μmol min^{-1} and 0.041 μmol^{-1} for the case of 10 ppm CH_3CHO, supplied at flow rates of 150 mL min^{-1} and 100 mL min^{-1}, respectively.

5.3.2. Presence of gas-phase intermediates

The semiconductor VOC gas sensor does not discriminate between different species in the gas-phase. Thus, it was important to confirm if any intermediates were present in the exhaust flow, as these might affect the measured C_{CH_3CHO} values.

This was achieved by passing the exhaust flow through a long-path FTIR gas cell. FTIR spectra were obtained prior to, and during UV illumination. Two FTIR spectra of this kind are presented in Figure 5.12.

Even at RH = 0% the exhaust flow contained trace amounts of water, which is a product of the photocatalytic oxidation reactions. Thus, an atmospheric correction was performed on the spectra, in order to remove the distortion caused by water δ(HOH) bands, which would otherwise overlap with the carbonyl frequency region in the CH_3CHO IR spectra.

As shown in Figure 5.12, the exhaust flow contains nothing but CH_3CHO and gas-phase CO_2, which is another product of the photo-oxidation reaction. This implies that CH_3CHO is completely mineralized by the TiO_2 films during UV illumination. If present, gas-phase intermediates are expected to be at sub – ppb level, which is the sensitivity limit of the FTIR gas cell.

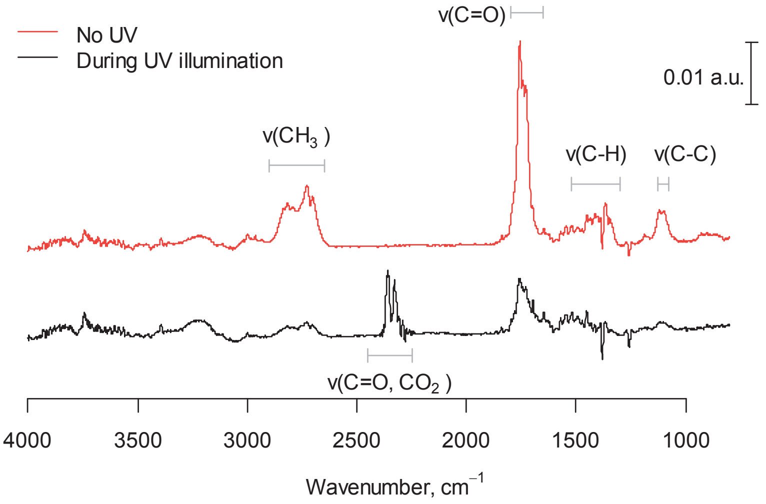

Figure 5.12: FTIR spectra of gas-phase CH_3CHO before and during UV illumination. The spectra during UV illumination was obtained at the end of a 15 – min – long UV illumination cycle, which allowed sufficient time that the FTIR gas cell is saturated with reaction products. The characteristic vibration modes of CH_3CHO and CO_2 are shown.

At such low concentrations, if present, the gas-phase intermediates are not expected to affect the signal from the semiconductor gas sensor. The gas sensor is not sensitive to CO_2 as well, particularly at the concentrations expected in the exhaust gas flow, of up to 20 ppm, assuming a full mineralization of the 10 ppm CH_3CHO inlet gas flow.

5.4. Modelling of spatial light intensity distributions

An important aspect in photocatalytic experiments is the UV illumination intensity distribution over the catalyst surface. As discussed in the overview of photocatalysis basics in Chapter 2, in photocatalysis the energy needed to overcome the reaction barrier is provided by light. Some authors go as far as suggesting that the term “photocatalysis” itself is not semantically correct, since light does not actually catalyze the reaction, but can be considered a reagent, which is consumed during its course [23]. Thus, knowing how much light reaches the catalyst can be as important, as knowing the concentration of the substrate molecule or the amount of catalyst.

Often the illumination intensity cannot be measured directly at the catalyst surface, and in this case spatial light-distribution models can be employed. In this section we will discuss two models, which are relevant for the light sources used in the experimental setups described in Sections 5.2 and 5.3.

5.4.1. The linear source spherical emission model for UV tube sources

An UV tube is used as a light source in liquid-phase experiments (Section 5.2). The tube can be approximated as a line source, where every point, laying across its length, emits light isotopically. This is the basis of the linear source spherical emission (LSSE) model (eqn. 5.12) [113; 114]. It can be employed to give an accurate description of the spatial illumination distribution on any flat surface positioned at a given distance from the tube.

$$I(x,y) = \frac{2\pi r_L I_W}{8\pi R}\left[atan\left(\frac{x}{R}\right) - atan\left(\frac{x-L}{R}\right)\right], \qquad (5.12)$$

Here r_L is the lamp radius, I_W is the intensity measured at the wall of the UV tube, x and y are spatial coordinates, L is the length of the lamp, and R is the shortest distance between the lamp axis and the point of interest in the y direction (calculated via eqn. 5.13).

$$R = \sqrt{Z^2 + y^2}, \qquad (5.13)$$

where Z and y are the distance between the lamp axis and the surface of interest, and the spatial coordinate in the y direction, respectively. The parameters are schematically noted in Figure 5.13.

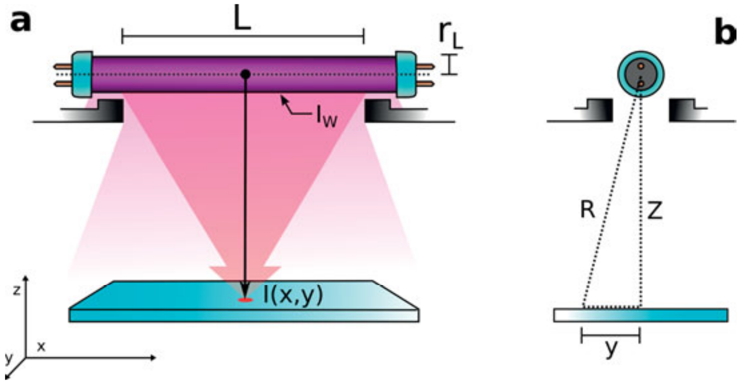

Figure 5.13: Schematic representation of the LSSE light-distribution model and the parameters used in eqns. 5.13 and 5.14. 2D isometric view (a) and side-view (b). Red arrow signifies that the contribution of every point across the optical axis of the tube is taken into account in calculating *I(x, y)*.

For the 4W UV tube used in the liquid-phase MB reactor described in Section 5.2: r_L is 15 mm, L is 65 mm (determined by the opening at the lid of the liquid-phase reaction cell, where the UV tube is positioned), I_W is 2.44 mW cm^{-2}, and the UV tube – to – sample distance is a minimum of 85 mm and determined by the reaction cell height. In some experiments, where the intensity dependence of the reaction rate was studied, the intensity was changed by shifting the UV tube upwards from the reaction cell.

The LSSE model allows for an easy calculation of the resulting spatial distribution. Figure 5.14 shows two such distributions, which were determined for the minimum UV tube – to – sample distance (85 mm) and for the case where the UV tube was shifted with 50 mm upwards in the Z direction (Z = 135 mm).

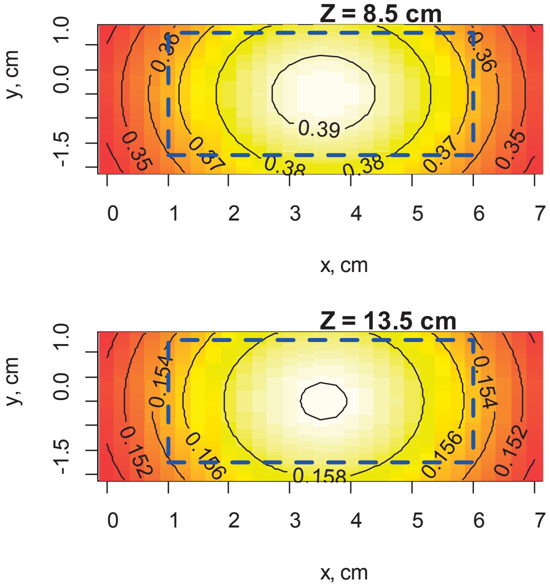

Figure 5.14: Intensity distributions, obtained over a TiO_2 film in the liquid-phase MB reactor (Section 5.2), for lamp positioned at 85 mm, and 135 mm above the film. The values of the isointensity lines are in mW cm^{-2}.

The position and dimensions of the TiO_2 film are marked with a dashed blue line. The average UV illumination intensity obtained at the catalyst surface is 0.38 mW cm^{-2} and 0.16 mW cm^{-2} for Z = 85 mm and Z = 135 mm, respectively.

5.4.2. Modified cosine law model for LEDs and LED arrays

In the gas-phase photocatalytic setup, described in Section 5.3, an array of three UV LEDs was used as a light source. In a crude approximation, the LED can be considered a point source, and the angular dependence of its relative intensity can be described with a cosine law: $I(\theta) = I(0)\cos(\theta)$.

In reality this approximation does not yield a good result, since the LEDs usually have a number of optical components, such as an integrated reflector and a plastic dome, that serves as a lens, which are employed to shape and direct the light. Fortunately, there are semi-empirical models designed to accurately describe angular and spatial light distributions for a specific LED. One example is the model proposed by Moreno *et al* [115].

Here the angular distribution of the light intensity is approximated to a sum of i cosine functions (usually three), each of them with three adjustable parameters (a_i, b_i and c_i).

$$I(\theta) = \sum_{i=1}^{3} \mathrm{a}_i \cos(\theta - b_i)^{c_i} \tag{5.14}$$

These parameters are obtained by fitting the sum to an experimentally determined angular distribution, which is usually found in the manufacturer datasheet for a specific LED. Figure 5.15 shows the angular distribution of the P8D136 LED and the resulting fit from eqn. 5.14.

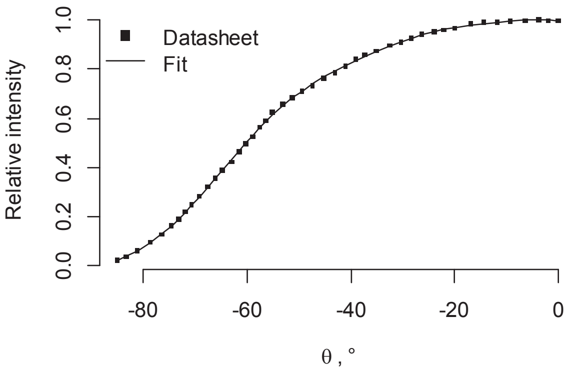

Figure 5.15: Angular distribution of relative UV light intensity for the P8D136 LED used in the setup described in Section 5.3, and the resulting fit from Moreno's model (eqn. 5.14).

Once the fitting parameters in eqn. 5.14 are obtained, allowing for a correct description of the angular dependence, the incident light intensity at any point with coordinates (x, y, z), relative to the optical center of the LED, can be calculated via eqn. 5.15.

$$I(x,y,z) = \frac{I_0}{z^2} I(\arctan(\frac{\sqrt{x^2+y^2}}{z})) \tag{5.15}$$

The absolute intensity *I(x, y, z)* is calculated taking into account both the angular dependence of the relative intensity, which is specific for the LED (via eqn. 5.14), and the inverse-square law, which is typical for any point source of light, on the total luminous flux (I_0) of the LED (refer to Figure 5.16a for clarification).

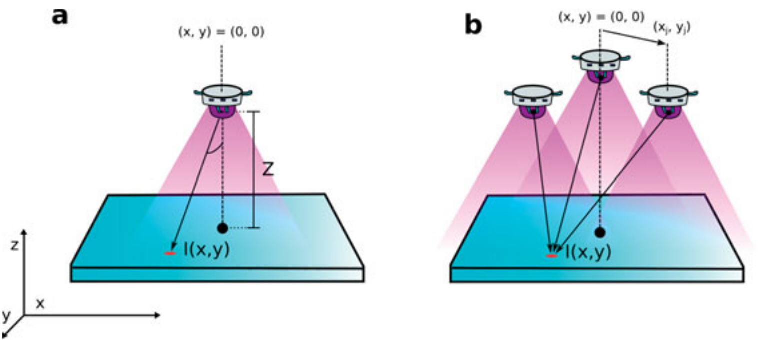

Figure 5.16: Geometric considerations in order to calculate I(x, y) for a single LED (a) and for an array of three LEDs (b), such is the case in the setup presented in Section 5.3.

For the case of an array of j LEDS, each LED is displaced from the center of the coordinate system by its geometric position in the array (x_j, y_j). Then the spatial distribution of the array is calculated, by summing up the contributions of each LED at point *I(x, y, z)* via eqn. 5.16, as shown in Figure 5.16b.

$$I^{tot}(x,y,z) = \sum_{j=1}^{3} I(x+x_j, y+y_j, z) \tag{5.16}$$

Figure 5.17 shows the ensuing spatial distribution of the three-LED-array from Section 5.3. The blue circles represent the positions of each LED. The average UV illumination intensity was found to be about 13 mW cm^{-1}, with local values ranging from 10 to 20 mW cm^{-1}.

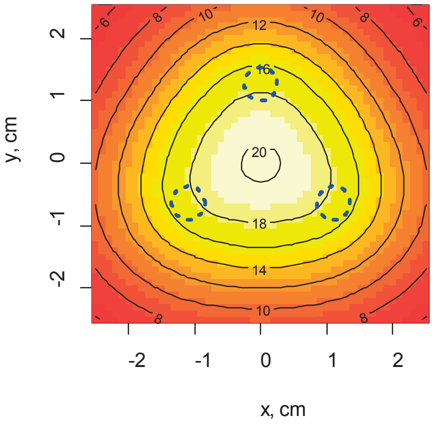

Figure 5.17: Spatial UV intensity distribution for the array used in the gas-phase setup (Section 5.3). The positions of the three LEDs is noted with blue dashed circles. The values of the isointensity lines are in mW cm^{-2}.

6. DFT calculations

Density functional theory (DFT) calculations were performed in order to predict the vibrational frequencies of unknown surface adsorbates, and help elucidate the mechanism of CH_3CHO adsorption and photo-oxidation by TiO_2. This chapter outlines the basic theoretical backgrounds of DFT and describes the procedure used to obtain the calculated results.

6.1. Density Functional Theory Calculations

The Density Functional Theory (DFT) is a quantum-mechanical theory for solving the ground-state electronic structure of many-body systems. It provides the means for solving the Schrödinger equation of such systems. As known from basic quantum mechanics, the time-independent Schrödinger equation (eqn. 6.1) postulates that the ground-energy E of any system is related to its wave function Ψ through the Hamiltonian operator $\hat{H}$.

$$\hat{H}E = \hat{H}\Psi \tag{6.1}$$

$\hat{H}$ itself can be split into three contributions to E (eqn. 6.2): The kinetic energy, which is given by the kinetic energy operator $\hat{T}$, the potential energy of the electron – nuclei interaction ($\hat{V}_{Ne}$), and the potential energy of the electron – electron interaction ($\hat{V}_{ee}$).

$$\hat{H} = \hat{T} + \hat{V}_{Ne} + \hat{V}_{ee} = -\frac{1}{2}\sum_i \nabla_i^2 - \sum_i \sum_A \frac{Z_A}{r_{iA}} - \sum_i \sum_j \frac{1}{r_{ij}} \tag{6.2}$$

Since the nuclei have much higher mass compared to that of the electrons, which results in a much smaller momentum, their positions can be fixed according to the Born-Oppenheimer approximation. Thus, the electrons move in a static external potential V_{ext}, defined by the positions and charge of the immobilized nuclei. This simplifies the first two members of the Hamiltonian, $\hat{T}$ and $\hat{V}_{Ne}$, to a sum of single-particle equations. The electron-electron interaction operator $\hat{V}_{ee}$, however, cannot be described with single particle equations and another approximation is required for solving it.

A well-known way to solve this problem is the Hartree-Fock method. First, the ground state wave function is represented as a Slater determinant (eqn. 6.3). It is constructed as a matrix of many single-electron functions, known as spin orbitals.

$$\Psi_{HF} = \frac{1}{\sqrt{N!}}\begin{bmatrix} \psi_1(\vec{x}_1) & \cdots & \psi_N(\vec{x}_1) \\ \vdots & \ddots & \vdots \\ \psi_1(\vec{x}_{1N}) & \cdots & \psi_N(\vec{x}_N) \end{bmatrix} \qquad (6.3)$$

Then, the complex many-body Hamiltonian is replaced by the one-electron Fock operator $\hat{f}$ (6.4), which describes the kinetic and potential energy of every one-electron-core interaction. The repulsion term is defined as the Hartree-Fock potential V_{HF}.

$$\hat{f}(i) = -\frac{1}{2}\nabla_i^2 - \sum_i^A \frac{Z_A}{r_{iA}} + V_{HF}(i) \qquad (6.4)$$

The Hartree-Fock potential (eqn. 6.5) is calculated for one electron at a time, but information for all of the spin-orbitals is required in order to solve it.

$$V_{HF}(\hat{x}_1) = \sum_j (\hat{J}_j(\vec{x}_1) - \hat{K}_j(\vec{x}_1)) \qquad (6.5)$$

The Coulomb operator $\hat{J}$ (eqn. 6.6) is responsible for the interaction between the *i*–th electron and the average charge distribution of an electron, occupying the spin-orbital state ψ_j.

$$\hat{J}_j(\vec{x}_1) = \int \left|\psi_j(\vec{x}_2)\right|^2 \frac{1}{r_{12}} d\vec{x}_2 \qquad (6.6)$$

The exchange operator $\hat{K}$ (eqn. 6.7) is based on a purely mathematical formalism, and has no physical meaning. It is similar to the Coulomb operator, but the two electrons exchange their positions in the integral, which is due to the Pauli exclusion principle, which forbids two electrons with the same spin to occupy the same space.

$$\hat{K}_j(\vec{x}_1)\psi_i(\vec{x}_1) = \int \psi_j^*(\vec{x}_2)\frac{1}{r_{12}}\psi_i(\vec{x}_2)d\vec{x}_2\psi_j(\vec{x}_1) \qquad (6.7)$$

The exchange energy described by $\hat{K}$ is part of the electron correlation energy, which is not entirely taken into account in the HF theory. The electron correlation energy (E_{XC}) takes into account all effects of the electron – electron interaction, and requires the electrons to be treated explicitly.

The Hamiltonian of the system then is expressed as a Fock matrix of one-electron Fock operators. Applying it on the Slater determinant, the Hartree-Fock energy E_{HF} can be obtained through the self-consistent field (SCF) operation. Basically the Slater determinant and the Fock matrix are diagonalized iteratively, and their eigenvalues are exchanged after each cycle, as starting values for the next one until the change in the electron density fall below certain threshold. Then E_{HF} is obtained, and along it the properties of the system.

The main problem with the HF methods is that for a system of N particles the wave function depends on 4N variables, and the number of inter-particle interactions increases exponentially with system size. DFT simplifies this many-body problem to a one-body problem, by actually making the electron density $\rho(\vec{r})$, which is a by-product in HF, into a main observable variable. $\rho(\vec{r})$ is the probability to find an electron in a given point and is a real-world quantity, depending on 3 spatial coordinates.

The DFT is based on two assumptions, which are called the Hohenberg-Kohn (HK) theorems. The first HK theorem states that the ground-state properties of any system of N particles are determined by $\rho(\vec{r})$, and hence all interactions within the system can be expressed as functionals the electron density. The second HK tells us how to find this ground-state $\rho(\vec{r})$. It states that the density, corresponding to the lowest possible energy for a given V_{ext} (eqn. 6.8) is the ground state density of the system. In DFT the density is obtained by introducing a fictional system of non-interacting electrons. They populate a set of one-electron wavefunctions called Kohn-Sham (KS) orbitals, $\psi(\vec{r},\sigma)$, similarly to the one-electron wavefunction approach in HF. The KS orbitals have no physical meaning, but can be used in order to calculate the density of the system.

$$\rho(\vec{r}) = \sum_i \sum_\sigma |\psi_i(\vec{r},\sigma)|^2 \qquad (6.8)$$

The energy of the system then is expressed as:

$$E_0 = (F[\rho] + \int \rho(\vec{r}) V_{Ne} d\vec{r}) \qquad (6.9)$$

where $F[\rho]$ is the universal functional. The main problem is that the exact form of $F[\rho]$is unknown. It contains functionals for the kinetic energy $T[\rho]$, the classical Coulomb interaction $J[\rho]$, and the non-classical portion of the interaction $E_{ncl}[\rho]$ (eqn. 6.10). From them only the Coulomb interaction is easy to find.

$$F[\rho] = T[\rho] + J[\rho] + E_{ncl}[\rho] \qquad (6.10)$$

Using the non-interacting system the kinetic energy can also be found (eqn. 6.11).

$$T = -\frac{1}{2} \sum_i \langle \psi_i | \nabla^2 | \psi_i \rangle \qquad (6.11)$$

This approach was proposed by Kohn and Sham and an analytical solution for the energy of the system was also proposed (the so called Kohn-Sham equation). However it does not include the exchange-correlation energy E_{XC}, which is one of the big deficiencies of the DFT method. Since the electrons are not explicitly included in the calculation, as in HF, the exchange energy cannot be easily found. At the price of some approximations it can be expressed through the electron density through the methods of Local Density Approximation (LDA) or Generalized Gradient Approximation (GGA). Both of them work similarly, by treating $\rho(\vec{r})$ as probability to find an electron at a given volume around the nucleus. In LDA the absolute density is used, while in GGA its gradient is also taken into account. Then the exchange and correlation energies are derived from this data. This, however, leads to significant errors and can affect certain types of calculations, where the electron correlation is important for the result. Such are the calculations on non-covalent interactions or when the thermochemistry of a system must be evaluated thoroughly. For such calculations the so-called hybrid functionals must be used. In them the E_{XC} is partly expressed in terms of the KS orbitals, by calculating the exact exchange through HF. An example of such functional is the B3LYP, which is parameterized for general calculations, but still does not provide good results for many non-covalent interactions. For such the Minnesota family of functionals is a good choice, an example being the M06 by Truhlar group. It is a meta-GGA hybrid functional, which uses the Laplacian of the electron density, as well as 27% of exact HF exchange. It is also parameterized for good results, when it comes to non-covalent bonding, system with transition metals and organometallics.

6.2. Basis sets

As we discussed in the previous topic the Slater determinant is constructed by a number of single-electron wavefunctions, known as spin-orbitals. They are the product of two functions – the spatial orbital function $\phi_i(\vec{r})$ and the spin function $\sigma(s)$ (eqn. 6.12).

$$\psi_i(\vec{x}) = \phi_i(\vec{r})\sigma(s) \tag{6.12}$$

While the latter can be fully described only with only two functions ($\alpha(s)$ and $\beta(s)$) due to the fermionic nature of the electron, the spatial part can be described with any spatial function. Such function is the Slater type orbital (STO). It is based on the solutions for the hydrogen and describes the behavior of the electron around the nucleus very precisely. However it is very difficult to use it for computations on molecules, because the integrals cannot easily be adapter for multi-center calculations.

Fortunately the STO function can also be represented as a linear combination of other functions mimicking its behavior. Nowadays most of the software use linear combinations of contracted Gaussian functions. They come along initial coefficients optimized for every element in sets of functions, called basis sets. An example for minimal basis set is the STO-3G, where the STO are approximated to a three contracted Gaussian functions.

In practice, the split-valence basis sets, as the X-YZg are more widely used and return much better results. An example of such is the 6-31g, where the core-electrons are described with 6 contracted Gaussian functions, while the valence shell is split into two parts, described respectively with 3 Gaussians for the inner and 1 Gaussian for the outer electrons (allowing them to be very flexible and participate in chemical bonds). Such split valence sets are also known as Pople sets, named after its creator. The valence shell can be split even more, introducing even higher flexibility (for example 6-311g, where it is split into three parts, described with 3, 1 and 1 Gaussians).

The larger the basis set is, the better description of the system is expected and the predicted energy will be more precise. But of course this comes at higher computational costs, because more and more functions are introduced. One of the ways to ease the calculations is the use of Effective core potential (ECP) basis sets. In them the core electrons are no longer calculated implicitly and are replaced with an effective potential, representing their density. Such ECP sets are particularly useful for heavier elements that have a lot of core electrons. Example of ECP basis set is the LANL2DZ basis set.

6.3. Modeling of the TiO_2 surface

As shown by the XRD (Section 4.2) and TEM (Section 4.3.1) analysis, the commercial DyeSol anatase nanoparticles are dominated by {101} surfaces. Thus, for the DFT calculations a small cluster model was constructed, based on a model of the {101} facet (Figure 6.1).

The decision to employ a cluster model, instead of a periodic slab, was motivated by the a priori knowledge that the adsorption on oxide surfaces is a localized process. Furthermore, the overall aim of these DFT calculations was to supplement the *in situ* FTIR data and provide a rational explanation for observed absorption bands of unknown species. One example is a hitherto unknown dimeric CH_3CHO adsorbate, which is a central topic in Paper I. In that case, the main interest is not how the adsorbates would influence the surface itself, but how the surface influences the electronic structure of the adsorbates, and what effect will that interaction have on their IR vibrational frequencies. Hence, the use of a simpler model for the surface is justified in order to capture the main trends, which the surface interactions have on the adsorbates. Furthermore this allows for a description of the adsorbates employing a higher level of theory (the plane-wave basis sets used in periodic calculations rarely describe organics well), and for a number of corrections to the energy to be carried, which would otherwise be difficult to obtain from periodic calculations.

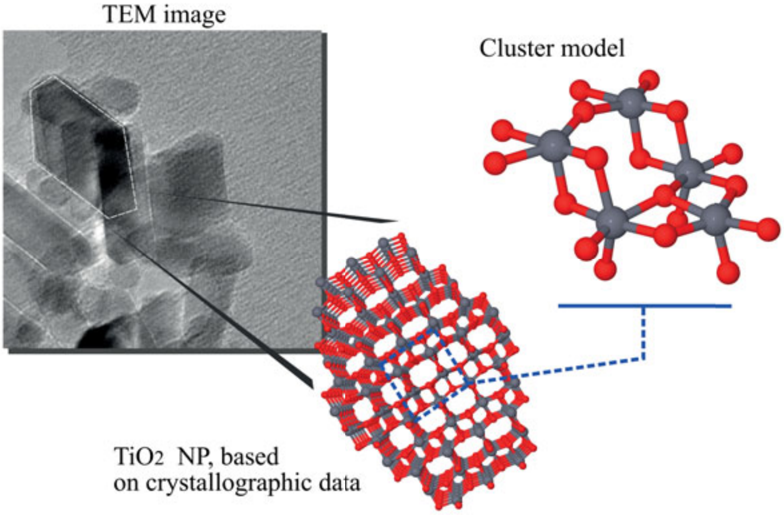

Figure 6.1: The dominant (101) plane was selected to prepare a model of TiO_2 surface for the DFT calculations. A cluster representation of the surface was chosen in order to spare computational resources.

The cluster is based on crystallographic data for the anatase unit cell at 25 °C [95]. It contains 5 Ti atoms and the dangling bonds were saturated by hydrogens, leading to the formula $Ti_5O_{10} \times 8H_2O$ (Figure 6.2).

All calculations were performed on a partially relaxed cluster. Both the peripheral oxygen atoms and the saturation hydrogen atoms were fixed, in order to provide stability for the structure. During the relaxation procedure the spacing in the [010] direction increased from 3.78 Å to 3.80 Å.

The equilibrium geometry of the adsorbate-cluster system was calculated in several steps. First, a rough optimization was performed with the Huzinaga MIDI minimal basis set [116]. The resulting geometry was then re-optimized, at a higher level, by a combination of basis set functions: The LANL2DZ ECP basis [117] was employed for the Ti atoms in the cluster. It was obtained from the Basis Set Exchange (BSE) database [118]. The standard Pople split-valence 6-31G* basis set was used for oxygen and hydrogen atoms within the cluster. Finally, the 6-31++G** basis set was used to describe the organic adsorbate molecule [119; 120; 121].

The adsorption itself was carried by positioning the optimized adsorbate geometry over the relaxed cluster, with the C=O group oriented toward the 5-fold coordinated Ti^{4+} atom. The distance between the adsorbate and the cluster was ~ 5 Å. The energy was then minimized: first with the lower basis sets (MIDI), and then by re-optimization at the higher level of theory (LANL2DZ/6-31G/6-31++G**).

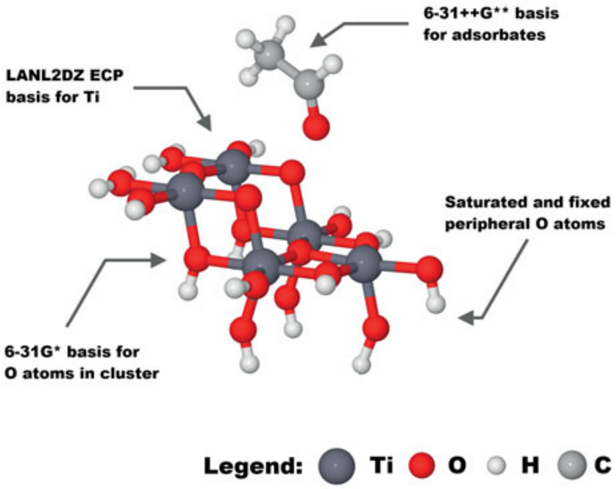

Figure 6.2: Structure of the $Ti_5O_{10}x8H_2O$ cluster model used to represent the anatase (101) surface in the DFT calculation, and the acetaldehyde molecule prior to geometry optimization. The basis sets used for geometry optimization of the structure at different levels are indicated.

Among the data obtained from DFT calculations were: the total electronic energy, the zero-point energy correction to the electronic energy (ZPE), the Gibbs free energy correction to the total electronic energy (G), the entropy correction to the total electronic energy (S), and the IR vibrational frequencies. All electronic energies were counterpoise (CP) corrected using the Boys and Bernardi scheme (eqn. 6.13) [122].

$$\Delta E = E(Ads@Cluster) - E(Cluster) - E(Ads) \tag{6.13}$$

ΔE is the energy change due to the adsorption, and E is the CP and ZPE corrected total electronic energy for the respective parts of the system. The adsorption enthalpy ΔH, and free energy change ΔG were computed in a similar way, but instead of using a ZPE correction, the total electronic energy of each of the interacting species were adjusted with thermal correction to standard conditions (298.15 K, 1 atm), and with the Gibbs free energy correction, as calculated by GAMESS (including the ZPE).

The IR vibrational frequencies were computed at the high computational level by means of the default two-point method in GAMESS. All IR frequencies were corrected with a scaling factor of 0.947, as recommended by the National Institute of Standards and Technology (NIST) [123]. Derivatives of the vibrational spectra, such as ZPE, entropy, thermal and free energy corrections were also scaled with the same factor. In order to be compared with experimental data, the calculated IR frequencies were convoluted with Lorentzian functions using a home-made R script.

7. Results on the photocatalytic activity of TiO_2

This chapter covers the experimental results concerning the photocatalytic activity of anatase TiO_2, which is discussed in the appended papers. The experimental and theoretical methods used to obtain or treat the data were presented in the preceding chapters.

7.1. Mechanism of acetaldehyde adsorption and photo-oxidation on pristine and SO_4 – modified anatase TiO_2 films (Papers I, II)

In the first part of this section the mechanisms of adsorption of acetaldehyde (CH_3CHO), and its spontaneous condensation to crotonaldehyde on the TiO_2 surface is investigated by *in situ* FTIR and DFT calculations.

The experiments employed films of commercial TiO_2 catalyst prepared by Doctor-blading (Section 4.1.1). *In situ* FTIR spectroscopy was used to in order to study adsorption kinetics on the TiO_2 surface during its exposure to 50 ppm of CH_3CHO in synthetic air (Section 5.1). In the experiments TiO_2 was first exposed to acetaldehyde, until saturation of the surface was reached (12 min). The reaction cell was subsequently purged with synthetic air for 10 min.

In the second part, the detailed reaction mechanism of acetaldehyde photo-oxidation is investigated by *in situ* FTIR data, obtained during subsequent 30 min of UV irradiation. Comparison is made between reaction pathways on the pristine and the SO_4 – modified TiO_2 surfaces. The effects of multiple reaction cycles are taken into account as well.

7.1.1. Adsorption of acetaldehyde on the anatase TiO_2 surface.

7.1.1.1. Overview of FTIR spectroscopy and kinetic data

The FTIR spectra of the Doctor-bladed TiO_2 films exposed to acetaldehyde were characterized by the appearance of an intense peak at 1693 cm^{-1}, which was associated with the $\upsilon(C{=}O)$ vibration of mono-dentate CH_3CHO, coordinated to Ti^{4+} centers with its carbonyl oxygen [124]. Meanwhile, another carbonyl peak appeared at 1653 cm^{-1}. Initially this band was less intense, compared to the 1693 cm^{-1} CH_3CHO carbonyl peak, but with the increasing CH_3CHO coverage the relative difference between these two peaks decreased. After the saturation coverage was reached, and during purging with synthetic air, the peak at 1693 cm^{-1} decreased and eventually vanished. Contrary, the 1653 cm^{-1} peak increased in a concerted manner (Figure 6.1a).

The 1653 cm^{-1} peak was associated with the formation of crotonaldehyde ($CH_3(CH)_2CHO$), due to an aldol condensation between acetaldehyde molecules on the TiO_2 surface (eqn. 7.1).

$$2CH_3CHO^{gas} \xrightarrow{k_A^{ad}} 2CH_3CHO \xrightarrow{k_A} CH_3(CH)_2CHO + H_2O \qquad (7.1)$$

It is known that such condensation reactions occur spontaneously at room temperature not only on the TiO_2 surface[125], but on other metal oxide surfaces as well [126; 127].

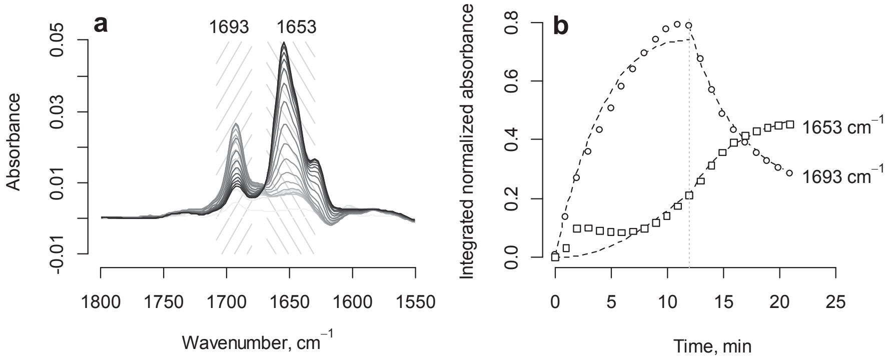

Figure 7.1: (a) Progression of carbonyl peaks for acetaldehyde (1693 cm^{-1}) and crotonaldehyde (1653 cm^{-1}) during exposure of TiO_2 to acetaldehyde; the widths chosen for integration of peak areas are indicated by differently hashed rectangular areas. (b) Time-traces of the integrated carbonyl bands for acetaldehyde and crotonaldehyde as a function of time (gas dosing at $0 < t < 12$ minutes; purging in synthetic air at $13 < t < 23$ minutes); dashed curves show results from kinetic modelling. In the simplest model it fails to take into account for the contribution of the intermediate species which appear between $0 < t < 5$ minutes (see text).

The integrated and normalized absorbance data for the acetaldehyde → crotonaldehyde conversion was fitted with the following set of kinetic equations:

$$\frac{d\theta_A}{dt} = k_A^{ad}(\theta^{sat} - \theta_A - \theta_C) - k_A^{cond}\theta_A^2 \qquad (7.2)$$

$$\frac{d\theta_C}{dt} = \frac{1}{2}k_A^{cond}\theta_A^2 \qquad (7.3)$$

θ_A and θ_C are the surface coverages of acetaldehyde and crotonaldehyde, respectively. θ^{sat} is the saturation coverage, which is obtained from the normalization procedure highlighted in Section 5.1.1. Note that the coverages of the two species were normalized separately, and their sum should equal 2, but due to the stoichiometry of the reaction (2A → C) $\theta^{sat} = 1.5$. k_A^{ad} and k_A are the rate constants for acetaldehyde adsorption and condensation, respectively. The same kinetic equations were used for the dosing and purging parts, with the main difference being that during purging $k_A^{ad} = 0$.

Eqns. 7.2 and 7.3, however, do not provide a good description of the experimental data. It can be assumed that there is a contribution from another species to the integrated absorbance. This species can be seen in Figure 7.1b, where a hump in the crotonaldehyde data is particularly apparent during the time interval 0 – 5 min. Deconvolution of the crotonaldehyde peak unravels the contributing species (Figure 7.2). It is evident that there are a number of peaks which appeared in the carbonyl region during the initial minutes of CH_3CHO adsorption.

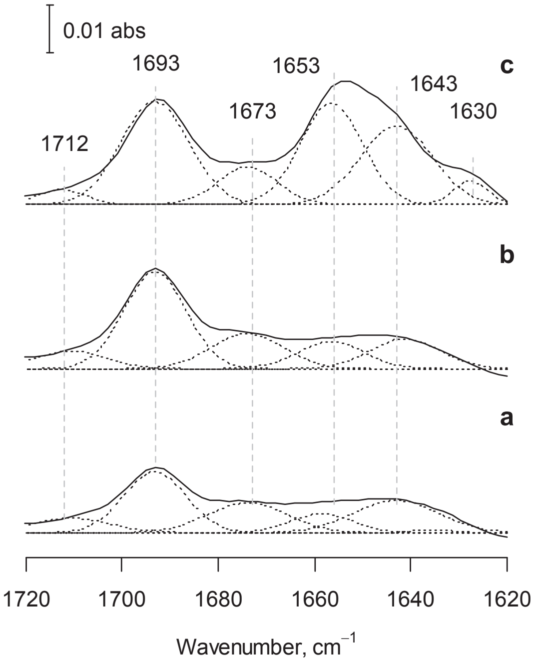

Figure 7.2: Deconvolution of absorption bands in the carbonyl vibration region, using Gaussian functions, for data recorded during exposure of TiO_2 to acetaldehyde. (a) during acetaldehyde adsorption, at t = 6 min, where the 1643 cm^{-1} peak reaches is maximum; (b) at a later time, with t = 9 min, where the 1643 cm^{-1} peak has decreased slightly; and (c) during the conversion of acetaldehyde to crotonaldehyde, at t = 15 min, where the 1643 cm^{-1} peak has merged with the crotonaldehyde carbonyl peak.

Among them was a peak at 1643 cm^{-1}. This peak gained in intensity during the first 3 min, and unfortunately merged with the already-forming crotonaldehyde band at 1653 cm^{-1} (Figure 7.2 a – c). A reasonable hypothesis for the unknown 1643 cm^{-1} peak is that it is caused by the adsorption of gas-phase acetaldehyde dimers. Acetaldehyde, being a carbonyl compound, is expected to dimerize in gas-phase. A textbook example of such interaction is the gas-phase dimerization of acetic acid, wherein the dimers are stable even at elevated temperatures [128]. Similar behaviour was observed for CH_3CHO since as early as 1929 [129].

7.1.1.2. DFT calculations

DFT calculations were performed in order to investigate the possibility of gas-phase acetaldehyde dimers co-adsorbing with acetaldehyde. First, the structure of the acetaldehyde dimer in gas-phase had to be obtained. There are a number of possibilities, which were presented in the work of Hermida-Ramón *et al* [130], and are shown in Figure 7.3. Structure A was found to have the lowest energy. According to our calculations they are $\Delta E = -16.4$ kJ mol^{-1} and $\Delta H = -15.10$ kJ mol^{-1}, which is in agreement with the value reported by Hermida-Ramón of $\Delta E = -16.57$ kJ mol^{-1}, obtained with MP2/6-311+G(2d,p) [130]. It is also close to the only available experimental value, that we are aware of, $\Delta H = -16.4$ kJ mol^{-1}, as reported by Curtiss and Blander [131].

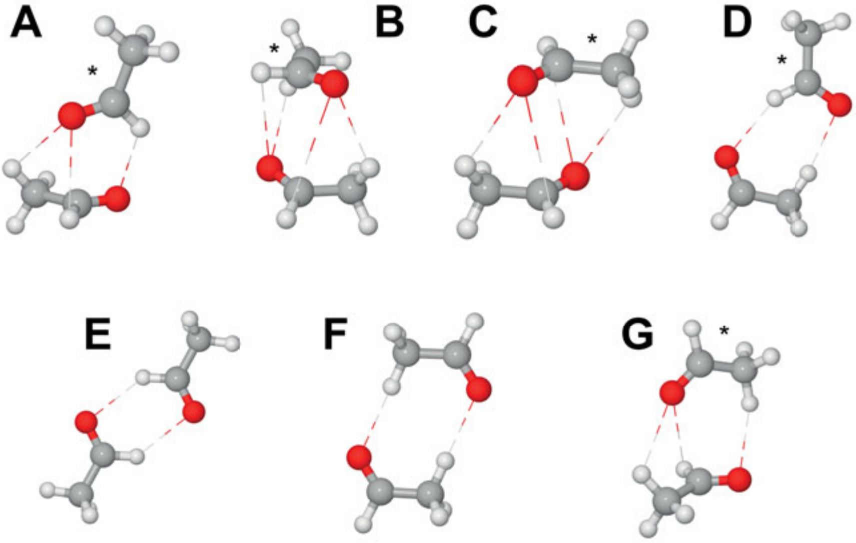

Figure 7.3: Optimized geometries for seven different dimer structures of acetaldehyde in gas-phase. Structures taken from [130].

The molecular structures of acetaldehyde and its most stable dimer, adsorbed onto the (101) anatase cluster model, are presented in Figure 7.4. The adsorption energy for acetaldehyde was calculated to be ΔE = –79.79 kJ mol^{-1}. For its dimer, a slightly lower ΔE = –77.85 kJ mol^{-1} was obtained. The similarity between these two values can be related to the adsorption geometry, which is similar in both cases, and the equal number of bonds formed with the surface.

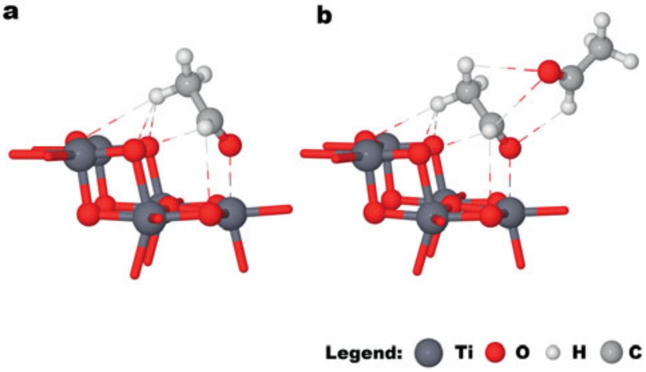

Figure 7.4: (a) Calculated equilibrium structures of crotonaldehyde, and (b) of water, adsorbed on the anatase (101) surface of the $Ti_5O_{10} \times 8H_2O$ cluster.

The calculated ν(C=O) vibrational frequency of adsorbed acetaldehyde was 1690 cm^{-1}, which is in good agreement with the experimental value of 1693 cm^{-1}. For the adsorbed dimer, the ν(C=O) frequency of the interacting molecule is down-shifted to 1653 cm^{-1}, which agrees well with the unknown species frequency of 1643 cm^{-1}, observed during CH_3CHO adsorption on the TiO_2 surface (Figure 7.2 a – c).

7.1.1.3. Extended kinetic model for acetaldehyde adsorption and condensation

The fate of the adsorbed acetaldehyde dimers is determined by thermochemistry. They can either desorb, back into the gas-phase with ΔG = -13.4 kJ mol^{-1} (eqn. 7.4), or decompose. There are two possibilities for the latter case. In the first, one of the acetaldehyde units returns to the gas-phase with ΔG = -33.28 kJ mol^{-1} (eqn. 7.5). In the second case, the dimer decomposes into two adsorbed CH_3CHO units, with ΔG = -60.16 kJ mol^{-1} (eqn. 7.6).

$$(CH_3CHO)_2^{ad} \xrightarrow{k_D^{des}} (CH_3CHO)_2^{gas} \quad (7.4)$$

$$(CH_3CHO)_2^{ad} \overset{k_D'}{\rightarrow} CH_3CHO^{ad} + CH_3CHO^{gas} \quad (7.5)$$

$$(CH_3CHO)_2^{ad} \overset{k_D}{\rightarrow} CH_3CHO^{ad} + CH_3CHO^{ad} \quad (7.6)$$

Based on these three possible reaction paths, an improved kinetic model for the adsorption and condensation of CH_3CHO was constructed taking into account the surface-bound dimer.

$$\frac{d\theta_D}{dt} = k_D^{ad}(\theta^{sat} - \theta_A - \theta_C - \theta_D) - (k_D + k'_D + k_D^{des})\theta_D \tag{7.7}$$

$$\frac{d\theta_A}{dt} = k_A^{ad}(\theta^{sat} - \theta_A - \theta_C - \theta_D) + (2k_D + k'_D)\theta_D - k_A^{cond}\theta_A^2 \tag{7.8}$$

$$\frac{d\theta_C}{dt} = \frac{1}{2}k_A^{cond}\theta_A^2 \tag{7.9}$$

The new variables introduced in eqns. 7.2 and 7.3 are: θ_D, which is the surface coverage of dimeric CH_3CHO; k_D^{ad}, which is the dimeric CH_3CHO adsorption rate constant; and k_D, k'_D, and k_D^{des}, which are the rate constants of dissociation into two adsorbed monomers, one adsorbed monomer, and complete desorption of the entire dimer, respectively. Once again, during the purging phase the model was reused, by enforcing $k_D^{ad},\ k_A^{ad} = 0$.

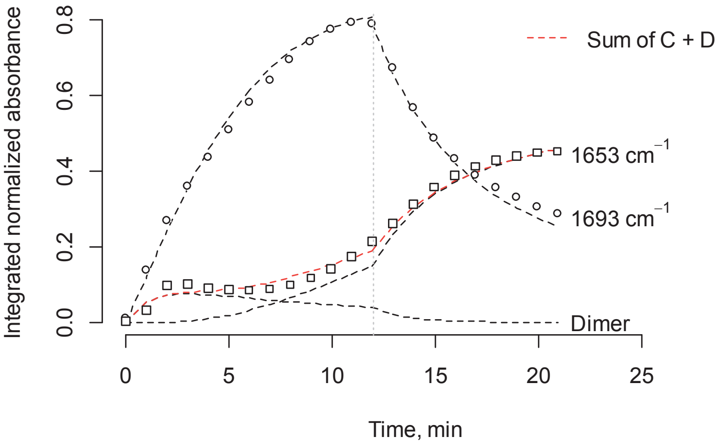

Figure 7.5: Time-traces of the integrated FTIR absorption bands for acetaldehyde adsorption and condensation on TiO_2. The dashed curves show the results from the generalized model (eqns. 7.7 – 7.9), including the acetaldehyde dimer.

Fitting simulated data, based on eqns. 7.7 and 7.8, directly to the normalized and integrated spectral data in Figure 7.1 was complicated due to the difficulties of isolating the contributions of each of the species to it. Both the dimeric acetaldehyde and crotonaldehyde carbonyl bands occurred in the same region of the IR spectrum. This prohibited the unambiguous deconvolution, and instead the integrated data for crotonaldehyde was fitted with the sum of eqns. 7.7 and 7.9. It became evident that inclusion of dimers in the model improved the description of the spectroscopic data significantly. An evidence for that is the R^2 factor of the fit, which increased from 0.81 to 0.97.

7.1.1.4. Overview of results from kinetic modelling

The inclusion of the dimer in the kinetic equations provides an extra source of acetaldehyde, lowering its adsorption rate from 1.82 to 1.4 × 10^{-3} s^{-1}. The adsorption rate constant of the dimer was found to be 1.26 × 10^{-3} s^{-1}, which is close to that of acetaldehyde, and in line with the predictions from DFT calculations for the similar binding energies of the two species. Regarding the reaction pathways, through which the dimer is channeled on the surface, they clearly depend on the number of available adsorption sites. During dosing the CH_3CHO coverage is high and the dimer is channeled through all three suggested pathways. Dissociation into two adsorbed units, however, is favored. During this period k_D^{des}, k_D' and k_D were found to be 3.39, 4.16 and 4.19 × 10^{-3} s^{-1}, respectively. As more surface sites are freed during purging, only dissociation into two adsorbed units is observed in this period, with $k_D = 4.49 \times 10^{-3}$ s^{-1}.

It is interesting that regardless of the presence of the dimer, the aldol condensation of acetaldehyde increases significantly during the purging. Without the dimer the rate increased from 1.77 to 4.13 × 10^{-3} s^{-1}, and with the dimer – from 1.26 to 5.35 × 10^{-3} s^{-1}. There are two effects that could explain this observation. First, the condensation rate of acetaldehyde could benefit from the higher CH_3CHO coverage in the beginning of the purging phase. Then θ_A approaches θ^{sat}, which brings the molecules closer to eachother, and leads to a higher reaction rate. The second effect could be associated with the presence of the dimer, or the formation of multilayers of interacting CH_3CHO molecules, during the first minutes. In order for two acetaldehyde units to condense, one of them must be activated by the $Ti \leftarrow O = C$ interaction, which polarizes the carbonyl group and increases the partial charge of the carbonyl carbon atom. However, transfer of electron density within the dimeric structure may lower the charge of this carbonyl carbon, diminishing its reactivity in the aldol reaction. A proof of this is obtained from DFT calculations, where it was found that the partial charge of the carbon in the carbonyl group is lowered from 0.351 in the surface-bound acetaldehyde, to 0.253 in the surface-bound dimer.

7.1.2. Kinetics of acetaldehyde photo-oxidation on TiO_2 and SO_4 – modified anatase TiO_2 films

In this section the photo-oxidation of CH_3CHO on the TiO_2 and SO_4 modified TiO_2 films is studied. The surface reaction pathways are investigated in depth, using micro-kinetic modelling. The FTIR spectroscopic data was fitted with detailed kinetic equations, in order to obtain the concentrations of reaction products and the corresponding rate constants. The effect of surface sulfation on reaction pathways, and deactivation of the catalyst was studied in terms of site inhibition, i.e. accumulation of intermediates on the surface.

7.1.2.1. Overview of FTIR spectroscopy on TiO_2.

On the pristine TiO_2 (Figure 7.6) dosing with acetaldehyde resulted in the formation of a carbonyl peak at 1693 cm^{-1}, due to the acetaldehyde υ(C=O) vibration, and a number of less intensive peaks at 1653, 1421, 1376, 1355, 1168, 1128 and 1099 cm^{-1}. Upon purging with synthetic air, the intensity of the large peak at 1693 cm^{-1} decreased, while the intensity of the peak at 1653 cm^{-1} increased synchronously. A new band is, at the same time, formed at 1629 cm^{-1}. These two peaks were assigned to the υ(C=O) and υ(C=C) vibrations of crotonaldehyde, which is formed on the surface due to aldol condensation of CH_3CHO. Another peak observed at 1168 cm^{-1} was assigned to the υ(C–C) vibration mode of crotonaldehyde.

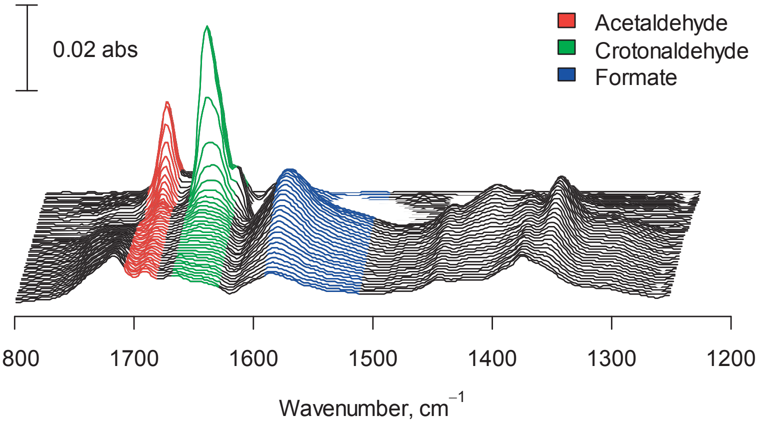

Figure 7.6: *In situ* FTIR data for the first reaction cycle on TiO_2. The regions of interests are color – coded and the integration ranges to obtain the kinetic data for major intermediates are also shown.

During photocatalytic oxidation, the following changes were noted in the FTIR spectra. The carbonyl peak at 1653 cm^{-1} decreased along with the one at 1168 cm^{-1}. This was accompanied with the formation of a wide peak at 1580 cm^{-1}, which was assigned to multiple differently coordinated formate species. Similarly, the peaks at 1376 cm^{-1} and 1355 cm^{-1}, can be attributed to the δ(CH) and symmetric OCO vibrations of formate, respectively. New, weaker absorbance bands also appeared at 1444 cm^{-1} and 1409 cm^{-1}, signalling the formation of small amounts of acetic acid species.

7.1.2.2. Overview of FTIR spectroscopy on SO_4 – modified TiO_2.

On SO_4 modified TiO_2 (Figure 7.7) a different picture emerged from the FTIR spectra. During dosing, an intense peak was formed at 1698 cm^{-1}. It was assigned to surface-bound CH_3CHO, similarly as on the pristine TiO_2 surface, and is a doublet peak with a feature at 1684 cm^{-1}, likely due to acetaldehyde coordinated to surface SO_4 groups. This is supported by a simultaneous decrease in the absorbance, observed at 1336 and 1292 cm^{-1}, where the characteristic vibrations of SO_4 groups are expected [60; 132; 133].

During purging with synthetic air, the large carbonyl peak decreased slightly due to desorption of acetaldehyde. This was, however, the only change in the spectra during this period. No condensation reaction was observed on the sulphated TiO_2, in contrast to pure TiO_2. This is likely due to a stronger interaction between CH_3CHO and the sulphate groups.

During UV illumination two consecutive reactions were distinguished. First, the peak at 1698 cm^{-1} was consumed. This was followed by the appearance of a new peak at 1656 cm^{-1}, similar to the crotonaldehyde peak observed on the pristine TiO_2 surface. However, since the peak at 1656 cm^{-1} was formed during the photocatalytic reaction, and not spontaneously during the purging phase, a different reaction mechanism had to be considered. Most likely, another condensation product is formed, which however is unsaturated as it lacks the 1629 cm^{-1} feature, associated with the double bond of crotonaldehyde. Evidences are inconclusive regarding this species, but it was observed that the newly formed peak at 1656 cm^{-1} was promptly consumed.

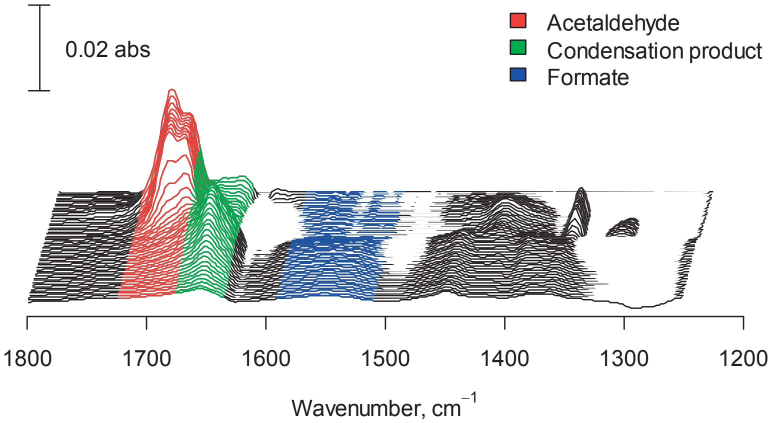

Figure 7.7: *In situ* FTIR data for the first reaction cycle on SO_4 – modified TiO_2. The regions of interests are color coded and the integration ranges to obtain the kinetic data for the different vibrational modes are indicated.

A weak, broad absorbance band appeared at 1553 cm^{-1}, which corresponds to surface-bound formate species. The much weaker intensity of the peaks associated with formate, could be attributed either to a rapid desorption of those species, due to the elevated surface acidity of sulfated TiO_2, or to a more effective photocatalytic reaction, resulting in their complete mineralization.

7.1.2.3. Two-site model for the first step of the photo-oxidation of acetaldehyde.

A detailed study on the photo-fragmentation mechanism of CH_3CHO on the TiO_2 surface was reported by Zehr *et al* [134]. In UHV experiments he found that the first step is the cleavage of the C–C bond. This leads to a release of a $^{\bullet}CH_3$ radical, and a surface-bound CHO fragment which is further oxidized to surface-bound formate species. In the same study it was reported, that the C-C cleavage photoreaction has two components, associated with different reaction rates.

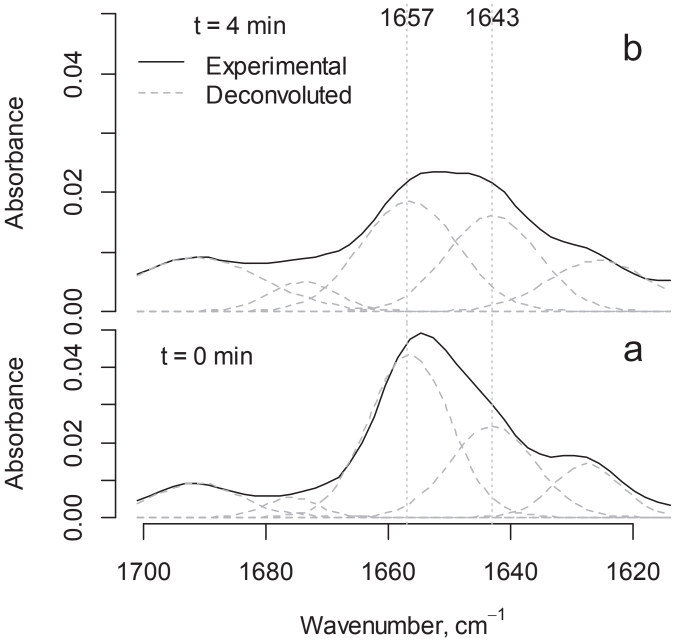

Figure 7.8: Deconvolution of the main carbonyl peak of crotonaldehyde on TiO_2 surface prior (a) and after 4 min of UV illumination (b).

Similar behaviour was observed in our experimental data during the first step of the photo-oxidation reaction, both on the pristine and the SO_4 – modified TiO_2 surfaces. The example given in this section is for crotonaldehyde, which is the starting species in the photo-oxidation reaction on the pristine TiO_2 surface. The same model is applicable for acetaldehyde on $SO_4 – TiO_2$.

Deconvoluting the main carbonyl peak of crotonaldehyde in the FTIR spectra (Figure 7.8) reveals that it is composed of two peaks, positioned at 1657 and 1643 cm^{-1}, respectively. Comparing Figure 7.8a and Figure 7.8b, it is found that one of the deconvoluted peaks decreased much faster during the first minutes of UV illumination. Thus, we can assume that the crotonaldehyde photo-oxidation follows a reaction pathway, similar to the one reported by Zerh *et al.* We propose that aldehyde molecules are coordinated to two different reaction sites, which are associated with asymmetric reactivity. Based on this assumption, a kinetic model taking into account the contributions of these sites in the photocatalytic oxidation rate is devised (eqn. 7.10).

$$C(T) = ZC_0e^{-k_{B_1}t} + Z'C_0e^{-k_{B_2}t}, \tag{7.10}$$

where k_{B_1} and k_{B_2} are the rate constants for the slow and for the fast reactions, respectively, and Z and Z' are the fractions of each type of sites (Z + Z' = 1). A typical fit of experimental data with eqn. 7.10 is shown in Figure 7.9.

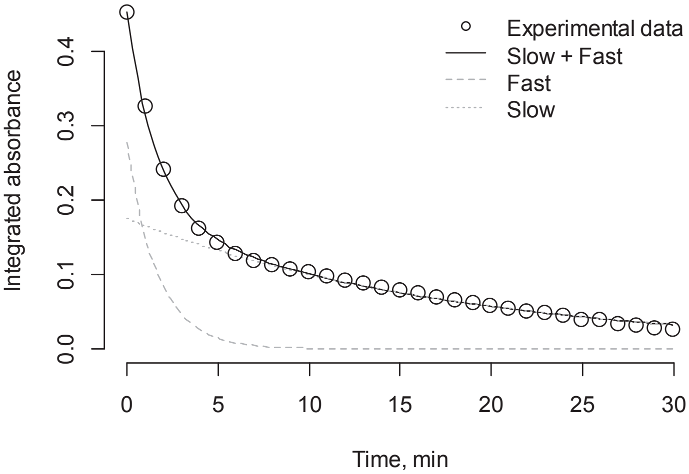

Figure 7.9: Typical fit for crotonaldehyde photo-degradation on the pure TiO_2 using the two-site kinetic model (eqn. 7.10).

7.1.2.4. Kinetic model for pristine TiO_2

During dosing, acetaldehyde (A) is adsorbed on TiO_2 and small amounts of crotonaldehyde (B) are formed due to aldol condensation (eqn. 7.11).

$$2A_g \xrightarrow{k_A^{ad}} 2A_{ad} \xrightarrow{k_{A-B}^{DOSE}} B_{ad} + H_2O \tag{7.11}$$

This process is limited by the amount of available sites, which is inversely proportional to the saturation coverage θ^{sat}. The kinetic equations for this reaction, expressed by the surface coverage of the species, are:

$$\frac{d\theta_A}{dt} = k_A^{ad}(\theta^{sat} - \theta_A - \theta_B) - k_{A-B}^{DOSE}\theta_A^2 \tag{7.12}$$

$$\frac{d\theta_B}{dt} = \frac{1}{2}k_{A-B}^{DOSE}\theta_A^2, \tag{7.13}$$

where θ_A and θ_B are the surface coverages for acetaldehyde an crotonaldehyde. k_A^{ad} is the rate constant of acetaldehyde adsorption, and k_{A-B}^{DOSE} is the rate constant of crotonaldehyde formation through condensation of the adsorbed acetaldehyde.

During purging in synthetic air the aldol condensation continues, which ultimately converts all of the adsorbed acetaldehyde into crotonaldehyde (i.e. the reaction follows eqns. 7.12 and 7.13, but $k_A^{ad} = 0$):

$$2A_{ad} \xrightarrow{k_{A-B}^{PURGE}} B_{ad} + H_2O_{ad} \tag{7.14}$$

The corresponding kinetic equations for this process are:

$$\frac{d\theta_A}{dt} = -k_{A-B}^{PURGE}\theta_A^2 \tag{7.15}$$
$$\frac{d\theta_B}{dt} = \frac{1}{2}k_{A-B}^{PURGE}\theta_A^2 \tag{7.16}$$

During UV illumination we assumed the following reaction pathways: First, crotonaldehyde is oxidized through the two reaction pathways, discussed in Section 7.1.2.3. A major product of this oxidation is surface-bound formate (C), which is further oxidized to CO_2 and H_2O (eqns. 7.17 – 7.18).

$$2A_{ad} \xrightarrow{k_{A-B_1}^{UV}} B_{ad} \xrightarrow{k_{B_1-C}^{UV}} 4C_{ad} \xrightarrow{k_C^{UV}} CO_2, H_2O \tag{7.17}$$
$$2A_{ad} \xrightarrow{k_{A-B_2}^{UV}} B_{ad} \xrightarrow{k_{B_2-C}^{UV}} 4C_{ad} \xrightarrow{k_C^{UV}} CO_2, H_2O \tag{7.18}$$

However, the crotonaldehyde coverage could be decreased through other reactions, e.g. through oxidation to formaldehyde or acetic acid. We have included this possibility implicitly in the model, by introducing two extra rate constants responsible for channelling of crotonaldehyde through unknown reaction pathways. One is corresponding to the fast reaction pathway ($k_{U_1}^{UV}$), and one – to the slow reaction pathway ($k_{U_2}^{UV}$), as shown in eqn. 7.19.

$$B_{ad} \xrightarrow{k_{U_1}^{UV}, k_{U_2}^{UV}} other\ reactions \tag{7.19}$$

Based on eqns. 7.17 – 7.19, the following set of kinetic equations describes the complete reaction pathway for acetaldehyde on TiO_2:

$$\frac{d\theta_A}{dt} = -k_{A-B_1}^{UV}\theta_A^2 - k_{A-B_2}^{UV}\theta_A^2 \tag{7.20}$$
$$\frac{d\theta_B}{dt} = \frac{d\theta_{B_1}}{dt} + \frac{d\theta_{B_2}}{dt} \tag{7.21}$$
$$\frac{d\theta_{B_1}}{dt} = \frac{1}{2}k_{A-B_1}^{UV}\theta_A^2 - k_{B_1-C}^{UV}\theta_{B_1} - k_{U_1}^{UV}\theta_{B_1} \tag{7.22}$$

$$\frac{d\theta_{B_2}}{dt} = \frac{1}{2} k_{A-B_2}^{UV} \theta_A^2 - k_{B_2-C}^{UV} \theta_{B_2} - k_{U_1}^{UV} \theta_{B_2} \tag{7.23}$$

$$\frac{d\theta_C}{dt} = 4\left(k_{B_1-C}^{UV} \theta_{B_1} + k_{B_2-C}^{UV} \theta_{B_2}\right) - k_C^{UV} \theta_C \tag{7.24}$$

where θ_A, θ_B and θ_C are the coverages of acetaldehyde, crotonaldehyde and formate, respectively. As discussed above the crotonaldehyde coverage is split into two contributions, from the fast and slow surface sites, resp. θ_{B_1} and θ_{B_2}. All rate constants for the following reactions on these two types of sites are noted accordingly. k_{A-B}^{UV} is the rate constant for acetaldehyde condensation during the UV illumination phase. k_{B-C}^{UV} is the rate constant of crotonaldehyde photo-oxidation to formate. k_U^{UV} is the rate constant of crotonaldehyde – to other intermediates conversion. k_C^{UV} is the constant of formate photo-oxidation.

7.1.2.5. Kinetic model for sulfated TiO_2

Analogously to the model for pristine TiO_2, the following reaction scheme was devised for the adsorption and photo-oxidation of acetaldehyde on SO_4 – TiO_2:

$$A^{gas} \underset{k_A^{des}}{\overset{k_A^{ad}}{\leftrightarrow}} A \xrightarrow{k_{A-C}^{UV}} 2C \xrightarrow{k_C^{UV}} CO_2, H_2O \tag{7.25}$$

$$A^{gas} \underset{k_A^{des}}{\overset{k_A^{ad}}{\leftrightarrow}} A \xrightarrow{k_{A-U}^{UV}} U \tag{7.26}$$

Eqn. 7.25 describes the conversion of acetaldehyde to formate and eqn. 7.26 describes the parallel reaction pathway, a product of which is the unknown surface species, with a carbonyl band at 1656 cm^{-1}. Formate is a minor surface intermediate on the SO_4 – TiO_2 surface, hence most of the adsorbed acetaldehyde is channelled through eqn. 7.26.

Since no condensation of acetaldehyde was observed during its adsorption on the SO_4 – TiO_2 surface, the kinetic equations during this phase reflect only on its accumulation, until saturation coverage is reached (eqn.7.27). Consequently, during the purging period only the slight desorption of acetaldehyde is observed (eqn.7.28).

$$\frac{d\theta_A}{dt} = k_A^{ad}\left(\theta^{sat} - \theta_A\right) - k_A^{des} \theta_A \tag{7.27}$$

$$\frac{d\theta_A}{dt} = -k_A^{des} \theta_A \tag{7.28}$$

The photocatalytic oxidation reaction is then described with the following set of equations:

$$\frac{d\theta_{A_1}}{dt} = -k_{A_1-C}^{UV}\theta_{A_1} - k_{A_1}^{des}\theta_{A_1} - k_{A_1-U}^{UV}\theta_{A_1} \tag{7.29}$$

$$\frac{d\theta_{A_2}}{dt} = -k_{A_2-C}^{UV}\theta_{A_2} - k_{A_2}^{des}\theta_{A_2} - k_{A_2-U}^{UV}\theta_{A_2} \tag{7.30}$$

$$\frac{d\theta_{C}}{dt} = 2(k_{A_1-C}^{UV}\theta_{A_1} + k_{A_2-C}^{UV}\theta_{A_2}) - k_{C}^{UV}\theta_{C} \tag{7.31}$$

7.1.2.6. Results from micro-kinetic modelling

The micro-kinetic fit for four reaction cycles on both TiO_2 and sulphated TiO_2 is presented in Figure 7.10.

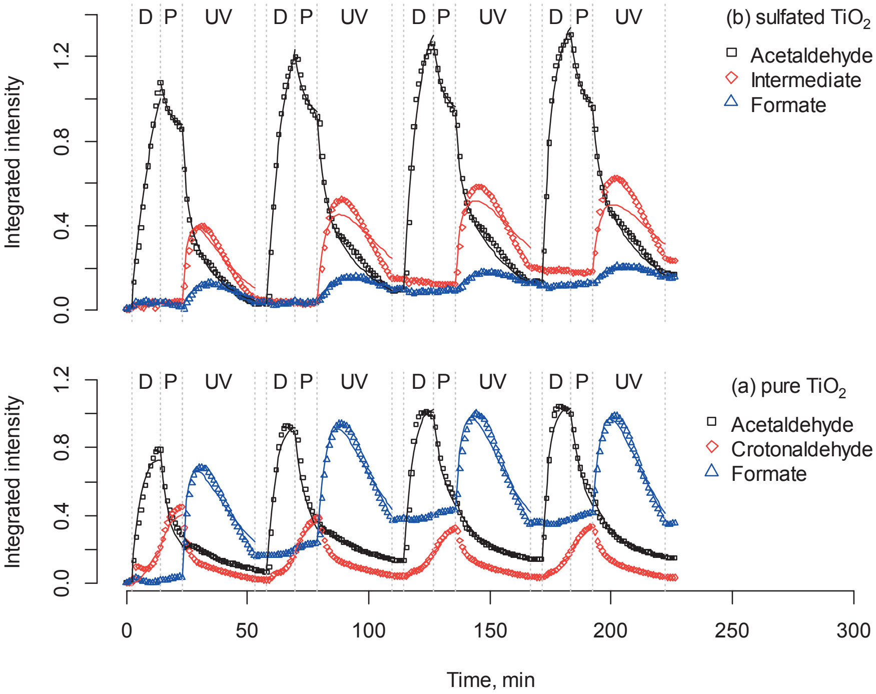

Figure 7.10: Surface coverage of adsorbed acetaldehyde, crotonaldehyde, and formate as a function of reaction time during four consecutive cycles of acetaldehyde gas dosing (D), purging in synthetic air (P), and UV irradiation (UV), respectively, on (a) TiO_2, and (b) SO_4–TiO_2 films. Solid curves represent results from the micro-kinetic modelling (see text).

Table 7.1 summarizes the rate constants obtained from the asymmetric surface sites model (eqn. 7.10), as a function of cycle number. As noted before, the two rate constants correspond to the fast and slow photo-oxidation pathways. The contribution of each pathway in the total observed photo-oxidation rate is quantified by the weighing factors in eq. 7.10. The physical meaning of these weighting factors is the fraction of total reaction sites available for the corresponding reaction.

Table 7.1: Fast and slow reaction rate constants and fractional site occupancies for the photo-oxidation of crotonaldehyde (on TiO_2) and acetaldehyde (on SO_4–TiO_2).

TiO_2 surface				
Cycle no.	Sites. %		Rate constant, $\times 10^{-3}[s^{-1}]$	
	B_1	B_2	$k_{B_1}^{UV}$	$k_{B_2}^{UV}$
1	61.31	38.69	8.513	1.621
2	63.19	36.81	3.955	0.910
3	49.80	50.20	6.624	1.013
4	46.57	53.43	5.497	1.826
SO_4–TiO_2 surface				
Cycle no.	Sites. %		Rate constant, $\times 10^{-3}[s^{-1}]$	
	A_1	A_2	$k_{A_1}^{UV}$	$k_{A_2}^{UV}$
1	45.67	54.33	9.206	3.777
2	39.04	60.96	6.991	3.476
3	34.26	65.74	8.194	4.472
4	32.69	67.31	9.826	5.575

Similar trends were observed both for TiO_2 and $SO_4 – TiO_2$. On both surfaces there was an approximately one-fold difference between the rate constants of the two reaction pathways. The deactivation of the photocatalyst, with respect to the two reaction pathways, was also similar in both materials. After the first cycle, a notable decrease in the rate constants was observed, which was associated with accumulation of intermediates and site inhibition [135; 136; 137; 138].

The main difference between the two surfaces was that for the SO_4 – modified surface the slow reaction had a higher contribution to the overall photocatalytic activity. A possible explanation for this observation comes from the theoretical work of Nissar *et al* on the binding energies of SO_4-species on the TiO_2 surfaces [92]. It was found that these are preferentially adsorbed onto highly-reactive sites, such as oxygen defects, and in general on the more reactive {001} surfaces. Thus, it is logical that the "fast" reaction sites became partly populated during the SO_4 modification. Consequently, they will not be available for acetaldehyde adsorption and hence will contribute less to the overall acetaldehyde degradation. Furthermore, other sulfur – containing species, which might be a product of the SO_2 – photofixation, are found to be a main cause for catalyst deactivation in some catalytic reactions [139].

The data, presented as overall photo-oxidation rates, along with the other rate constants for the full cycle (dose, purge, reaction) are summarized in Tables 7.2 and 7.3 for TiO_2 and the SO_4 – modified TiO_2, respectively. During the dosing period similar trends were observed for both the modified and unmodified photocatalyst. With the accumulation of reaction intermediates there were less adsorption sites available in each new cycle, which led to a faster saturation with acetaldehyde. Similarly, due to the accumulation of species occupying surface sites, the diffusion of acetaldehyde on the surface was limited, and consequently the acetaldehyde condensation (Eqn. 7.14) became slower during each subsequent purging cycle. This led to accumulation of detectable amounts of acetaldehyde (A) on the pure TiO_2. On the SO_4 – modified surface only desorption of acetaldehyde was observed.

Table 7.2: Reaction rate constants on TiO_2 obtained from micro-kinetic modelling.

Rate constant, $\times 10^{-3} [s^{-1}]$

Cycle no.	k_A^{ad}	k_{A-B}^{DOSE}	k_{A-B}^{PURGE}	k_{A-B}^{UV}	k_{B-C}^{UV}	k_U^{UV}	k_C^{UV}
1	1.996	2.192	5.949	4.057	6.227	3.907	1.626
2	2.572	1.213	3.616	2.190	4.551	0.314	1.066
3	3.152	0.937	2.173	2.984	7.147	0.491	1.332
4	3.651	1.045	2.185	2.717	6.715	0.608	1.436

On the unmodified TiO_2 a notable decrease in the rate of crotonaldehyde photo-oxidation was observed after the first UV cycle. The reason for this is once again attributed to accumulation of surface intermediates and catalyst deactivation. The rate of formate photo-oxidation (k_C^{UV}) was not affected by the number of cycles, hinting that formate is the last intermediate in the pathway, and its photo-oxidation is not dependent on the total number of sites available, hence its removal is the step, limiting the entire pathway.

Table 7.3: Reaction rate constants on SO_4 – TiO_2 obtained from micro-kinetic modelling.

Rate constant, $\times 10^{-3} [s^{-1}]$

Cycle no.	k_A^{ad}	k_A^{des}	k_{A-C}^{UV}	k_{A-U}^{UV}	k_C^{UV}
1	2.299	4.624	0.132	4.025	1.749
2	3.593	4.460	0.089	3.576	1.133
3	4.682	4.546	0.075	4.460	1.004
4	5.774	4.976	0.076	3.461	1.004

On the sulfated TiO_2 the photo-degradation rate remained stable through cycles 1 – 4. On this surface the accumulation of formate was not a limiting step, as it no significant accumulation of such species was observed.

7.2. Preferentially orientated TiO_2 thin films (Papers III, IV, V).

This section summarizes results on the effects of preferential <001> orientation on the photocatalytic activity of sputter-deposited anatase TiO_2 films.

7.2.1. Effect of deposition conditions on TiO_2 structure, morphology and optical properties (Paper).

Eight sets of TiO_2 thin films with increasing preferential <001> orientation were deposited via reactive DC sputtering using the methodology described in Section 4.1.2. The substrates were standard 1 mm thick microscopy glass slides, which were pre-cut in 50 × 25 mm size. The deposited TiO_2 was covering the entire area of the slides. The films crystallographic, structural and optical properties were determined using GI-XRD, TEM, AFM and UV/Vis techniques as described in Chapter 4.

Table 7.4: Structural and optical properties of the anatase TiO_2 films. From left to right: oxygen partial pressure during deposition (P_{O_2}), film thickness (*d*), mean crystallite size ($\bar{d}_{\text{xrd}}$), degree of preferential <001> orientation (η_{001}), fraction of exposed {001} facets (A_{001}), refractive index (*n*), packing density (*PD*), and AFM r.m.s. surface roughness ($R_{r.m.s}$).

P_{O_2}, mTorr	*d*, nm	$\bar{d}_{\text{xrd}}$	η_{001}, %	A_{001}, %	*n*	*PD*, %	$R_{r.m.s}$, nm
0.64	574	24	2	12	2.36	93	1.3
0.56*	518	26	7	14	2.32	91	1.4
0.95	579	26	12	17	2.31	91	1.1
0.8*	485	25	23	26	2.28	90	1.3
1.25	664	22	25	27	2.20	87	1.4
0.95*	557	22	28	30	2.19	86	1.2
1.10*	474	21	35	37	2.17	85	1.3
1.53	697	18	38	41	2.08	81	1.6

A summary of the effects of altering the partial oxygen pressure in the deposition chamber (P_{O_2}) on selected structural, morphological and optical properties of the ensuing TiO_2 films is presented in Table 7.4. Note that, as mentioned in Section 4.2.2 half of the samples were deposited with a set of new Ti targets, while the rows marked with asterisk in Table 7.4 correspond to films deposited with another set of targets, which were eroded after prolonged use. The eroded targets have less active area available for sputtering, which resulted in a higher degree of preferential <001> orientation at lower P_{O_2} settings. The sputtering rates were also lower, yielding thinner films for the same deposition time, which was 35 min for all samples discussed in this section.

All films exhibited similar structure and morphology, independently of P_{O_2}. They were thick and solid, with a columnar growth structure, and a surface roughness of the order of 1.3 ± 0.1 nm. The major difference across samples was the increasing preferential orientation (η_{001}) leading to an increase in the exposed area of {001} facets (A_{001}) from 12 to 41%. The mean crystallite size was found to decrease proportionally, from 26 to 18 nm. Similarly, the refractive index decreased from n = 2.36 to n = 2.08, leading to a decrease of with about 10% in the packing density (*PD*), which was calculated from n. No morphological changes, related to the decrease in PD, were observed in microscopy; hence we can assume that it is associated with small pores enclosed inside the film, and inaccessible for contaminants adsorption. The optical bandgaps of the films were determined (Section 4.7) and no effect of the sputtering conditions was found. A mean value of $E_g \cong 3.3\ eV$ was obtained for all films, which is in a fair agreement with the tabulated value for anatase TiO_2 (E_g = 3.2 eV).

7.2.2. Dependence of <001> orientation on the MB photo-degradation rates

In order to elucidate the effects of the relative abundance of {001} facets on the photocatalytic activity of sputtered anatase TiO_2 films, photocatalytic experiments were conducted in liquid-phase. Methylene blue (MB) dye was employed as a model pollutant, according to the methodology presented in Section 5.2. Figure 7.11 shows kinetic plots for three sputtered TiO_2 films with increasing A_{001}.

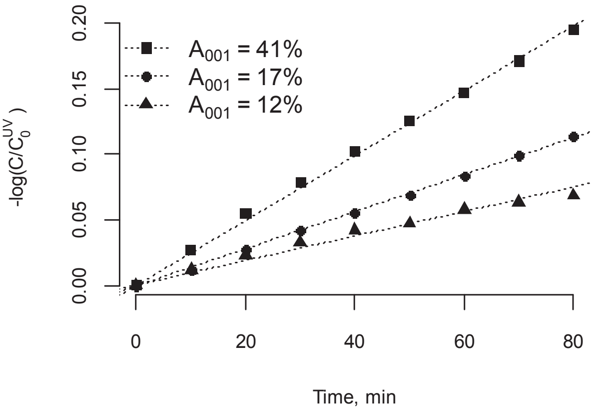

Figure 7.11: Semi-logarithmic plots of normalized MB concentration vs. the reaction time for three samples with increasing A_{001}. Assuming first-order kinetics the slope is determined by the rate of MB photo-oxidation (Section 5.2.1).

The kinetic rate constants of MB removal were found to correlate with the preferential <001> orientation. The results for all 8 sets of films are summarized in Table 7.5. The saturation coverage of MB (C_{sat}^{MB}), obtained during the 40 min dark period in each experiment (Section 5.2.1), was found to be constant for all films. This is in line with the expectations that the 10% increase in porosity is associated with pores, enclosed inside the films and inaccessible for MB.

Table 7.5: Summary of results from the liquid-phase MB tests for anatase TiO_2 films with increasing A_{001}.

A_{001}, %	C_{sat}^{MB}, ppm	k_{MB}, x 10^{-3} min^{-1}
12	0.27	0.96
14	0.25	1.02
17	0.3	1.00
26	0.31	1.31
27	0.28	1.43
30	0.29	1.72
37	0.29	2.27
41	0.28	2.49

The functional dependence $k_{MB}(A_{001})$ was obtained using a model, where the reactivity of the {001} and {101} facets is described by two separate rate constants. The model is based on a simplified construction of the catalytic surface as composed of only two facets. The relative abundance of {001} is obtained via A_{001} and the rest of the surface is comprised of {101}. The model has the following form:

$$k_{MB} = k_{101}(1 - \mathrm{A}_{001})^{x} + k_{001}(f_{001}\mathrm{A}_{001})^{x}, \qquad (7.32)$$

where k_{MB} is the observed MB photo-degradation rate constant; k_{101} and k_{001} are the corresponding rates of the {101} and {001} facets, respectively; x is the reaction order; and f_{001} is a parameter accounting for the different number of surface Ti atoms on the two surfaces. The Ti atom surface densities on {101} and {001} are 5.17 and 6.99 × 10^{14} cm^{-2}, respectively. These values yield f_{001} = 1.35.

The resulting fit of eqn. 7.32 on the experimental data is presented in Figure 7.12. The fitting parameters, obtained for this data were $k_{101} = 0.99 \times 10^{-3}$, $k_{001} = 7.56 \times 10^{-3}$, and x = 2.05. This signifies that the photo-oxidation rate of MB is about 8 times higher on the {001} surfaces, compared with the {101} surfaces. Furthermore, k_{MB} increases with the square of the relative fraction exposed {001} facets.

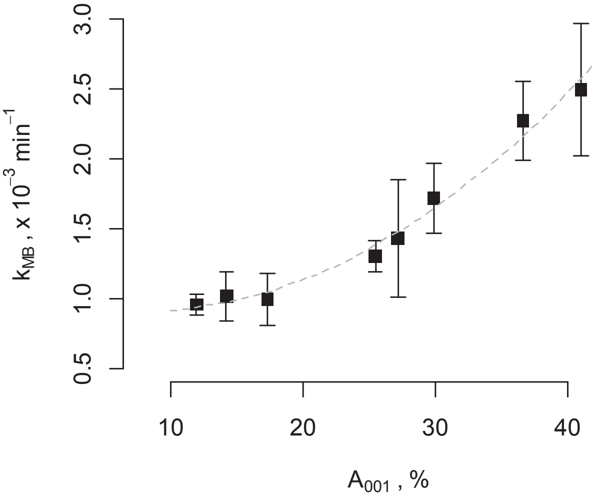

Figure 7.12: MB photo-degradation rate, k_{MB}, as a function of the exposed {001} area, A_{001}. The best fit according eqn. 7.32 is shown as a dashed line.

7.2.3. UV intensity dependence of photocatalytic activity of preferentially <001> oriented TiO_2 films

The presence of {001} facets has a beneficial effect on k_{MB}. This implies, by definition, that the preferentially oriented films exhibit improved quantum efficiency and should utilize light energy more effectively. To probe this hypothesis, photocatalytic experiments were conducted in order to determine the functional dependence of UV light intensity on k_{MB}.

Two films were compared in this study. One – with random orientation (η_{001} = 2%; A_{001} = 12%), and one – with preferential <001> orientation (η_{001} = 25%; A_{001} = 27%). Photocatalytic degradation of MB was conducted at four UV illumination intensities, achieved by moving the UV lamp away from the photocatalytic reactor. The average UV illumination intensity on the film surface was calculated using the LSSE model (Section 5.4.1), and its values were, as follows: 0.382 mW cm^{-2}, 0.158 mW cm^{-2}, 0.085 mW cm^{-2} and 0.053 mW cm^{-2}.

The observed apparent MB photo-oxidation rate constants are plotted for both samples in Figure 7.13. The data was fitted using the model suggested by Mills *et al* (eqn. 7.33) [140].

$$k_{MB} = a \times I^b, \qquad (7.33)$$

where k_{MB} is the apparent rate constant, I – the UV illumination intensity, and a and b are constants. The physical meaning of a is of the UV independent rate constant, and of b – the reaction order by light intensity.

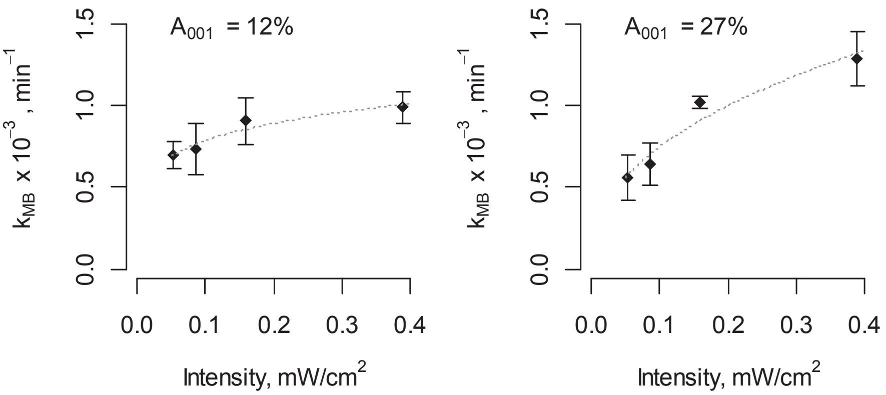

Figure 7.13: k_{MB} as a function of UV intensity for randomly oriented film (A_{001} = 12%) and a film with preferential <001> orientation A_{001} = 27%). The dashed line is the resulting fit from eqn. 7.33.

As expected, the film with a higher preferential <001> orientation exhibited a higher reaction rate. It showed a 30% increase in the apparent rate constant of MB photo-oxidation, and a 60% increase – in the UV independent rate constant. Hence, it is to be expected that at higher intensities the <001> oriented sample will show even better performance. This is also reflected in the reaction order by light intensity (*b*), which was estimated to be 0.2 and 0.4 for the random and orientated film, respectively.

It is reported by Mills *et al* that, as a function of light intensity, the photocatalytic performance exhibits three regions: (*i*), at low intensity the rate increasing linearly with intensity; (*ii*) at medium intensity a square root dependence is observed; and (*iii*) at high intensity the reaction rate becomes independent of intensity [140].

The results in Table 7.6 show that both samples approach the saturation region, at intensities as low as 0.4 mW cm^{-2}. However, the film with preferential <001> orientation is more effective in the given intensity range, and a further increase of k_{MB} can be expected at UV illumination intensities, higher than the range shown in Figure 7.13.

Table 7.6: Kinetic parameters for the photocatalytic degradation of MB by samples with random (A_{001} = 12%) and preferential <001> orientation (A_{001} = 27%).

Parameter	Sample	
	A_{001} = 12%	A_{001} = 27%
Apparent rate constant, k_{MB}	0.986 ± 0.09	1.286 ± 0.17
Intensity independent constant, *a*	1.19	1.95
UV intensity light order, *b*	0.18	0.42

7.3. Reactivity of <001> preferentially orientated TiO_2 films in operando conditions (Paper VI)

In Section 7.2 the results for the functional dependence $k_{MB}(A_{001})$ were presented for sputtered anatase TiO_2 films. A positive effect of the preferential <001> orientation on the photocatalytic performance of the films was observed. As a central topic in this thesis is the use of TiO_2 coatings in indoor air cleaning applications, a logical next step was to confirm that the same beneficial effects would be observed in the gas-phase photocatalytic oxidation of CH_3CHO. This is the topic of this section. It also covers the effects of important operating conditions, namely the catalyst surface temperature (T^{surf}) and relative humidity (*RH*) in the gas-phase, on the photocatalytic activity of the TiO_2 films as well.

The gas-phase photocatalytic experiments were conducted using the setup discussed in Section 5.3. Films with increasing A_{001} were prepared via the approach described in Section 4.1.2 and employed in the investigations. These were deposited on 4 mm thick UV transparent OptiWhite^{TM} substrates (70 × 70 mm squares), simulating a window substrate.

Five batches of films were deposited at P_{O_2} in the range 0.64 – 1.81 mTorr. After heat treatment, the initially amorphous TiO_2 films crystallized into the anatase phase with η_{001} = 2 to 34% (A_{001} = 10 to 36%). Selected structural, crystallographic and optical parameters are listed in Table 7.7.

Table 7.7: Selected parameters of the anatase TiO_2 films. From left to right: deposition partial oxygen pressure (P_{O_2}), film thickness (*d*), average crystallite size ($\bar{d}_{xrd}$), degree of preferential <001> orientation (η_{001}), relative abundance of {001} facets at the surface (A_{001}), refractive index (*n*), packing density (*PD*), and AFM surface roughness ($R_{r.m.s}$).

P_{O_2}, mTorr	*d*, nm	$\bar{d}_{xrd}$	η_{001}, %	A_{001}, %	*n*	*PD*, %	$R_{r.m.s}$, nm
0.65	708	21	2	10	2.22	87	1.9
0.95	755	24	9	15	2.21	87	1.8
1.25	716	25	19	22	2.23	88	1.7
1.54	835	22	30	31	2.10	82	2.2
1.82	933	19	34	36	2.05	80	1.8

The film morphology and structure were identical to that of the films employed in Section 7.2. In order to elucidate the effects of crystallinity and surface morphology on the ensuing photocatalytic activity of the films, a commercial sample was introduced as a reference. It was in the form of 70 × 70 mm square of TiO_2 – coated Pilkington Active^{TM} self-cleaning glass (also on a 4-mm thick substrate).

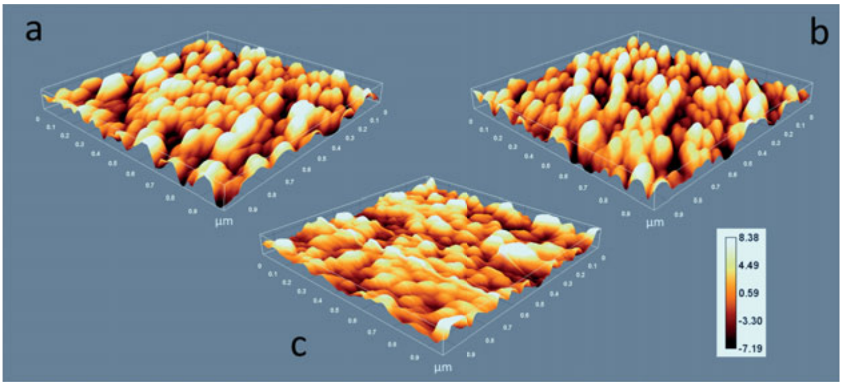

Figure 7.14: AFM images of TiO_2 films prepared by sputter deposition at P_{O_2} = 0.65 mTorr (a) and P_{O_2} = 1.82 mTorr; and AFM image of the Pilkington Active^{TM} sample (c).

The Pilkington Active^{TM} glass has a 15 nm thick anatase TiO_2 coating, deposited by a CVD process [45]. According to literature data it has less developed surface and lower crystallinity compared with our sputtered films. The small thickness of the commercial coating prevented us from obtaining meaningful XRD diffractograms, and consequently structural information about the film, so only AFM analysis was performed (Figure 7.14). $R_{r.m.s.}$ was found to be 0.9 nm, which is less than that of the sputtered films, for which a value of about 2 nm was obtained.

The CH_3CHO photo-oxidation experiments were conducted by measuring the reaction rate, $r_{\mathrm{CH_3CHO}}$, upon cycling the catalyst (3 cycles of UV illumination, 15 min each, separated by 15 min in darkness) at three different RH (0 %, 20 % and 40 %) and T^{surf} (25°C, 40°C and 55°C).

7.3.1. Functional dependence of <001> oriented films in dry and humid conditions

The functional dependence $r_{\mathrm{CH_3CHO}}(A_{001})$ was obtained by measuring the steady state photo-oxidation rate of CH_3CHO for films with increasing A_{001}. The data was fitted with the kinetic model discussed in Section 7.2.2 (eqn. 7.32). A comparison between the result from MB photo-oxidation experiment (recalculated to µmol cm^{-2} min^{-1}), and the dependence obtained for CH_3CHO, in dry and humid (RH = 20%) gas-phase is presented in Figure 7.15.

At RH = 0% (Figure 7.15b) the effect of A_{001} on $r_{\mathrm{CH_3CHO}}$ was comparable to the result observed in liquid-phase MB photo-oxidation (Figure 7.15a). In the former case the relative difference in the activities of {001} and {101} facets was found to be $k_{001}/k_{101} \approx 8$, while for gas-phase CH_3CHO photo-oxidation it was $k_{001}/k_{101} \approx 10$. Thus, for both reactions an order of magnitude higher activity was observed on {001}.

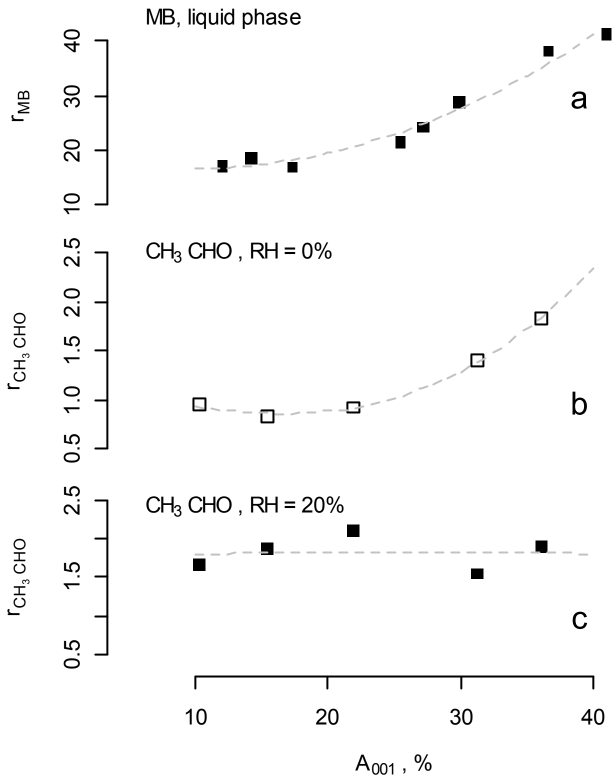

Figure 7.15: Effect of A_{001} on the photocatalytic rate constants of MB in liquid-phase (a), CH_3CHO in gas-phase at RH = 0% (b) and at RH = 20% (c). Dashed curves show the resulting fit of eqn. 7.32, and is added to guide the eye for RH = 20%. All reaction rates are in units of x 10^{-3} μmol cm^{-2} min^{-1}.

The main difference was in the reaction order by A_{001}, which was quadratic in liquid-phase experiments (x = 2.05), and cubic (x = 3.04) for the case of gas-phase CH_3CHO photo-oxidation.

This hints that x is not related to the intrinsic activity of the surface facets, and instead is influenced by the reaction mechanism of the photocatalytic process. Several explanations can be suggested for the quadratic – to – cubic transition. For example, (*i*) difference in the adsorption energies of MB and CH_3CHO; (*ii*) different intermediate reaction kinetics; or (*iii*) different limiting steps in liquid and gas-phase. E.g. in liquid-phase it is the adsorption of reactants, while in gas-phase – the desorption of reaction products, etc.

In any case, the result for RH = 0% confirms the findings from the liquid-phase experiments that {001} surfaces are associated with a higher photoreactivity.

The non-linear functional dependence $r_{CH_3CHO}(A_{001})$ holds only at RH = 0%. As shown in Figure 7.15c, at RH = 20% all samples exhibited similar photocatalytic activity, regardless of A_{001}. At RH = 40% similar result was observed, albeit with a slightly lower rates.

An explanation of this observation can be found in Section 3.1. As it was discussed there in detail, the presence of water on the TiO_2 surface is expected to influence its photocatalytic activity. It can either enhance it, through formation of reactive radicals; or limit it, by imposing a diffusion barrier for both the active surface species and the adsorption of reactant molecules.

7.3.2. Catalyst deactivation

At RH = 0% all samples exhibited deactivation, which is normally observed in anatase TiO_2 [138]. As discussed in Section 7.1, this deactivation is related to the accumulation of intermediates on the catalyst surface, which inhibits active surface sites [135; 136; 137; 138]. Experimental evidence for that can be demonstrated by tracing the change in r_{CH_3CHO} during the three 15 min cycles of UV illumination (for more details on the experiment refer to Section 5.3).

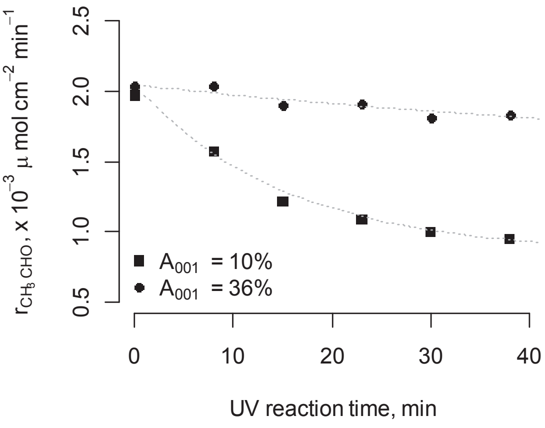

Figure 7.16: Decrease of r_{CH_3CHO} during UV illumination for a randomly oriented (A_{001} = 10%) and preferentially oriented (A_{001} = 36%) TiO_2 films. The data from three 15 min UV illumination cycles is merged in this plot (the first 7 min of each cycle were omitted, in order to compensate for the gas sensor response time). RH = 0% and T^{surf} = 25°C. Lines are added to guide the eye.

An example of the decrease of r_{CH_3CHO} at RH = 0% and T^{surf} = 25°C is given in Figure 7.16 for films at the two extremes of A_{001}. It is clearly visible that the randomly oriented films exhibited much higher deactivation.

The relative change in r_{CH_3CHO} throughout the experiment can be used as a quantitative descriptor of the catalyst deactivation. It is defined as:

$$\Delta r_{\mathrm{CH_3CHO}} = \frac{(r^{(3)}_{\mathrm{CH_3CHO}} - r^{(1)}_{\mathrm{CH_3CHO}})}{r^{(1)}_{\mathrm{CH_3CHO}}} \times 100\ [\%], \qquad (7.34)$$

where $r^{(1)}_{\mathrm{CH_3CHO}}$ and $r^{(3)}_{\mathrm{CH_3CHO}}$ are the rates observed during the first and the last of the three cycles, respectively. In Figure 7.16 the first cycle ends at approximately $t = 7$ min, and the last at $t = 38$ min.

The resulting $\Delta r_{\mathrm{CH_3CHO}}$ for the films with the two extreme values of A_{001} and the commercial Pilkington Active™ film, as a function of T^{surf} and RH are presented in Figure 7.17.

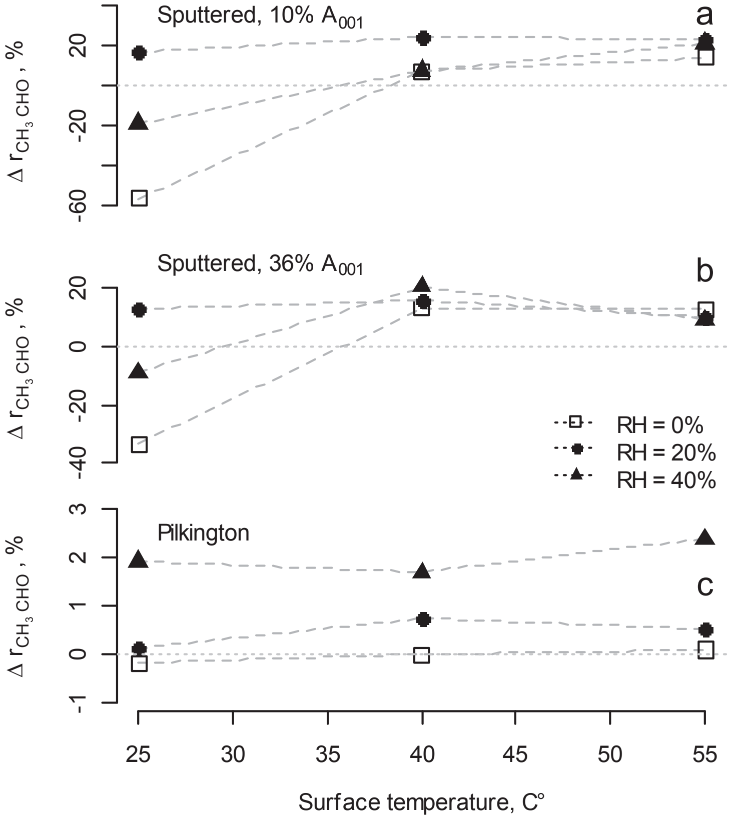

Figure 7.17: Change of the photocatalytic reaction rate, $\Delta r_{\mathrm{CH_3CHO}}$, through three successive UV illumination cycles, calculated for different T^{surf} and relative humidity (RH), for sputter deposited films with the lowest (a) and highest A_{001} (b), and for the commercial Pilkington Active™ film (c). Lines are drawn to guide the eye.

At RH = 0%, and T^{surf} = 25°C the deactivation was most pronounced in the film with the lowest preferential orientation, due to the higher contribution of less-reactive {101} facets on its surface. The commercial Pilkington

Active^{TM} film exhibited somehow lower deactivation. This can be related to its lower photocatalytic activity, resulting in smaller amounts of intermediates and reaction products. The lower crystallinity of this film would probably affect their binding to its surface as well.

At RH = 20% all samples showed reactivation, due to the enhanced photo-oxidation efficiency resulting from the photogeneration of reactive radical species. At RH = 40% de-activation was observed again in the sputtered samples, due to the inhibiting effects of the increasing water coverage. Upon rising T^{surf} re-activation was observed in all cases, due to enhanced desorption of reaction intermediates and surface water molecules.

7.3.3. Effect of surface temperature and relative humidity

A summary of $r_{\mathrm{CH_3CHO}}$ for both the sputtered TiO_2 films and the commercial Pilkington Active^{TM} film at all experimental conditions is listed in Table 7.8.

Table 7.8: Rate constant ($r_{\mathrm{CH_3CHO}}$) of CH_3CHO photo-oxidation for sputtered TiO_2 films with increasing A_{001}, and analogous data for the Pilkington ActiveTM commercial TiO_2 film. Data is given for different operational conditions (RH and surface temperature, T^{surf}).

$r_{\mathrm{CH_3CHO}}$, x 10^{-3} [μmol cm^{-2} min^{-1}]

	RH = 0			RH = 20%			RH = 40%		
A_{001}, %	25°C	40°C	55°C	25°C	40°C	55°C	25°C	40°C	55°C
10	0.954	1.073	1.297	1.669	1.912	2.084	1.694	1.765	1.954
15	0.826	0.933	1.081	1.87	2.052	2.173	1.741	1.792	1.948
22	0.921	0.995	1.162	2.114	2.207	2.277	2.115	2.032	2.108
31	1.404	1.52	1.66	1.548	1.705	1.809	1.388	1.618	1.698
36	1.831	1.936	2.028	1.897	2.017	2.078	1.542	1.766	1.847
Pilkington	0.014	0.014	0.015	0.012	0.019	0.023	0.016	0.031	0.051

The trends in Table 7.8 are also graphically summarized in Figure 7.18 for the two extreme cases of <001> orientation in sputtered films and the commercial film. The films with low A_{001} were found to significantly increase their activity at RH = 20%, while the activity of films with the highest degree of preferential <001> orientation remained almost unchanged. The commercial Pilkington Active^{TM} film exhibited two orders of magnitude smaller reaction rates under the same conditions, which can once again be attributed to its low crystallinity and less developed surface. In all cases, however, the effect of T^{surf} was beneficial for the steady-state reaction rates.

To quantify the effects of T^{surf} and RH on the films performance, two parameters describing the relative change in $r_{\mathrm{CH_3CHO}}$ at different operational conditions were calculated, similarly to the deactivation parameter, introduced in Section 7.3.2 ($\Delta r_{\mathrm{CH_3CHO}}$, eqn. 7.34). The first one is the change in $r_{\mathrm{CH_3CHO}}$ upon raising T^{surf} (eqn. 7.35).

$$\Delta r^{T}_{\mathrm{CH_3CHO}} = \frac{(r^{T}_{\mathrm{CH_3CHO}} - \mathrm{r}^{T=25°\mathrm{C}}_{\mathrm{CH_3CHO}})}{\mathrm{r}^{T=25°\mathrm{C}}_{\mathrm{CH_3CHO}}} \times 100 \ \ [\%], \qquad (7.35)$$

where $r^{T}_{\mathrm{CH_3CHO}}$ is the rate observed at the elevated temperature (T = 55°C), and $\mathrm{r}^{T=25°\mathrm{C}}_{\mathrm{CH_3CHO}}$ is the rate observed at T = 25°C.

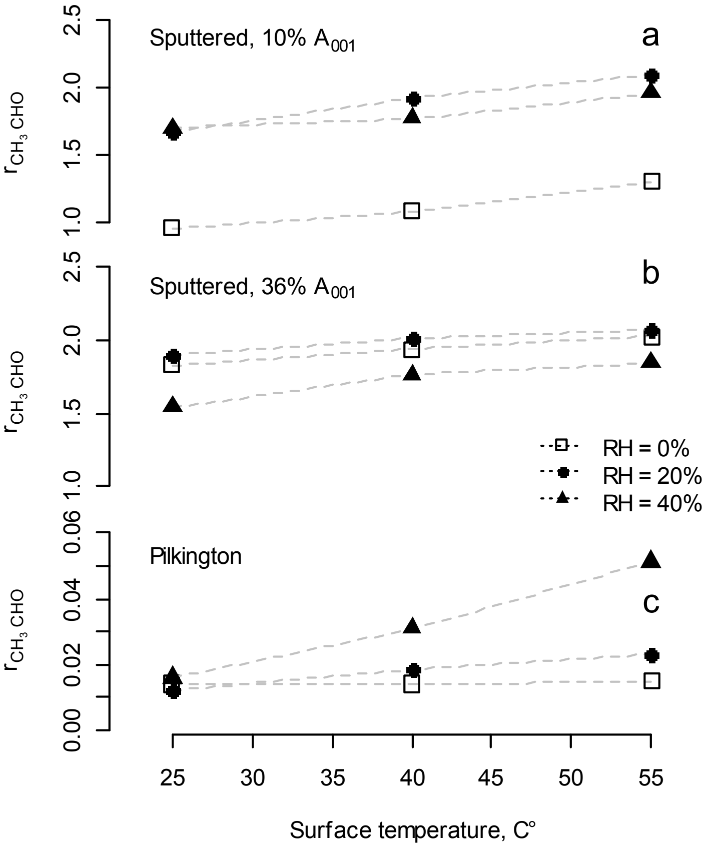

Figure 7.18: Trends in the effects of T^{surf} and RH on $r_{\mathrm{CH_3CHO}}$ for sputtered films with the shown degree of preferential orientation, and for the commercial Pilkington Active$^{\mathrm{TM}}$ sample. Lines are added to guide the eye. All reaction rates are in units of x 10^{-3} µmol cm^{-2} min^{-1}.

The second parameter describes the change in $r_{\mathrm{CH_3CHO}}$ with RH, compared to RH = 0% (which is the usual case in literature data).

It is defined as:

$$\Delta r_{\mathrm{CH_3CHO}}^{\mathrm{RH}} = \frac{(r_{\mathrm{CH_3CHO}}^{\mathrm{RH}} - r_{\mathrm{CH_3CHO}}^{\mathrm{RH=0\%}})}{r_{\mathrm{CH_3CHO}}^{\mathrm{RH=0\%}}} \times 100\ [\%], \tag{7.36}$$

where $r_{\mathrm{CH_3CHO}}^{\mathrm{RH}}$ is the rate at the elevated RH, and $r_{\mathrm{CH_3CHO}}^{\mathrm{RH=0\%}}$ is the rate at RH = 0. As in the case with eqn. 7.34, a positive value indicates enhancement in $r_{\mathrm{CH_3CHO}}$, while a negative value shows a decreased reaction rate. The results are summarized in Table 7.9. A few interesting trends are drawn from the data. First, as mentioned above, the samples with lower A_{001} exhibited much higher enhancement in $r_{\mathrm{CH_3CHO}}$ upon an increase of RH and T^{surf}. As their activity was systematically lower, the operational conditions turned out to be crucial in sustaining a good photocatalytic performance.

Table 7.9: Relative change in the photocatalytic reaction rate ($\Delta r_{\mathrm{CH_3CHO}}$) of CH_3CHO photo-oxidation over sputter-deposited TiO_2 films with different amounts of A_{001}, and for a commercial photocatalytic coating (Pilkington Active$^{\mathrm{TM}}$). Data summarized for $\Delta r_{\mathrm{CH_3CHO}}^{T}$ (7.35) at T^{surf} = 55°C (relative to 25°C) and for $r_{\mathrm{CH_3CHO}}^{\mathrm{RH}}$ (7.36) at two different RH values (relative to RH = 0%, and for T^{surf} = 25°C).

	$\Delta r_{\mathrm{CH_3CHO}}^{T=55°C}$, % (7.35)			$r_{\mathrm{CH_3CHO}}^{\mathrm{RH}}$, % (7.36) ($T^{surf}$ = 25°C)	
A_{001}, %	RH = 0%	RH = 20%	RH = 40%	RH = 20%	RH = 40%
10	36	25	15	75	78
15	31	16	12	126	111
22	26	8	0	129	130
31	18	17	22	10	-1
36	11	9	20	4	-16
Pilkington	9	90	215	-9	18

Another interesting effect is that at RH = 40% the enhancement with T^{surf} is similar for all sputtered samples regardless of A_{001}. The only exception was the film with A_{001} = 22%, which showed deviating results even in repeated measurements and is treated as an outlier.

This suggests that at high RH the intrinsic activity of the film is of minor importance. At this condition the water coverage is rate-determining, but its negative effects can be diminished by raising T^{surf}.

Apart from the sputtered samples, the most dramatic effect of T^{surf} was observed for the commercial Pilkington Active$^{\mathrm{TM}}$ film. For it the enhancement in $r_{\mathrm{CH_3CHO}}$ was over 200% at RH = 40% and T^{surf} = 55°C, underlining once again, that for catalysts with poor intrinsic activity the operational conditions are of prime importance.

Overall, the results for the sputtered samples show that there are multiple ways in which preferential <001> orientation improves the performance of the anatase TiO_2 photocatalyst: enhancing the overall reactivity, improving the long-term stability, and leading to stable performance over a wide range of operational conditions.

7.4. Synergistic effect of <001> preferential orientation and SO_4 – modification (unpublished results)

As discussed in Section 7.1.2 surface functionalization with SO_4 groups, improves the photocatalytic activity of TiO_2 films, by limiting the accumulation of surface intermediates. In Section 7.3.2 we showed that during the photo-oxidation of CH_3CHO the sputter-deposited TiO_2 films are deactivated, due to the accumulation of strongly bonded surface intermediates. In this section we will investigate the possibility to use SO_2 photofixation as means to restore and maintain the photocatalytic activity of sputtered TiO_2 films with preferential <001> orientation.

The samples used in the experiments were the same as in Section 7.3. They were split into two groups, and all were initially deactivated upon 45 min of CH_3CHO photo-oxidation, until a steady-state $r_{\mathrm{CH_3CHO}}$ was achieved. Following that they were treated for 1 h in a UV/O_3 photoreactor in an attempt to clean the surface from intermediates. After the treatment, the first group was used directly in CH_3CHO photo-oxidation experiments, while the second was firstly functionalized with SO_4 groups, according to the technique presented in Section 4.1.3. The deactivation and steady-state rates of two groups were then compared.

The photocatalytic experiments were conducted similarly to the procedure described in Section 5.3. However, T^{surf} was kept at 25°C and RH = 0%, in order to achieve maximum deactivation. The main difference was the duration of the UV illumination cycles, which were 3 × 15 min in Section 7.3. Here it was three 15 min cycles, followed by two 30 min cycles, resulting in a total reaction time of 105 min.

7.4.1. Effect of SO_4 – modification on the steady-state photo-oxidation rate and functional dependence on <001> orientation

The functional dependence $r_{\mathrm{CH_3CHO}}(A_{001})$ for pristine and SO_4 – modified sputtered TiO_2 films is presented in Figure 7.19, along with the resulting fits from the simplified two-facet kinetic model (eqn. 7.32). All data is for the steady-state $r_{\mathrm{CH_3CHO}}$, obtained after 105 min of CH_3CHO photo-oxidation.

The functional dependence of the pristine films remained similar after the deactivation, O_3 treatment, and a second deactivation. The reaction rate followed a cubic dependence of A_{001}. The main difference was that after the prolonged deactivation, $r_{\mathrm{CH_3CHO}}$ dropped dramatically. The results from the kinetic model show that both k_{101} and k_{001} decreased, as visible in Table 7.10. The less-reactive {101} facets, however showed a decrease in activity of about 80%, while the decrease for {001} was of about 45%, leading to the situation where the relative difference in reactivity between the two surfaces doubled, compared to the freshly deposited films.

The resulting kinetic parameters from fitting the data with eqn. 7.32 are summarized in Table 10. The sulfated TiO_2 films exhibited twice the reactivity of the ones, which were only regenerated with O_3. However, the surface modification changed the functional dependence on A_{001}. As visible in Table 7.10, a decrease was observed for the activity of {001}, while the one of {101} remained unchanged. This is consistent with theoretical prediction that SO_2 binds more strongly to {001} surfaces [92], and in line with the results in Section 7.1.2.6 on the effects of SO_4 – modification on the "fast" and "slow" pathways of CH_3CHO photo-oxidation on the TiO_2 surface. Clearly, the fast pathway is determined by the state of the {001} surfaces in TiO_2 films.

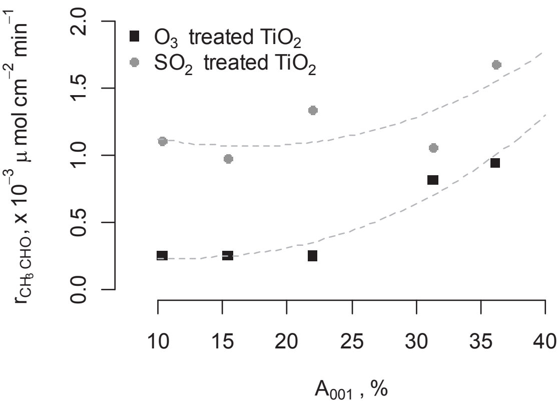

Figure 7.19: CH_3CHO photo-degradation rate, r_{CH_3CHO} , as a function of the exposed {001} area, A_{001} for films regenerated via UV/O_3 treatment and SO_2 – photofixation. The best fit according eqn. 7.32 is shown as a dashed line.

The SO_2 photofixation treatment results in an enhanced surface acidity, due to covalently bonded sulfate species, and prevents deactivation improving stability. However, it comes at the cost of losing active surface sites, which become occupied by surface-bound SO_4, preferentially on {001} surfaces.

Table 7.10: Resulting fitting parameters from the simplified surface kinetics model (eqn. 7.32) for the A_{001} dependent CH_3CHO photo-degradation rate, r_{CH_3CHO} , for pristine TiO_2 films before and after prolonged deactivation and UV/O_3 treatment, and for SO_4 – modified TiO_2 films.

Sample	Fitting parameters			k_{001}/k_{101}
	k_{101}	k_{001}	x	
Pristine TiO_2 films	1.245	13.531	3	11
O_3-treated pristine TiO_2 films	0.283	7.309	2.8	26
SO_4 - TiO_2 films	1.373	5.817	2.3	4

The other major effect was on the x parameter, which changed from a cubic dependence in the pristine TiO_2 films, to a quadratic dependence in the SO_4 – TiO2 films. As we discussed in Section 7.2.2, this parameter is expected to the energetics of CH_3CHO binding to the surface, and the photo-oxidation pathways through which it is channeled. Based on the findings, summarized in Section 7.1.2, where it was observed experimentally that desorption of CH_3CHO is possible on sulfated TiO_2, and crotonaldehyde no longer is an intermediate, it is not surprising to see that this affects $r_{\mathrm{CH_3CHO}}(A_{001})$ through a change of x, as these changes alter dramatically the overall photo-oxidation reaction pathways on the TiO_2 surface.

7.4.2. Effect of SO_4 – modification on deactivation of <001> orientated TiO_2 films.

In Section 7.1 it was observed that for SO_4 – modified TiO_2 the stability of the rate constant versus cycling the photocatalyst was enhanced in porous films of commercial catalyst. As we saw in the previous subsection, this also leads to higher rates for the sputter-deposited films. This is also reflected in their stability against deactivation. Figure 7.20 presents a comparison of $r_{\mathrm{CH_3CHO}}$ vs. time in four cases, corresponding to the films with lowest and highest A_{001}, with and without SO_4 – modification.

As discussed in Section 7.4.1 the unmodified films exhibited poorer activity in photocatalytic CH_3CHO oxidation, compared to the SO_4 – modified ones. The calculated $\Delta\, r_{\mathrm{CH_3CHO}}$ (eqn. 7.34) showed that they exhibited higher deactivation as well.

The result for the randomly oriented films ($A_{001} = 10\%$) were, as follows $\Delta\, r_{\mathrm{CH_3CHO}} = -20\%$ for a pristine film and $\Delta\, r_{\mathrm{CH_3CHO}} = -13\%$ for SO_4 – modified one. The sample with the highest orientation ($A_{001} = 36\%$) showed better stability against deactivation, in agreement with the conclusions drawn in Section 7.3.2, with $\Delta\, r_{\mathrm{CH_3CHO}} = -12\%$ for a pristine film and $\Delta\, r_{\mathrm{CH_3CHO}} = -1\%$ for the SO_4 – modified film.

This shows that the SO_4 – modification improves the photocatalytic performance of TiO_2 films, protecting them from deactivation regardless of their crystallographic orientation. However, it is clearly visible, that the synergistic effects of <001> preferential orientation and surface functionalization are highly beneficial in order to achieve maximal photocatalytic activity, combined with a high resistance against deactivation.

This makes the preferentially <001> oriented and SO_4 – modified TiO_2 films interesting for practical applications, especially in cases where deactivation can be a potential problem, as it is in gas-phase photocatalysis.

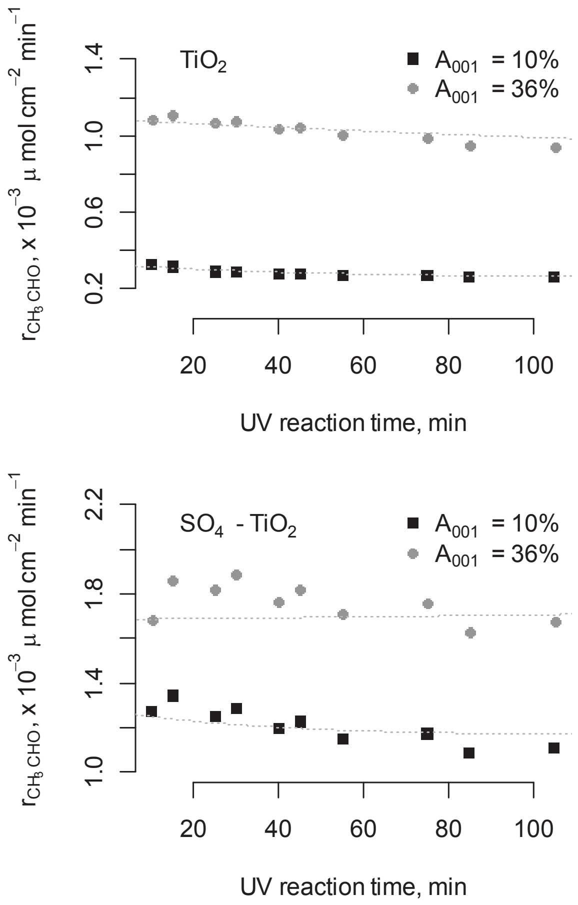

Figure 7.20: Decrease of $r_{\mathrm{CH_3CHO}}$ during UV illumination for a randomly oriented (A_{001} = 10%) and preferentially oriented (A_{001} = 36%) TiO_2 films with and without SO_4 surface treatment. The data from a total of five UV illumination cycles (3 × 15 + 2 × 30 min) is merged in this plot (the first 7 minutes of each cycle were omitted, in order to compensate for the gas sensor response time). RH = 0% and T^{surf} = 25°C. Lines are added to guide the eye.

8. Demonstrating photocatalysis for the general public

As it is demonstrated by the content of this thesis, TiO_2 photocatalysis is a promising and effective technique of solving a number of environmental problems. Unfortunately, it is a process largely unknown to society and not included in the high school curriculum in chemistry, nor physics. As scientists, it is our mission not only to work on important technologies, but to spread knowledge about them in the society. Hence, a large part of the time during my PhD studies was devoted to the popularization of science, and photocatalysis in particular.

In the past four years I have taken part in multiple popular science initiatives, such as science festivals (in Sweden, Finland and Bulgaria), popular science shows (in Bulgaria and the UK), conference educational sessions (in South Korea), and mass media events (predominantly in my country – Bulgaria). As a direct result of this, a large number of educational science demonstrations were developed treating different aspects of photocatalysis and indoor air quality. Some of them have resulted in publications in educational journals. A brief overview of the work, relevant to photocatalysis for indoor air treatment, is presented in this additional chapter which can be considered as an appendix.

8.1. Demonstrating gas-phase photocatalytic reactions using inexpensive semiconductor gas sensors (Paper VII)

It is straightforward to demonstrate photocatalysis in the liquid-phase. Usually an organic dye is added to a suspension of TiO_2 nanoparticles and a visual change is observed within 5 – 30 min upon UV- or sunlight illumination. As explained in Section 5.2, this approach is used in research as a standard method to determine photocatalytic performance. There are a number of "classroom ready" educational demonstrations based on this principle [141; 142; 143].

In contrast, tutorial demonstrations of photocatalysis in the gas-phase are challenging, as there is no visually observable change in the process, and advanced analytical equipment (such as GC, GC-MS or FTIR) is needed [144]. As such equipment is not readily available to educators; we proposed a design of gas-phase photocatalytic reactor based on an inexpensive SnO_2 gas sensor. A schematic overview of is presented in Figure 8.1.

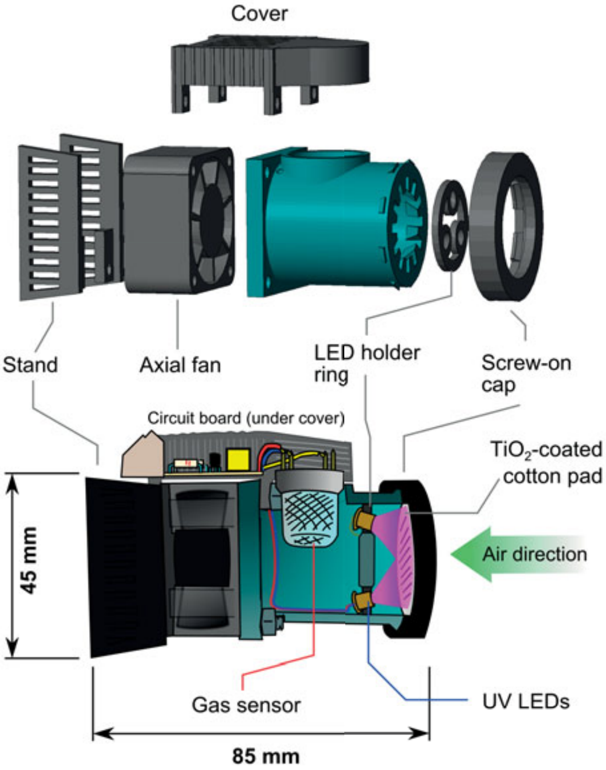

Figure 8.1: Schematic overview of the photocatalytic gas-phase reactor showing an exploded 3D view (top) and side-view cross-section (bottom).

The reactor body is in the form of a cylindrical air duct that is 3D - printed in poly-lactide (PLA) bioplastic. A cotton pad, impregnated with TiO_2 nanoparticles, serves as a photocatalytic filter and is attached to the air inlet and held in place with a screw-on plastic cap. A fan positioned at the opposite side is employed to drive an air flow through the reactor. Inside the 3D – printed reactor body a semiconductor gas sensor is placed (NAP-11AS, In_2O_3 air-quality sensor from Nemoto & Co., LTD, Japan), and a set of three UV LEDs with $\lambda = 365 \pm 18$ nm and 1.5 mW nominal optical output at 130° emission angle (Seoul Semiconductor, South Korea) is used to illuminate the photocatalytic filter. An Arduino microcontroller board is used to read the signal from the gas sensor via analogue – to – digital conversion, which is then sent to a host PC for plotting. The air flow can also be controlled by adjusting the speed of the fan by pulse – width – modulation.

The photocatalytic filter is prepared by impregnating a circular piece of cotton fabric (36 mm in diameter) using the approach schematically represented in Figure 8.2. The circular pads (1) are soaked and left overnight in 10 mL of distilled water, in which 1g of nanosized TiO_2 (Degussa P25 from Evonik Industries AG, Germany) is suspended. The pads are then dried (3) and thoroughly washed (4) and dried again, before being fastened onto the air inlet of the reactor (5).

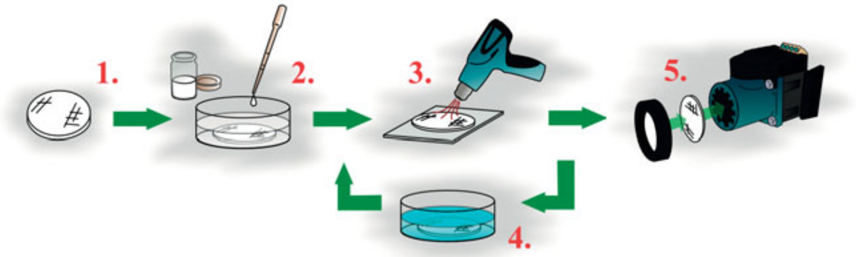

Figure 8.2: Preparation of the TiO_2 – impregnated cotton pads.

In this process the fibers comprising the cotton fabric get impregnated and covered with agglomerates of TiO_2 nanoparticles, forming the photocatalytic filter, as visible in the scanning electron microscopy images of the untreated and treated cloths shown in Figure 8.3.

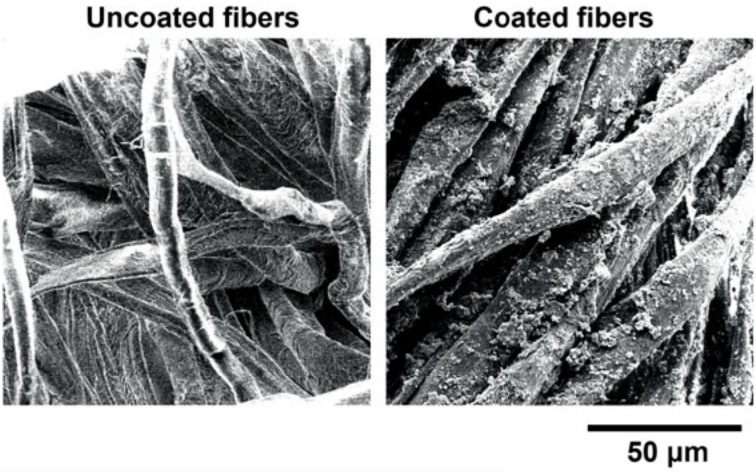

Figure 8.3: SEM images of cotton pad filters before (left) and after (right) the impregnation process described in Figure 8.2.

In the demonstration, shown schematically in Figure 8.4, two identical reactors are employed. The first is equipped with a TiO_2 – impregnated filter (Reactor 1), while the second is a used as a reference (Reactor 2), and equipped with an uncoated cotton pad. Ethanol vapor serves as a model gas-phase contaminant (a syringe is filled with the saturated vapors from a vial which contains small amount of ethanol). As shown in Figure 8.4 in the demonstration, the two reactors are placed in series, in two different configurations.

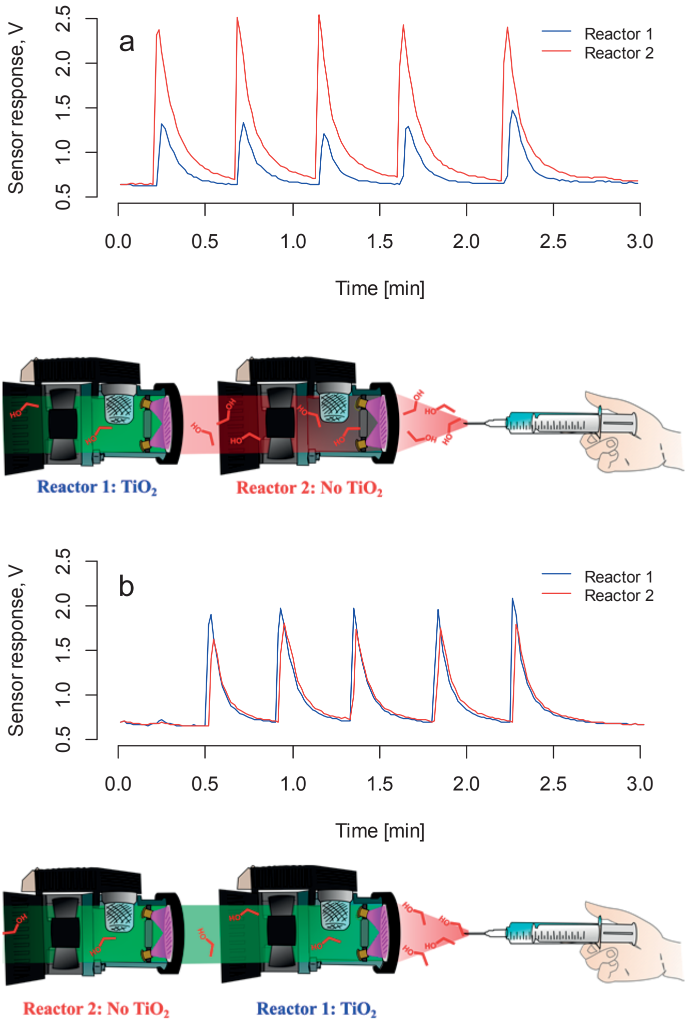

Figure 8.4: Reactor setups and measured online response as a function of time for two configurations: (a) Reactor 2 in front of Reactor 1, and (b) Reactor 1 in front of Reactor 2, clearly showing that the TiO_2 filter lowers the sensor signal (panel a) and that the reactor with no TiO_2 filter does not influence the signal (panel b).

In the first configuration the reference reactor (Reactor 2) is placed in front, and the TiO_2 filter is thus positioned between the two gas sensors. A strong difference in the signal is observed, as ethanol is consumed in the photocatalytic reaction, which is taking place in the filter between the two gas sensors. When the places of Reactor 1 and Reactor 2 are swapped, the TiO_2 filter is in front of both sensors, and a minute difference is observed.

More details are available in the appended Paper VII. The models of all structural parts, ready for 3D printing; detailed schematics; firmware and software; and detailed instructions for constructing the setup are provided by us both on our departmental web – page (http://www.ftf.teknik.uu.se), and as supporting information on the ACS web-page.

8.2. Demonstration of photocatalytic air cleaning by a TiO_2 – impregnated lampshade

In the course of my PhD I also had the opportunity to work on a small project involving a practical application of photocatalysis for indoor air cleaning. It was carried in cooperation with the Swedish company Butong AB, specializing in the production of lampshades and decorative elements made from concrete. A proposed modification involves concrete with additions of photocatalytic TiO_2 powder. Part of the work involved determination of the photocatalytic activity of TiO_2 – impregnated concrete lamps for gas-phase CH_3CHO photo oxidation. Figure 8.5 shows plots of CH_3CHO removal from the surface of three mixtures, compared with the activity of a commercial photocatalyst (Hombicat, Saschleben Chemie GmbH).

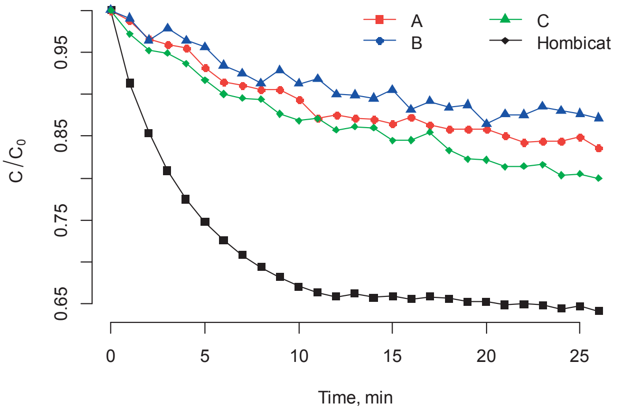

Figure 8.5: CH_3CHO removal by TiO_2 impregnated concrete (A – C), compared with a commercial photocatalyst. The exact composition of the mixtures is intellectual property of Butong AB, but TiO_2 was in the order of few percent, and increasing from A – C.

Data was obtained in a similar way as described in Section 5.1, but with the catalyst in the form of powder. Diffuse – reflectance measurements (DRIFTS) were employed and the plot represents the decrease in CH_3CHO coverage, as estimated by its carbonyl peak. The mortars exhibited good photocatalytic activity, considering their low TiO_2 content, which was in the order of few mass percent. The obtained rate constants were in the order of 1 x 10^{-2} min^{-1}, comparable to the 5 x 10^{-2} min^{-1} obtained from a commercial TiO_2 catalyst (100% TiO_2) by Hombicat, which is known for its high photocatalytic activity.

Part of the project included the design of a setup visually demonstrating indoor air cleaning for a presentation at the Stockholm Furniture Expo '15. The demonstration was based on one of their products. It was designed to be completely autonomous and capable of demonstrating the photocatalytic activity in way which is accessible to a general audience that is unfamiliar with the photocatalytic technology. The photocatalytic element was in the form of a cylinder (approx. 40 cm long and 12 cm in diameter), casted out of Butong AB's TiO_2 containing mortars. The resulting setup is shown in Figure 8.6.

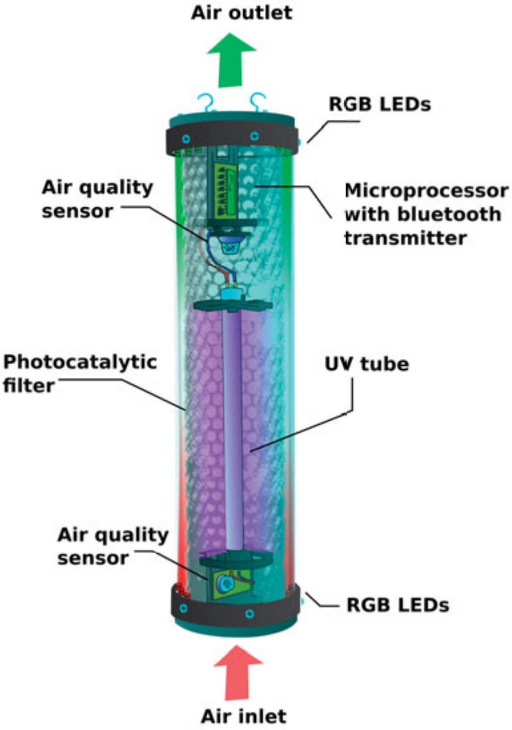

Figure 8.6: Schematic overview of the demonstration of photocatalytic air cleaning with a catalytic element of TiO_2 impregnated concrete, developed for the Stockholm Furniture Expo '15.

The lampshade was placed inside a 40 cm long tube, made of transparent polycarbonate, and both ends were sealed with 3D – printed caps, equipped with air inlets. A small fan was positioned on top, forcing the air to pass through the cylinder. Inside the photocatalytic element a 8W UV tube was placed. Two semiconductor gas sensors, identical with the one used in the educational demonstration, and described in the previous section were positioned at the air inlet and outlet, respectively. The signal from them was monitored in real time by an Arduino microcontroller. In order to convert the sensor signal into a visually perceivable change of gas concentration, rings of RGB LEDs were placed inside the plastic caps, illuminating the outside of the photocatalytic element. Depending on the signal measured in each sensor, the color of the LEDs was adjusted, ranging from blue, through green, yellow, orange and red, when the signal was ranging from small – to large. The absolute values of the signals were also transmitted by a Bluetooth connection to a PC for plotting.

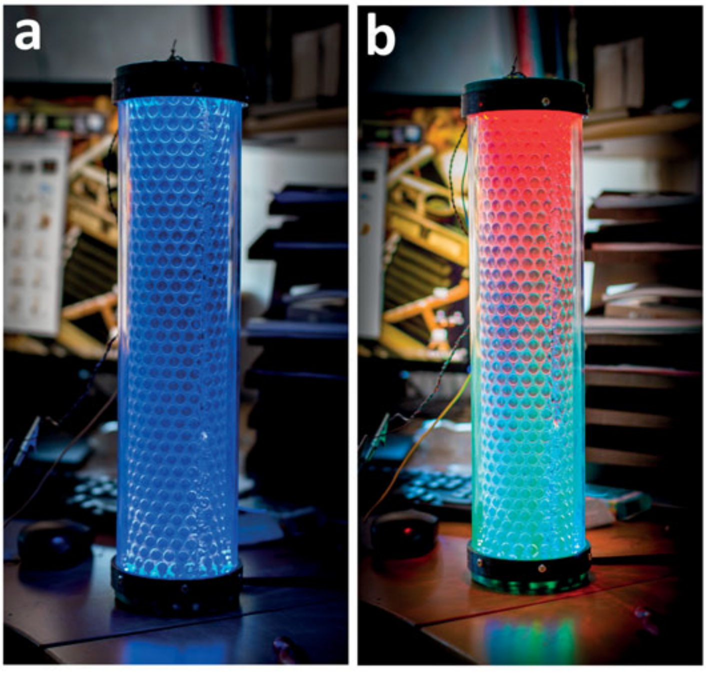

Figure 8.7: Observed color change in the setup presented in Figure 8.6. Both sides are illuminated in blue color when low concentrations of VOC are present (a), and as a color gradient during air cleaning, when a change in gas composition was measured (b).

8.3. Photocatalytic air cleaning window model

Another educational demo developed during the PhD project was a functioning photocatalytic air cleaning window based on TiO_2 – coated glass. The aim was to construct an autonomous setup allowing for online monitoring of not only the photocatalytic performance of a TiO_2 coated glass, but also its dependence on relevant environmental parameters. This type of demo can be employed in university courses exemplifying engineering aspects of photocatalytic coatings in the built environment, as well as to stakeholders in the building sector. A schematic overview of the setup is presented in Figure 8.8.

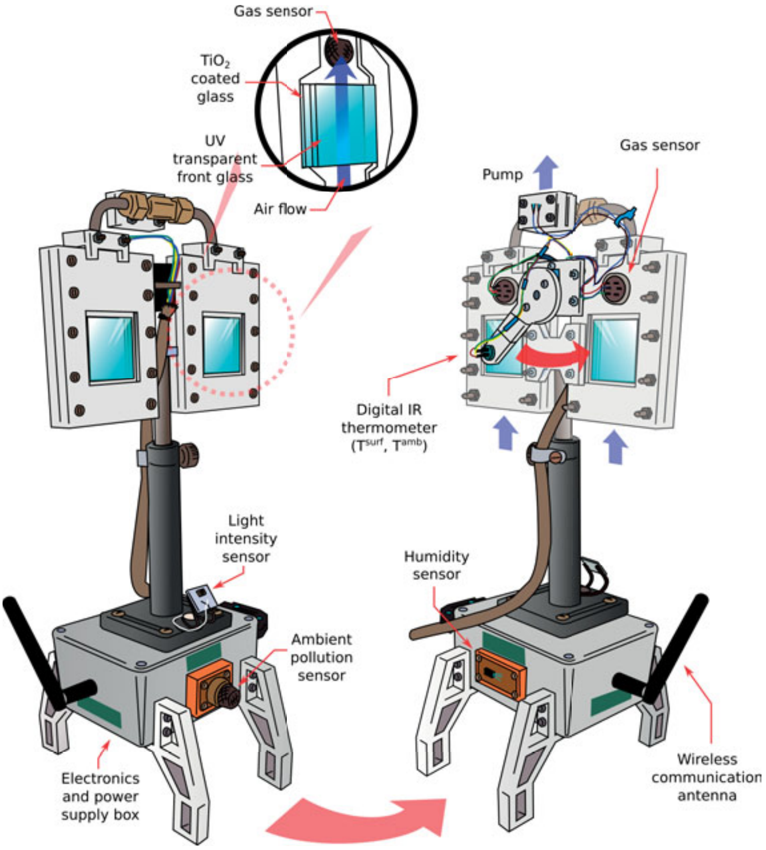

Figure 8.8: Schematic overview of the photocatalytic air cleaning window model. The major components are labelled.

The setup is built around an Arduino microcontroller board, equipped with a 2.4 GHz radio transceiver module, allowing for 300 m communication range with a host PC. The electronics are contained in an aluminum enclosure, which is equipped with plastic legs and serves as structural support of the photocatalytic module. The latter has two identical photocatalytic reaction window cells, each of them equipped with a 50 × 50 mm TiO_2 coated glass substrate and a UV-transparent front window. One of the window cells can be equipped with an uncoated glass, and used for reference measurements, or both can be used in tandem in comparison studies. The air flow through the reaction cells is controlled by a miniature radial fan. The setup is equipped with sensors that monitor: incident light intensity, relative humidity, air quality before, and after the reaction cells, and surface temperature of the TiO_2 coated glass slide.

In one experiment the setup was placed at a window in the common kitchen at the Division of Solid State Physics of The Ångström lab. It unfortunately is equipped with Solar-control glass windows, which limited the UV photon flux. Measurements with a radiometer, equipped with a 360 nm wideband UV filter, showed that on a sunny day the UV illumination measured outside is 3 mW cm^{-2}, while behind the window it was less than 0.5 mW cm^{-2}. Nevertheless some interesting results were still obtained.

Figure 8.9 shows a plot of the response in the ambient gas sensor, during a 24h period. The ambient gas sensor does not discriminate between different VOCs, so the plot in Figure 8.9 shows just the trends in the total VOC content throughout the day. It is clearly visible that higher levels are related to human presence and activities.

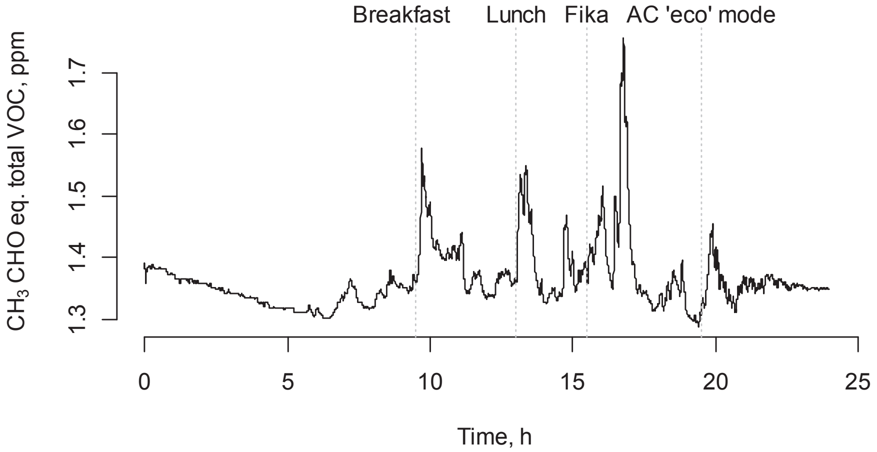

Figure 8.9: Changes in ambient VOC concentration levels in the common kitchen of the Solid State Physics division. Major peaks in air contamination correspond to daily activities in the kitchen. The signal from the ambient air quality sensor was converted into units of equivalent CH_3CHO concentration using calibration data from the setup described in Section 5.3. AC eco-mode indicates the energy saving mode of the Ångström Laboratory ventilation system.

The first peak is observed around 9:30 AM, during the morning coffee break, followed by another one at 1:30 PM, during the lunch break. The highest VOCs levels are measured during the afternoon "fika", that traditionally takes place in Swedish offices at precisely 3:30PM. It is also observed that during the night, the baseline levels are higher, compared to during the day. This is due to the energy-saving "eco" that Ångström's ventilation system is switched to after 7:30 PM. Then the slight increase in the VOC level comes from the composting bins in the shared kitchen

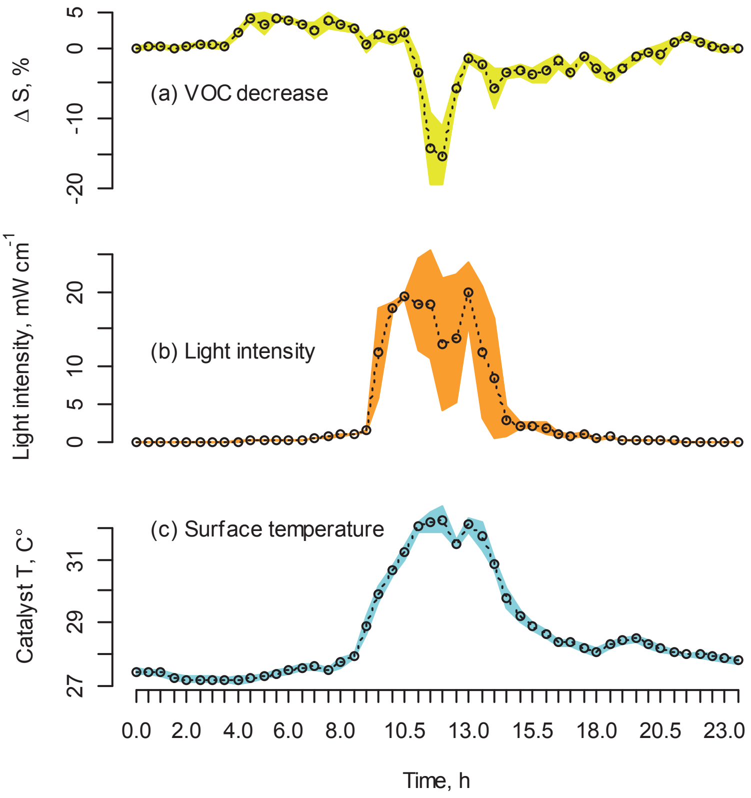

Figure 8.10: Relative difference between the signal measured in the ambient air quality sensor, and the signal measured after the TiO_2 coated glass in the setup described in Figure 8.8. The highest decrease in the VOC levels coincides with the highest solar illumination intensity.

In Figure 8.10a the relative difference between the ambient sensor and the sensor in one of the window reaction cells, equipped with a TiO_2 coated glass is plotted. A negative value shows a decrease of the VOC levels in the exhaust after the TiO_2 coating, and the highest difference correlates very well with the plot in Figure 8.10b, which represents the incident light intensity during the same period (which in turn is proportional to the temperature of the glass in the window cell, plotted in Figure 8.10c).

9. Conclusions

The overall aim of this PhD thesis was to investigate some innovative strategies to improve the performance of anatase TiO_2 films in indoor air cleaning applications. A number of interesting results were obtained. These included mechanistic details about the interaction between CH_3CHO and TiO_2 films, as well as SO_4 functionalized TiO_2 films. The importance of TiO_2 film growth and the role of crystal orientation and exposed crystal surfaces were also investigated. Finally, the influence of reaction conditions, such as relative humidity, catalyst temperature, and light intensity on the photocatalytic activity of TiO_2 films was also considered.

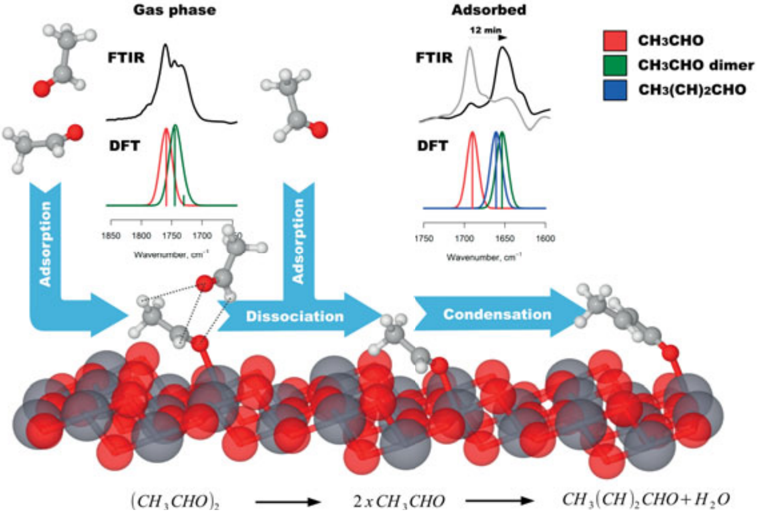

Figure 9.1: Mechanism of adsorption of CH_3CHO and its dimeric structure onto the TiO_2 {101} surface and condensation to form crotonaldehyde. The insets show a comparison of experimentally observed FTIR spectra and the vibrational frequencies for the respective structures, as predicted by DFT calculations.

Focusing on acetaldehyde, which is an important indoor air pollutant and at the same time a suitable model contaminant, detailed results for its adsorption and condensation are presented. By means of *in situ* FTIR, complemented by DFT calculations, a hitherto unknown dimeric acetaldehyde surface species, associated with a vibrational band at 1643 cm^{-1}, was identified on the anatase TiO_2 surface. It was found that this species influences the condensation reaction of acetaldehyde, and acts as a source of acetaldehyde at later reaction steps, as illustrated in Figure 9.1.

Furthermore we have elucidated the effect of surface SO_4 groups on the adsorption and photo-oxidation of CH_3CHO. The surface sulfation was found to prevent the formation of condensation products (crotonaldehyde) and to preserve the long-term photocatalytic activity of TiO_2, which is otherwise inhibited due to accumulation of intermediates.

In all cases we observed that two types of surface active sites, exhibiting different activities are present, and devised a model to estimate their contribution to the total activity of the photocatalyst. It was found that upon cycling the catalyst, the relative contribution from the sites with higher activity decreases.

Having elucidated elementary reaction steps for photocatalytic oxidation of CH_3CHO on porous TiO_2 and sulfate modified TiO_2 films, further studies were made on TiO_2 thin films prepared by DC magnetron sputtering. These have suitable optical and mechanical properties for use in the proposed "photocatalytic" air cleaning window concept. In the course of optimizing the sputtering process a way to fine control the preferential <001> orientation in sputtered TiO_2 films was discovered.

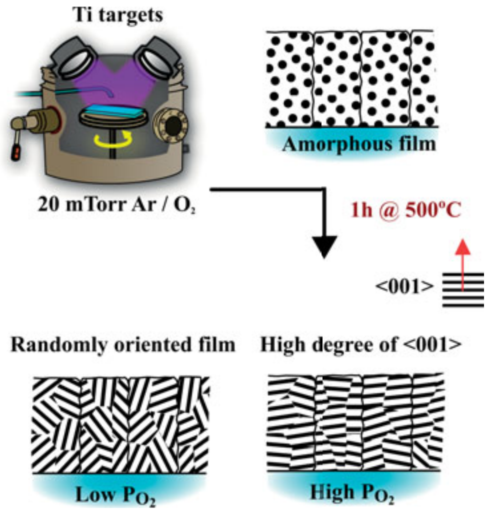

Figure 9.2: Altering the partial O_2 pressure during the sputter - deposition of TiO_2 allows fine control over the preferential <001> orientation and relative abundance of {001} facets on the surface.

As shown in Figure 9.2 it was found that the partial O_2 pressure during film deposition can be used to increase the preferential <001> orientation and the relative abundance of {001} facets up to four times compared to randomly oriented anatase TiO_2 films. To our knowledge this work represents the first systematic study on the effect of preferential <001> orientation for the photocatalytic activity of TiO_2 photocatalysts. We found that preferentially <001> orientation is highly beneficial for the photocatalytic activity of TiO_2 films, due to the following reasons:

1. The intrinsic activity of the surface-exposed {001} facets is about one order higher than that of {101} facets. This was confirmed independently by two different approaches: liquid-phase methylene blue and gas-phase CH_3CHO photo-oxidation (Figure 9.3a).
2. Films with preferential <001> orientation can utilize light much more effectively for photocatalysis, as shown by the intensity dependence of the measured rate constants for methylene blue photo – oxidation.

The functional dependence of the relative {001} facet abundance on the photocatalytic activity is non-linear and follows either a quadratic (liquid-phase photo-oxidation) or a cubic (gas-phase) dependence. The relative difference in facet reactivity of the fresh catalyst was preserved in all cases; hence we conclude that the non-linearity is determined by reaction mechanisms and specific for the given reaction conditions and substrate molecule.

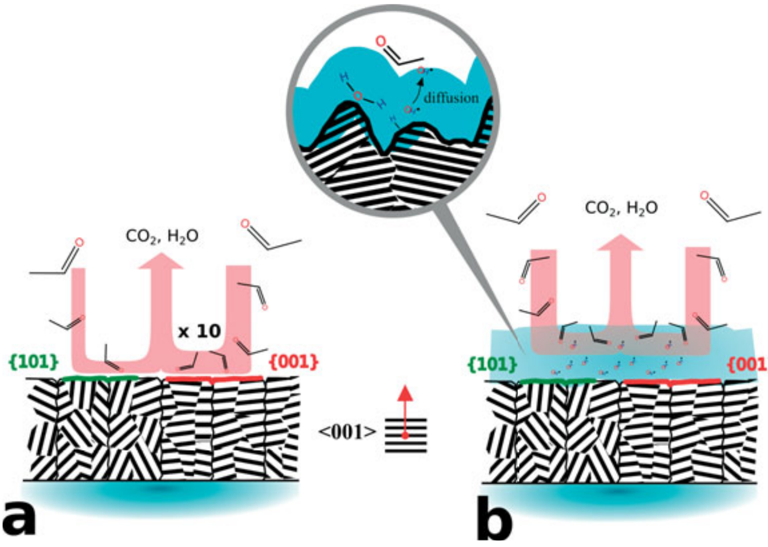

Figure 9.3: In liquid-phase and “dry” gas-phase experiments the {001} facets exhibit an order of magnitude higher activity in photocatalytic reactions, compared to the {101} facets (a). In the presence of humidity, however, the photocatalytic activity is determined by the formation of OH radicals and their ability to diffuse through the surface water layer (b).

In the gas-phase, when water is present in the reaction environment, the intrinsic activity of the photocatalyst is altered, and an enhanced photocatalytic activity is observed, possibly due to the generation of active radical species by the catalyst. At high RH the beneficial effects of surface water are diminished due to an increasing water coverage, which has the effect of creating a diffusion barrier for radicals and reactants (Figure 9.3b). It is demonstrated that this negative effect of RH can be remediated by heating the surface of the catalyst, which desorbs excess water and at the same time has the additional beneficial effect of promoting surface reaction kinetics.

We found that the above-mentioned processes are especially advantageous in samples with low intrinsic photocatalytic activity, which can result from a poor crystallinity, undeveloped surface area, or a small fraction of highly reactive facets exposed on the surface. This was the case for the commercial Pilkington Active^{TM} film, but the last point is valid for most TiO_2 materials where crystal growth is dictated by thermodynamics.

Our results clearly demonstrate that a high degree of preferential <001> orientation leads to both higher reactivity for two common model pollutants, and much more stable photocatalytic activity over a wide range of operational conditions. Finally, the combined beneficial effects of surface SO_4 – functionalization and preferential orientation can be utilized in order to prepare highly active anatase TiO_2 films with excellent long-term stability against deactivation.

10. Summary in Swedish: Fotokatalytiska tunna filmer av TiO_2 för luftrening

Dålig kvalitet på inomhusluften är en viktig källa till ohälsa. Det så kallade "sjuka hus-syndromet" erkändes av Världshälsoorganisationen (WHO) i mitten av 1980-talet som en orsak till ohälsa och förknippas med dålig ventilation som leder till ackumulering av föroreningar i inomhusluften. Flyktiga organiska föreningar, såsom formaldehyd och acetaldehyd, är en viktig klass av kemiska substanser som bidrar till luftföroreningar inomhus. Flera källor i inomhusmiljön bidrar till dessa kemikalier, såsom syntetiska byggmaterial, möbler, rökning inomhus och diverse hushållskemikalier.

Det finns flera befintliga metoder att förbättra inomhusluftskvaliteten, t.ex. mekaniska filter, absorbentmaterial, förbättrad ventilation, eller ozon – och – UV – behandling av luften. Dessa dock kan vara väldigt kostsamma och kräva mycket energi, samt kräver frekvent regenerering, rengöring eller utbyte (t.ex. absorbenter, mekaniska filter).

En annan lovande metod för att upprätthålla god luftkvalitet är användning av beläggningar av titandioxid (TiO_2) som i kombination med lämplig belysning kan fungera underhållsfritt. Dessa TiO_2 kan beläggas på fönsterrutor eller väggar. Luftreningen bygger i dessa beläggningar bygger på fotokatalys. I fotokatalys absorberar katalysatorn energi i form av ljus och initierar kemiska reaktioner, såsom fotooxidation eller fotoreduktion av molekyler, som direkt eller indirekt kan bryta ned organiska föreningar till enbart vatten och koldioxid. Vid sådana tillämpningar är det viktigt att säkerställa stabil fotokatalytisk aktivitet för ett brett spann av driftförhållanden, såsom relativ fuktighet och temperatur. Det är också viktigt att undvika deaktivering av katalysatorn.

I den här avhandlingen undersöks den fotokatalytiska nedbrytningen av föroreningen acetaldehyd (CH_3CHO) med hjälp av nanostrukturerade tunna filmer av TiO_2. Nya metoder för att förbättra den fotokatalytiska aktiviteten hos sådana filmer genom olika typer av modifiering förslås. T.ex. kovalent bindning av sulfatgrupper (SO_4) till TiO_2, vilka förändrar ytsurheten och gör katalysatorn mer beständig för deaktivering. Dessutom kan filmernas totala fotokatalytiska aktivitet också förbättras genom att öka andelen exponerade reaktiva {001} facetter i de nanokristallina TiO_2 filmerna. I den anatasa fasen av TiO_2 domineras ytan på partiklarna av {101} ytor som här lägre fotokatalytisk aktivitet.

I den första delen av avhandlingen används *in situ* FTIR spektroskopi för att studera adsorption och fotokatalytisk nedbrytning av CH_3CHO på TiO_2 och SO_4 – modifierade TiO_2 – ytor. Ytkoncentrationer av huvudprodukter och motsvarande reaktionshastigheter bestäms. På TiO_2 – ytan kondenserar acetaldehyd omedelbart till krotonaldehyd (CH_3CH_2CHO) genom aldolkondensation. På det sättet blir krotonaldehyd startpunkten i fotooxidationsreaktionen, vilket inte är fördelaktigt eftersom krotonaldehyd är svårare att oxidera på grund av sin högre molekylvikt (fler kolatomer och därmed fler reaktionssteg).

Nedbrytning av krotonaldehyd resulterar huvudsakligen i ytbundet format vilket binder hårt till TiO_2 och därmed blockerar adsorptionssäten, dvs. deaktiverar katalysatorn. Vi visar att oxidationsreaktionen för krotonaldehyd beskrivs av två reaktionsvägar vilka är förknippade med två typer av aktiva säten. Det visar sig att de mer aktiva sätena blockeras snabbt och att deras relativa andel minskar när katalysatorn används flera gånger i upprepade oxidationscykler. Vi visar vidare att på SO_4 – modifierad TiO_2 ackumuleras färre reaktionsprodukter genom att sura säten binder svagare till oxidationsprodukterna vilket gör att katalysatorn motstår deaktivering bättre än ren TiO_2. Dessutom förhindrar sulfatgrupperna aldolreaktionen och därmed bildas inga kondensationsprodukter på svavelhaltiga filmer. Genom en kombination av FTIR spektroskopi och DFT beräkningar har en hittills okänd ytförening identifierats – en ytbunden acetaldehyddimer med ett adsorptionsband vid 1643 cm^{-1}. Denna dimer kan förvandlas till acetaldehyd i senare reaktionssteg.

Den andra delen av avhandlingen behandlar effekten av <001> – orientering på den fotokatalytiska aktiviteten hos anatas TiO_2 – filmer tillverkade med hjälp av katodförstoftning (eng. magnetron sputtering). Genom reglering av det partiella syretrycket i deponeringskammaren kan <001> – orienteringen i filmerna kontrolleras, vilket leder till en direkt kontroll av andelen exponerade {001} – kristallografiska fasetter. En positiv fotokatalytisk effekt observerades både för nedbrytning av metylenblått i vattenlösning, och gasfas CH_3CHO. I båda fallen var filmerna med högsta andelen {001} ytor upp till dubbelt så reaktiva än de med en slumpmässig orientering. Vi visar att den relativa aktiviteten hos {001} – ytor i fotokatalytiska reaktioner är minst 10 ggr högre jämfört med {101} – ytor. Vidare visas att de orienterade filmerna är mer motståndskraftiga gentemot deaktivering. De uppvisar nästan oförändrad aktivitet under olika reaktionsbetingelser, såsom olika luftfuktighet och yttemperatur. Slutligen påvisas även en synergistisk effekt av SO_4 – funktionalisering och hög andel exponerade {001} – ytor.

De resultat som presenteras i avhandlingen på TiO_2 filmer med modifierade kristallografiska och kemiska egenskaper kan finna viktiga tillämpningsområden i den byggda miljön som nya beläggningar för rening av inomhusluft och självrengörande ytor.

11. Summary in Bulgarian: Фотокаталитични тънки филми от TiO_2 за пречистване на въздух

Лошото качество на въздуха може да доведе до негативни последици за здравето. Т.нар. "синдром на болната сграда" е бил разпознат за пръв път от Световната здравна организация (СЗО) още през средата на 80 – те години на миналия век. Той се причинява от неефективна вентилация в жилищните и офис сгради, което може да доведе до натрупването на замърсители във въздуха. Такива замърсители са например летливите органични съединения, представители които са съединенията формалдехид и ацеталдехид. Те се отделят от различни източници: например синтетичните материали и текстили, използвани в строителството и производството на мебели, тютюнопушенето на закрито, или пък битовата химия.

Качеството на въздуха може да бъде подобрено с по-ефективна вентилация, употребата на еднократни абсорбиращи филтри или третиранете му с озон и ултравиолетова светлина. Тези методи, обаче изискват инвестиции и съществен разход на енергия. За щастие в последно време се работи върху нова и обещаваща технология за пречистване на въздух, базирана на активни покрития от титанов диоксид (TiO_2). Такива покрития могат да бъдат отложени върху големи и добре осветени повърхности, като например стени и прозоръчни стъклопакети. На тези места активните покрития могат да намалят количеството замърсители на въздуха, отстранявайки ги чрез фотокатализ. Във фотокатализа катализаторът поглъща енергия под формата на светлина и я използва за иницииране на фотохимични процеси – например на фотоокисление и фоторедукция. Чрез тези процеси органичните замърсители могат да бъдат напълно разградени до вода и въглероден диоксид.

При прилагането на покрития от TiO_2 е важно да се вземат мерки за осигуряването на устойчива фотокаталитична активност в широк диапазон условия на околната среда (например относителна влажност и температура). Освен това трябва да бъде ограничена деактивацията на фотокатализатора, която се причинява от натрупване на междинни съединения на повърхността му.

В настоящата дисертация е изследвано фотокаталитичното разлагане на замърсителя ацеталдехид (CH_3CHO) с помощта на наноструктурирани тънки филми от TiO_2. Предложени са нови методи за подобряване на фотокаталитичната активност на такива тънки филми. Например, чрез ковалентно свързване на сулфатни групи (SO_4) към повърхността на фотокатализатора може да бъде повишена нейната киселинност. Това от своя страна намалява афинитета на междинните съединения към повърхността, ограничава тяхното натрупване и възпрепятства деакцивацията на катализатора. Освен това цялостната фотокаталитична активност на филмите може да бъде подобрена, чрез повишаване на относителния дял на изложените на повърхността силно реактивни {001} кристалографски фасети. Важно е да се отбележи, че при наночастиците на анатазната модификация на TiO_2 повърхността обикновено бива доминирана от по-слабо реактивните {101} фасети.

В първата част на дисертацията е изследван механизмът на адсорбция и фотокаталитично разлагане на CH_3CHO от TiO_2 и SO_4 функционализиран TiO_2. Протичащите на повърхността процеси са изследвани с инфрачервена спектроскопия (FTIR). Установени са структурите на адсорбираните молекули, тяхната концентрация и цялостната кинетика на фотоокисление.

На повърхността на TiO_2 ацеталдехидът претърпява реакция на алдолна кондензация, при която се превръща в кротоналдехид (CH_3CH_2CHO). Поради този процес първата реакционна стъпка при фотокаталитичното окисление е разграждане на натрупалия се кротоналдехид. Това е нежелано, тъй като кротоналдехидът има по-голяма молекулна маса, съответно се изисква по-голям брой стъпки, за да бъде разграден напълно. Основен междинен продукт при разграждането на кротоналдехид са форматните йони. Те се свързват здраво към повърхността на фотокатализатора, под формата на няколко изключително стабилни структури и затрудняват по-нататъшните реакционни стъпки. Тяхното натрупване води и до деактивацията на TiO_2, поради блокиране на активни центрове.

Самото фотокаталитично окисление преминава през два различни реакционни канала. Причина за това е наличието на активни центрове с различна активност. Бе установено, че относителният дял на по-високо реактивните центрове намалява, когато фотокатализаторът е подложен на няколко последователни реакционни цикъла.

На повърхността на SO_4 – модифицираният TiO_2 не се наблюдава натрупването на междинни продукти и се оказа, че той устоява на процесите на деактивация по-добре, от колкото немодифицираният фотокатализатор. Освен това наличието на сулфатни групи предотвратява нежеланата алдолна кондензация между молекулите ацеталдехид.

С помощта на комбинация от спектроскопски данни и квантово-химични изчисления с DFT бе открита и непозната досега структура на адсорбиран към TiO_2 ацеталдехид. А именно, под формата на свързан с повърхността димер, наличието на който води до появата на абсорбционна линия при 1643 $см^{-1}$ на ИЧ спектри. Въпросният димер може да се превърне в източник на ацеталдехид при по-нататъшни реакционни стъпки.

Втората част от дисертацията засяга ефектите на преференциална <001> кристалографска ориентация във филми от TiO_2, отложени чрез магнетронно разпрашаване. Открито бе, че при промяна на парциалното налягане на кислорода по време на отлагането на тези филми, се постига прецизен контрол върху преференциалната ориентация. Този ефект позволява отлагането на тънки филми TiO_2 с предопределено съотношение между площите на {001} и {101} кристалографски фасети на повърхността.

При филми с по-висок принос от силно реактивните {001} фасети се наблюдава повишена фотокаталитична активност както при фотокаталитичното окисление на Метиленово синьо в течна фаза, така и при това на CH_3CHO в газова фаза. И в двата случая увеличаването на относителната площ на {001} четири пъти води до двойно по-висока фотокаталитична активност. С помощта на специално разработен за целта кинетичен модел бе установено, че фотокаталитичната активност при {001} е един порядък по-висока от тази при {101} повърхностите. Освен това преференциално ориентираните TiO_2 филми са не само по-устойчиви спрямо деактивация, но и запазват високата си фотокаталитична активност при промяна на реакционни параметри, като например относителна влажност на газовата фаза и температура на повърхността.

Особено висока и устойчива фотокаталитна активност бе наблюдавана при филми, които са не само преференциално ориентирани, но и SO_4 – модифицирани. Синергичните ефекти от двете модификации правят тези филми подходящи за употреба като прозоръчни покрития за пречистване на въздух.

Представените в дисертацията резултати са от съществена важност за прилагане на тънки филми от TiO_2 в приложения за пречистване на въздух и като самопочистващи се покрития.

Acknowledgements

The PhD project was funded by the European Research Council, under the European Community's Seventh Framework Program (FP7 / 2007 – 2013) / ERC Grant Agreement No. 267234 ("GRINDOOR"). Financial support for some of the experimental work was received from the Swedish Research Council (Grant No. VR – 2010 – 3514). The author is also thankful for the computational resources, provided by the Swedish National Infrastructure for Computing (SNIC) through Uppsala Multidisciplinary Centre for Advanced Computational Science (UPPMAX) under project p2012120.

Writing this thesis was a pleasurable task and I am proud of the results that were accomplished during the four years of my doctoral project. These results would not have been obtained without the guidance of my supervisor **Prof. Lars Österlund**, whom I would like to thank first and foremost. Under his supervision I always felt encouraged to develop my ideas. It was a pleasure to work together and I do believe we did manage to achieve a lot for a PhD project, especially in the competitive field of photocatalysis. I am also deeply grateful to my co-supervisors, **Prof. Gunnar Niklassons** and **Prof. Claes-Göran Granqvist**, for all of the fruitful discussions we have had over the past years, and for helping me turn our findings into credible scientific results. *Stort tack!*

I am thankful to **Dr. Zareh Topalian**, who was a post-doctoral fellow at our group when I began my PhD studies and whose work has inspired a lot of my own research.

Very special thanks should also go to **Emma Kay** and **William Jones** for helping me proofread a large deal of the ~150 pages preceding this one.

I will always associate working at the Division of Solid State Physics with good memories and a very warm environment. I am very happy that I had the honor of sharing my workplace with so many wonderful colleagues. Among them I must personally mention **Delphine Lebrun**, who is not just a colleague, but also a true friend; **Umut Cindemir**, who had to endure my entropy-enhancing effects on our shared office; **Andreas Mattsson** and **Bengt Götesson**, for the technical support during the years; **Shuyi Li**, for being herself, and all the Chinese tea I got from her family; the other ”green” students, **Ruitao Wen** and **Yuxia Ji**; **Annica Nilsson**, for helping me tame the Lambda 900; and **Joakim Widén**, for the beer therapy during the tense weeks of writing.

Some unpublished results from this PhD project also proved the hypothesis that there is life outside the lab. I was really fortunate to make a lot of friends in Uppsala. Among them are my best friend **Andrés;** and **João**, **Cédric** and **Mário**. *Guys, thank you for sharing all of those memories, adventures, and travels with me!*

Living abroad can be difficult, but Uppsala never felt any different than home, thanks to my Bulgarian gang: **Darina**, **Ioanna**, **Dorothea**, **Vassil**, **Pavel**, **Sandra**, **Roumen** and **Radostina**. *Наздраве, приятели!*

The last few words are dedicated to some special people (in Bulgarian):

Казват, че съдбата се пише *когато*, а не *преди* нещо да се случи. Дори и така да е, *преди* да се стигне до тук своята роля изиграха няколко важни за мен хора. Това са: **г-жа Илиана Пецанова**, която първа ме насочи към науката; преподавателите ми във Факултета по химия и фармация към СУ, в частност **доц. Цецо Душкин** (1958 – 2011) и **проф. д.х.н. Тони Спасов**, които не само ми предоставиха здравата основа, на която да стъпя, но ме и насърчиха да продължа кариерата си като учен; и невероятната **Любов Костова**, която макар и хуманист по душа е най-големият фен на науката в България и ми показа не само, че да си учен е „*наистина, ама наистина готино*", но и колко е важно да бъдеш себе си.

И накрая, но най-важно, искам да благодаря на семейството си. На това в Швеция, **Милена** и **Ливио**, които ме приютиха в дома си и ми помогнаха толкова много през първите трудни месеци.

И на родителите си – *Мамо, татко, не мога да намеря думите, с които да ви благодаря за жертвите, които направихте за да получа добро начало. Обичам ви!*

Bibliography

[1] J.A. Leech, W.C. Nelson, R.T. Burnett, S. Aaron, M.E. Raizenne, *J. Exposure Anal. Environ. Epidemiol.* **12** (2002) 427 – 432.

[2] "Strategic approaches to indoor air policy-making.", World Health Organization (Bilthoven, 1999).

[3] J. Sundell, *Indoor air* **4** (1994) 7 – 49.

[4] "Indoor air quality research. EURO Rep Stud 103", World Health Organization (1986).

[5] "Indoor Air Pollutants: Exposure and Health Effects. EURO Reports and Studies, No. 78", World Health Organization (Copenhagen, 1983).

[6] R.J. Laumbach, *International Encyclopedia of Public Health*. (2008).

[7] The Lancet Oncology online, Thursday Oct 24th. 2013.

[8] "Indoor Air Quality: Organic Pollutants. EURO Reports and Studies No. 111.", World Health Organization (Copenhagen, 1989).

[9] "Overall evaluations of carcinogenicity to humans, acetaldehyde [75-07-0] (Vol. 71, 1999) and formaldehyde [50-00-0] (Vol. 88, 2004). The IARC Monographs Series.", International Agency for Research on Cancer (IARC).

[10] W.W. Nazaroff, C.J. Weschler, *Atmos. Environ.* **38** (2004) 2841 – 2865.

[11] J.-Y. An, S. Kim, H.-J. Kim, J. Seo, *Building and Environment* **45** (2010) 1826 – 1833.

[12] B.F. Yu, Z.B. Hu, M. Liu, H.L. Yang, Q.X. Kong, Y.H. Liu, *Int. J. Refrig.* **32** (2009) 3 – 20.

[13] S. Wilburn, *Am. J. Nurs.* **99** (1999) 71.

[14] D. Grosjean, A.H. Miguel, T.M. Tavares, *Atmos. Environ. B* **24** (1990) 101 – 106.

[15] G. Leonardos, D. Kendall, N. Barnard, *J. Air Pollut. Control Assoc.* **19** (1969) 91 – 95.

[16] "Overall Evaluations of Carcinogenicity to Humans, Acetaldehyde [75-07-0] (Vol. 71, 1999), Formaldehyde [50-00-0] (Vol. 88, 2004).", International Agency for Research on Cancer (IARC). The IARC Monographs Series.

[17] "European Risk Observatory Report. Exploratory Survey of Occupational Exposure Limits for Carcinogens, Mutagens and Reprotoxic substances at EU Member States Level.", European Agency for Safety and Health at Work. (2009).

[18] "Permissible Exposure Limits. Occupational Safety and Health Administration.", Occupational Safety and Health Administration (OSHA) (Washington DC, 2005).

[19] M. Dunky, *Int. J. Adhes. Adhes.* **18** (1998) 95 – 107.

[20] L. Sopyan, M. Watanabe, S. Murasawa, K. Hashimoto, A. Fujishima, *J. Photochem. Photobiol. A* **98** (1996) 79 – 86.

[21] D.A. McNaught, A. Wilkinson, "IUPAC. Compendium of Chemical Terminology, 2nd ed.", Blackwell Scientific Publications (Oxford, 1997).

[22] H. Xu, S. Ouyang, L. Liu, P. Reunchan, N. Umezawa, J. Ye, *J. Mater. Chem. A* **2** (2014) 12642 – 12661.
[23] A. Mills, S. Le Hunte, *J. Photochem. Photobiol. A* **108** (1997) 1 – 35.
[24] B. Ekstrand – Hammarström, C.M. Akfur, P.O. Andersson, C. Lejon, L. Österlund, A. Bucht, *Nanotoxicology* **6** (2012) 623 – 634.
[25] S. Lakshmi, R. Renganathan, S. Fujita, *J. Photochem. Photobiol. A* **88** (1995) 163 – 167.
[26] A. Fujishima, T.N. Rao, D.A. Tryk, *J. Photochem. Photobiol. C* **1** (2000) 1 – 21.
[27] US Geological Survey Minerals Yearbook (2011).
[28] O. Carp, C.L. Huisman, A. Reller, *Prog. Solid State Chem.* **32** (2004) 33 – 177.
[29] A. Mattson, L. Österlund, *J. Phys. Chem. C* **114** (2010) 14121 – 14132.
[30] L. Kavan, M. Grätzel, S.E. Gilberg, C. Klemenz, H.J. Scheel, *J. Am. Chem. Soc.* **118** (1996) 6716 – 6723.
[31] R.J. Tayade, P.K. Surolia, R.G. Kulkarni, R.V. Jasra, *Sci. Tech. Advanced Mater.* **8** (2007) 455 – 462.
[32] D.O. Scanlon, C.W. Dunnill, J. Buckeridge, S.A. Shevlin, A.J. Logsdail, S.M. Woodley, C.R.A. Catlow, J. Powell, R.G. Palgrave, I.P. Parkin, G.W. Watson, T.W. Keal, P. Sherwood, A. Walsh, A.A. Sokol, *Nature Materials* **12** (2013) 798 – 801.
[33] T. Kawahara, T. Ozawa, M. Iwasaki, H. Tada, S. Ito, *J. Coll. Interface Sci.* **267** (2003) 377 – 381.
[34] B. Ohtani, O.O. Prieto-Mahaney, D. Li, R. Abe, *J. Photochem. Photobiol. A* **216** (2010) 179 – 182.
[35] Q. Xu, Y. Ma, J. Zhang, X. Wang, Z. Feng, C. Li, *J. Catal.* **278** (2011) 329 – 335.
[36] Y. Paz, *Appl. Catal. B* **99** (2010) 448 – 460.
[37] B. Shelimov, N. Tolkachev, G. Baeva, A. Stakheev, V. Kazansky, *Catal. Today* **176** (2011) 3 – 6.
[38] P. Pichat, J. Disdier, C. Hoang-Van, D. Mas, G. Goutailler, C. Gaysse, *Catal. Today* **63** (2000) 363 – 369.
[39] W.-K. Jo, K.-H. Park, *Chemosphere* **57** (2004) 555 – 565.
[40] S. Pigeot-Remy, J.C. Lazzaroni, F. Simonet, P. Petinga, C. Vallet, P. Petit, P.J. Vialle, C. Guillard, *Appl. Catal. B* **144** (2014) 654 – 664.
[41] L. Yang, A. Cai, C. Luo, Z. Liu, W. Shangguan, T. Xi, *Sep. Purif. Technol.* **68** (2009) 232 – 237.
[42] Y. Kikuchi, K. Sunada, T. Iyoda, K. Hashimoto, A. Fujishima, *J. Photochem. Photobiol. A* **106** (1997) 51 – 56.
[43] M. Houmard, D. Riassetto, F. Roussel, A. Bourgeois, G. Berthomé, J.C. Joud, M. Langlet, *Surf. Sci.* **602** (2008) 3364 – 3374.
[44] K. Midtdal, B.P. Jelle, *Sol. Energy Mater. Sol. Cells* **109** (2013) 126 – 141.
[45] I.P. Parkin, R.G. Palgrave, "CVD of Functional Coatings in Glass", editors Anthony C. Jones and Michael L. Hitchman in "Chemical Vapour Deposition: Precursors, Processes and Applications", (RSC, 2008), 451 – 476.
[46] D. Mills, T. Kreouzis, A. Sapelkin, B. Unal, N. Zyuzikov, K.W. Kolasinski, *Appl. Surf. Sci.* **253** (2007) 6575 – 6579.
[47] M. Kamei, T. Mitsuhashi, *Surf. Sci.* **463** (2000) 609 – 612.
[48] H.P. Boehm, *Discuss. Faraday Soc.* **52** (1971) 264 – 275.
[49] Y. Nosaka, M.A. Fox, *J. Phys. Chem.* **92** (1988) 1893 – 1897.
[50] W.A. Pryor, *Ann. Rev. Physiol.* **48** (1986) 657 – 667.
[51] P. Vassiliev, M.J. Louwerse, E.J. Baerends, *Chem. Phys. Lett.* **398** (2004) 212 – 216.

[52] S. Du, J.S. Francisco, G.K. Schenter, T.D. Iordanov, B.C. Garrett, M. Dupuis, J. Li., *J. Chem. Phys.* **124** (2006) 224318.1 – 224318.15.

[53] M.L. Sauer, D.F. Ollis, *J. Catal.* **149** (1994) 81 – 91.

[54] L. Zhang, W.A. Anderson, S. Sawell, C. Moralejo, *Chemosphere* **68** (2007) 546 – 553.

[55] B. Ou, D. Li, Q. Liu, Z. Zhou, B. Liao, *Mater. Chem. Phys.* **135** (2012) 1104 – 1107.

[56] Y. Zhao, X. Du, X. Wang, J. He, Y. Yu, H. He, *Sens. Actuators B* **151** (2010) 205 – 211.

[57] Y. Jiang, R. Amal, *Appl. Catal. B* **138-139** (2013) 260 – 267.

[58] P. Huo, Y. Yan, S. Li, H. Li, W. Huang, S. Chen, X. Zhang, *Desalination* **263** (2010) 258 – 263.

[59] K. Arata, *Appl. Catal. A* **146** (1996) 3 – 32.

[60] Z. Topalian, G.A. Niklasson, C.G. Granqvist, L. Österlund, *Thin Solid Films* **518** (2009) 1341 – 1344.

[61] T. López, P. Bosch, F. Tzompantzi, R. Gómez, J. Navarrete, E. López-Salinas, M.E. Llanos, *Appl. Catal. A* **197** (2000) 107 – 117.

[62] A. Corma, A. Martínez, C. Martínez, *Appl. Catal. A* **144** (1996) 249 – 268.

[63] G. Cólon, M.C. Hidalgo, J.A. Navío, *Appl. Catal. B* **45** (2003) 39 – 50.

[64] D.S. Muggli, L. Ding, *Appl. Catal. B* **32** (2001) 181 – 194.

[65] Y. Niu, M. Xing, B. Tian, J. Zhang, *Appl. Catal. B* **115-116** (2012) 253 – 260.

[66] C. O'Keeffe, P. Gannon, P. Gilson, A. Kafizas, I.P. Parkin, R. Binions, *Thin Solid Films* **537** (2013) 131 – 136.

[67] U. Diebold, N. Ruzycki, G.S. Herman, A. Selloni, *Catal. Today* **85** (2003) 93 – 100.

[68] M. Lazzeri, A. Vittadini, A. Selloni, *Phys. Rev. B* **63** (2001) 155409.

[69] U. Diebold, *Surf. Sci. Rep.* **48** (2003) 53 – 229.

[70] M.V. Dozzi, E. Selli, *Catalysts* **3** (2013) 455 – 485.

[71] S. Liu, J. Yu, M. Jaroniec, *Chem. Mater.* **23** (2011) 4085 – 4093.

[72] A. Vittadini, A. Selloni, F.P. Rotzinger, M. Grätzel, *Phys. Rev. Lett.* **81** (1998) 2954.

[73] G.S. Herman, Z. Dohnálek, N. Ruzycki, U. Diebold, *J. Phys. Chem. B* **107** (2003) 2788 – 2795.

[74] X.-Q. Gong, A. Selloni, *J. Phys. Chem. B* **109** (2005) 19560 – 19562.

[75] H.G. Yang, C.H. Sun, S.Z. Qiao, J. Zou, G. Liu, S.C. Smith, H.M. Cheng, G.Q. Lu, *Nature* **453** (2008) 638 – 641.

[76] J.S. Chen, Y.L. Tan, C.M. Li, Y.L. Cheah, D. Luan, S. Madhavi, F.Y.C. Boey, L.A. Archer, X.W. Lou, *J. Am. Chem. Soc.* **132** (2010) 6124 – 6130.

[77] M. Liu, L. Piao, W. Lu, S. Ju, L. Zhao, C. Zhou, H. Li, W. Wang, *Nanoscale* **2** (2010) 1115 – 1117.

[78] W.J. Ong, L.L. Tan, S.P. Chai, S.T. Yong, A.R. Mohamed, *Nanoscale* **6** (2014) 1946 – 2008.

[79] F. Pan, K. Wu, H. Li, G. Xu, W. Chen, *Chem. Eur. J.* **20** (2014) 15059 – 15101.

[80] X. Han, B. Zheng, J. Ouyang, X. Wang, Q. Kuang, Y. Jiang, Z. Xie, L. Zheng, *Chem. Asian J.* **7** (2012) 2538 – 2542.

[81] J. Pan, G. Liu, G.Q. Lu, H.-M. Cheng, *Ange. Chem., Int. Ed.* **50** (2011) 2133 – 2137.

[82] R. Li, F. Zhang, D. Wang, J. Yang, M. Li, J. Zhu, X. Zhou, H. Han, C. Li, *Nature Communications* 4 (2013) 1432.

[83] T. Ohno, K. Sarukawa, M. Matsumura, *New J. Chem.* **26** (2002) 1167 – 1170.

[84] T. Tachikawa, S. Yamashita, T. Majima, *J. Am. Chem. Soc.* 133 (2011) 7197 – 7204.

[85] S.K. Wallace, K.P. Mckenna, *J. Phys. Chem. C* **119** (2015) 1913 – 1920.
[86] W. Wang, Y. Zhou, Y. Ni, C. Lu, Z. Xu, *Mater. Lett.* **145** (2015) 180 – 183.
[87] D.G. Howitt, A.B. Harker, *J. Mater. Res.* **2** (1987) 201 – 210.
[88] P. Singh, D. Kaur, *Physica B* **405** (2010) 1258 – 1266.
[89] K. Eufinger, D. Poelman, H. Poelman, R. De Gryse, G.B. Marin, *J. Phys. D* **40** (2007) 5232.
[90] S. Sério, M.E. Melo Jorge, M.J.P. Maneira, Y. Nunes, *Mater. Chem. Phys.* **126** (2011) 73 – 81.
[91] D. Le Bellac, G. Niklasson, C.G. Granqvist, *J. Appl. Phys.* **77** (1995) 6145 – 6151.
[92] J. Nisar, Z. Topalian, A. De Sarkar, L. Österlund, R. Ahuja, *Appl. Mater. Interfaces* **5** (2013) 8516 – 8522.
[93] H.M. Rietveld, *J. Appl. Crystalograph.* **2** (1969) 65 – 71.
[94] W. Kraus, G. Nolze, *J. Appl. Crystalograph.* **29** (1996) 301 – 303.
[95] M. Horn, C.F. Schwerdtfeger, E.P. Meagher, *Zeitschrift für Kristallographie* **136** (1972) 273 – 281.
[96] W.A. Dollase, *J. Appl. Crystalograph.* **19** (1986) 267 – 272.
[97] E. Zolotoyabko, *J. Appl. Crystalograph.* **42** (2009) 513 – 518.
[98] D. Depla, M. Mahieu, “Reactive Sputter Deposition” (Springer, 2008).
[99] R.L. Penn, J.F. Banfield, *Am. Mineralogist* **83** (1998) 1077 – 1082.
[100] R.L. Penn, J.F. Banfield, *Am. Mineralogist* **84** (1999) 871 – 876.
[101] N.A. Deskins, S. Kerisit, K.M. Rosso, M. Dupuis, *J. Phys. Chem. C* **111** (2007) 9290 – 9298.
[102] X.-Q. Gong, A. Selloni, *Phys. Rev. B* **76** (2007) 235307-1.
[103] H. Zhao, L. Liu, J.M. Andino, Y. Li, *J. Mater. Chem. A* **1** (2013) 8209 – 8216.
[104] J.A. Thornton, *Ann. Rev. Mater. Sci.* **7** (1977) 236 – 260.
[105] R. Swanepoel, *J. Phys. E Sci. Instrum.* **16** (1983) 1214 – 1222.
[106] H.K. Pulker, *Appl. Optics* **18** (1979) 1969 – 1977.
[107] W.J. Anthony, et al. *Handbook of Mineralogy*. http://www.handbookofmineralogy.org/, Mineralogical Society of America
[108] S. Hong, E. Kim, D.-W. Kim, T.-H. Sung, K. No, *J. Non-Cryst. Solids* **221** (1997) 245 – 254.
[109] N. Serpone, A.V. Emeline, *Int. J. Photoenerg.* **4** (2002) 91 – 131.
[110] B.I. Stefanov, N.V. Kaneva, G. Li Puma, C.D. Dushkin, *Coll. Surf. A* **382** (2011) 219 – 225.
[111] S.R. Morrison, *Sens. Actuators* **2** (1982) 329 – 341.
[112] G. Heiland, *Sens. Actuators* **2** (1982) 343 – 361.
[113] I. Salvado-Estivill, A. Brucato, G. Li Puma, *Ind. Eng. Chem. Res.* **46** (2007) 7489 – 7496.
[114] I. Salvado-Estivill, D.M. Hargreaves, G. Li Puma, *Environ. Sci. Technol.* **41** (2007) 2028 – 2035.
[115] I. Moreno, C.-C. Sun, *Optics Express* **16** (2008) 1808 – 1819.
[116] S. Huzinaga, “Gaussian Basis Sets for Molecular Calculations” in “Physical Sciences Data, Volume 16”, Elsevier (Amsterdam, 1984).
[117] P.J. Hay, W.R. Wadt, *J. Chem. Phys.* **82** (1985) 299.
[118] K.L. Schuchardt, B.T. Didier, T. Elsathagen, L. Sun, V. Gurumoorthi, J. Chase, J. Li, T.L. Windus, *J. Chem. Inf. Model.* **47** (2007) 1045 – 1052.
[119] R. Ditchfield, W.J. Hehre, J.A. Pople, *J. Chem. Phys.* **54** (1971) 724.
[120] W.J. Hehre, R. Ditchfield, J.A. Pople, *J. Chem. Phys.* **56** (1972) 2257.
[121] V.A. Rassolov, J.A. Pople, M.A. Ratner, T.L. Windus, *J. Chem. Phys.* **109** (1998) 1223.
[122] S.F. Boys, F. Bernardi, *Mol. Phys.* **19** (1970) 553 – 566.

[123] National Institute of Standards and Technology, “Precomputed Vibrational Scaling Factors”, http://cccbdb.nist.gov/vibscalejust.asp.
[124] J.E. Rekoske, M.A. Barteau, *Langmuir* **15** (1999) 2061 – 2070.
[125] H. Idriss, M.A. Barteau, *Catal. Lett.* **40** (1996) 147 – 153.
[126] H. Idriss, C. Diagne, J.P. Hindermann, A. Kiennemann, M.A. Barteau, *J. Cat.* **155** (1995) 219 – 237.
[127] V.V. Ordomsky, V.L. Sushkevich, I.I. Ivanova, *J. Mol. Catal. A* **333** (2010) 85 – 93.
[128] A.C. Vawdrey, J.L. Oscarson, R.L. Rowley, W.V. Wilding, *Fluid Phase Equilibria* **222-223** (2004) 239 – 245.
[129] S.W. Milverton, *Proc. R. Soc. London* **150** (1935) 287 – 308.
[130] J.M. Hermida-Ramón, M.A. Ríos, *Chem. Phys. Lett.* **290** (1998) 431 – 436.
[131] L.A. Curtiss, M. Blander, *Chem. Rev.* **88** (1988) 827 – 841.
[132] T. Yamaguchi, *Appl. Catal.* **61** (1990) 1 – 25.
[133] Z. Topalian, G.A. Niklasson, C.G. Granqvist, L. Österlund, *Appl. Mater. Interfaces* **4** (2012) 672 – 679.
[134] R.T. Zehr, M.A. Henderson, *Surf. Sci.* **602** (2008) 2238 – 2249.
[135] R. Méndez-Román, N. Cardona-Martínez, *Catal. Today* **40** (1998) 353 – 365.
[136] M. Lewandowski, D.F. Ollis, *Appl. Catal. B* **43** (2003) 309 – 327.
[137] L. Österlund, *Trends Photochem. Photobiol.* **12** (2010) 53 – 64.
[138] L. Österlund, "Vibrational spectroscopy of pure and doped TiO_2 photocatalysts" in the book "On Solar Hydrogen and Nanotechnology" L Vayssieres,Wiley & Sons (Singapore, 2009).
[139] D.V. Kozlov, A.V. Vorontsov, P.G. Smirniotis, E.N. Savinov, *Appl. Catal. B* **42** (2003) 77 – 87.
[140] A. Mills, J. Wang, D.F. Ollis, *J. Phys. Chem. B* **110** (2006) 14386 – 14390.
[141] M.W. Pitcher, S.M. Emin, M. Valant, *J. Chem. Educ.* **89** (2012) 1439 – 1441.
[142] M. Tatarko, J. Tricker, K. Andrzejewski, J.A. Bumpus, H. Rhoads, *J. Chem. Educ.* **76** (1999) 1680 – 1683.
[143] X. Chen, S.M. Halasz, E.C. Giles, J.V. Mankus, J.C. Johnson, C. Burda, *J. Chem. Educ.* **83** (2006) 265 – 267.
[144] S. Gravelle, B. Langham, B.V. Geisbrecht, *J. Chem. Educ.* **80** (2003) 911 – 913.

Acta Universitatis Upsaliensis

Digital Comprehensive Summaries of Uppsala Dissertations from the Faculty of Science and Technology 1307

Editor: The Dean of the Faculty of Science and Technology

Distribution: publications.uu.se
urn:nbn:se:uu:diva-265056

ACTA
UNIVERSITATIS
UPSALIENSIS
UPPSALA
2015